PROTEIN IMPREGNATED POLYMER (PIP) FILM INFRARED SENSOR USING SUSPENDED MICROELECTROMECHANICAL SYSTEMS (MEMS) PIXELS

THESIS

Tetsuo Kaieda, Captain, USAF

AFIT/GE/ENG/05-10

DEPARTMENT OF THE AIR FORCE
AIR UNIVERSITY

AIR FORCE INSTITUTE OF TECHNOLOGY

Wright-Patterson Air Force Base, Ohio

The views expressed in this thesis are those of the author and do not reflect the official policy or position of the United States Air Force, Department of Defense, or the U.S. Government.

AFIT/GE/ENG/05-10

PROTEIN IMPREGNATED POLYMER (PIP) FILM INFRARED SENSOR USING SUSPENDED MICROELECTROMECHANICAL SYSTEMS (MEMS) PIXELS

THESIS

Presented to the Faculty

Department of Electrical and Computer Engineering

Graduate School of Engineering and Management

Air Force Institute of Technology

Air University

Air Education and Training Command

In Partial Fulfillment of the Requirements for the

Degree of Master of Science in Electrical Engineering

Tetsuo Kaieda, BS

Captain, USAF

September 2005

PROTEIN IMPREGNATED POLYMER (PIP) FILM INFRARED SENSOR USING SUSPENDED MICROELECTROMECHANICAL SYSTEMS (MEMS) PIXELS

Tetsuo Kaieda, BS
Captain, USAF

Approved:

_____/signed/_____   _____
Paul E. Kladitis, Capt, USAF (Chairman)   Date

_____/signed/_____   _____
James A. Fellows, Lt Col, USAF (Member)   Date

_____/signed/_____   _____
Guna S. Seetharaman (Member)   Date

_____/signed/_____   _____
Yong C. Kim (Member)   Date

_____/signed/_____   _____
Michael A. Marciniak (Member)   Date

AFIT/GE/ENG/05-10

Abstract

The Air Force Research Laboratory Materials and Manufacturing Directorate have developed a novel protein impregnated polymer (PIP) suspension that changes resistivity as a function of absorbed infrared radiation. Due to this property, the PIP is a potential material for use as an uncooled bolometer, or thermal sensor. In this research, a thermally-isolated pixel design, sensor characterization methods, and sensor fabrication and processing steps were developed. To create a microbolometer, the PIP was applied to two prototype micro-electro-mechanical systems (MEMS) surface micro-machined structures. The first is a raised cantilever pixel array that uses residual stress polysilicon and metal film arms to bend the pixels away from their substrate. The second is a suspended membrane pixel array in which the backside silicon wafer substrate is removed. The thermal sensor's figures of merit responsivity, detectivity, noise equivalent power, noise equivalent temperature difference, and thermal time constant, were modeled. An attempt was made to evaluate the performance of the fabricated microbolometer pixels by comparing measured data to model predictions. This research shows the PIP material can be used to make a practical thermal sensor.

iv

To my Mother and Father.

To All who have taught me valuable lessons in life.

To the Future.

Acknowledgments

Table of Contents

List of Figures

List of Tables

List of Acronyms

Acronym	*Definition*
AFRL	Air Force Research Laboratory
$Ge_xSi_{1-x}O_y$	amorphous germanium silicon oxygen
CMOS	complementary metal-oxide semiconductor
CAD	computer aided drawing
DIW	de-ionized water
DARPA	Defense Advanced Research Project Agency
DIP	dual inline package
EM	electromagnetic
FPA	focal plane array
GPIB	General Purpose Interface Bus
IR	infrared
PCT	lead-calcium titanate
LPCVD	low-pressure chemical vapor deposition
MCT	mercury-cadmium-telluride
MEMS	micro-electro-mechanical systems
MLPC	Mound Laser and Photonics Center, Inc.
NAWC	Naval Air Warfare Center
NVESD	Night Vision and Electronic Sensors Directorate
NEP	noise equivalent power
NETD	noise equivalent temperature difference

PSG	phosphosilicate glass
PolyMUMPs	Polysilicon Multi-User MEMS Processes
KOH	potassium hydroxide
PIP	protein impregnated polymer
QWIP	quantum well infrared photodetector
RIE	reactive ion etch
ROIC	readout integrated circuit
SEM	scanning electron microscope
SNR	signal-to-noise ratio
Ag-O-Cs	silver-oxygen-cesium
TCR	temperature coefficient of resistance
UV	ultraviolet
UAV	unmanned aerial vehicle
W/V	weight by volume
YBaCuO	yttrium-barium-copper-oxide

PROTEIN IMPREGNATED POLYMER (PIP) FILM INFRARED SENSOR USING SUSPENDED MICROELECTROMECHANICAL SYSTEMS (MEMS) PIXELS

I. Introduction

1.1 Motivation

In the efforts to develop methods of seeing in darkness and obscured visibility, three approaches have been tried. First is to provide an artificial source of illumination, second is to amplify the small amounts of ambient illumination present, and third is to detect and image electromagnetic (EM) radiation emitted by an object. Figure 1 shows black and white imagery taken using a modern thermal imaging camera. The image was taken during night time hours with white showing lowest temperature and black showing highest temperature. Developments and field applications in all three approaches have been tried by the US military since World War I [1].

Figure 1. Infrared image of cityscape taken with modern thermal imaging camera during night time hours [2].

1

1.2 Statement of Problem

The Air Force Research Laboratory (AFRL) Materials and Manufacturing Directorate have developed a novel material that responds to infrared (IR) energy. This material is a protein impregnated polymer (PIP) suspension that changes resistivity when it absorbs IR radiation. Due to this material property, the PIP material is a viable sensing material for use in a specific type of IR sensor called a bolometer [3]. A bolometer is a thermal sensor that detects IR radiation by changing electrical resistivity as a function of absorbed thermal energy.

The bolometer pixel designs implemented by the AFRL are relatively large and have low sensitivity. The sensor arrays created by the AFRL have low resolution due to the large pixel size and low density of pixels. Modern bolometric IR sensors have pixel arrays on the order of 640 x 480 and sensitivities able to distinguish target temperature differences on the order of 10 mK. The problems this thesis will address are: large pixel size, low pixel sensitivity, and low density of pixels in an array.

1.3 Proposed Solution

I propose to build a functioning micro-sized bolometer (microbolometer) prototype by applying the PIP material on top of polysilicon micro-electro-mechanical systems (MEMS) surface micro-machined structures. The goal is to solve the problems using raised pixel and suspended membrane designs to thermally isolate the pixels to improve sensitivity, and MEMS structures to decrease pixel and array size, while increasing array pixel density.

1.4 Approach

To create a functioning microbolometer using the PIP material will require the development of a thermally isolated pixel design, sensor characterization methods, and material fabrication and processing steps. The PIP material has not yet been fully characterized to determine many of its electrical and mechanical properties that would be required for a thorough understanding of its theoretical behavior.

The proposed microbolometer will begin with two designs. The first design is a raised cantilever pixel array that will thermally isolate each pixel by using residual stress polysilicon arms to bend the pixel away from the substrate. An example of a bolometer pixel using amorphous silicon as the temperature sensing material is shown in Figure 2. The individual pixels are fabricated and suspended above the integrated circuitry in monolithic system architecture. Figure 3 shows a close-up of a pixel post from Figure 2, used to provide thermal isolation of the pixel from the bulk substrate. The material is etched away to form a gap, leaving an arm as the primary path of thermal energy flow. The second design is a suspended membrane pixel array that thermally isolates the array by removing the bulk crystalline silicon wafer substrate beneath the pixel. Both pixel arrays have multiple design variables that affect the figures of merit of the microbolometer. The figures of merit can be derived from experimental measurements and through analytical modeling of each design.

The figures of merit of each microbolometer are responsivity ($\Re$), detectivity (D*), noise equivalent power (NEP), noise equivalent temperature difference (NETD), and time constant (τ). The responsivity and detectivity of a microbolometer array are

3
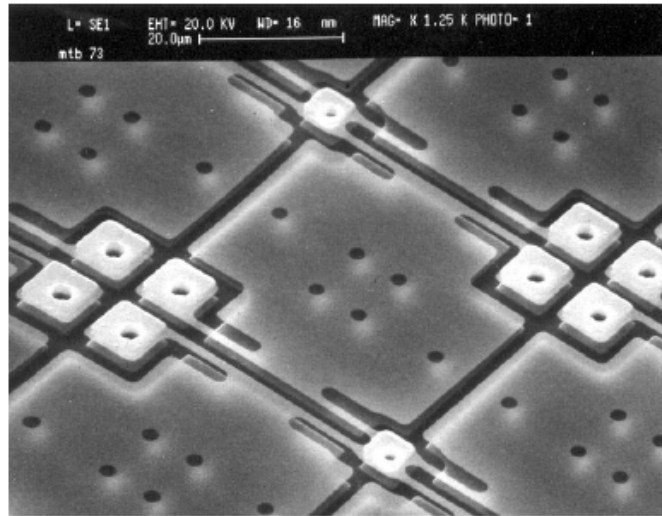
Figure 2. Scanning Electron Microscope (SEM) image of bolometer pixels using amorphous silicon for temperature sensing [4].

measures of sensitivity of the electrical output signal to the incident irradiant power. The

detectivity is a normalized responsivity for pixel area and system frequency response.

The NEP and NETD are measures of sensitivity of the power absorbed and target
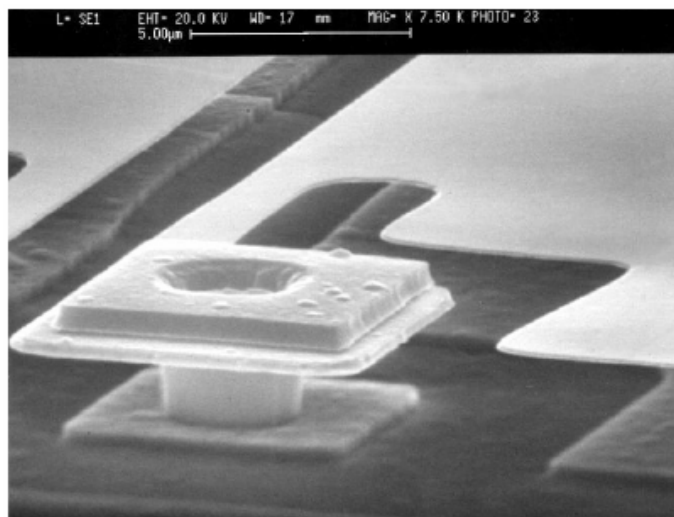
Figure 3. SEM image of microbolometer interconnect post and pixel support arm [4].

4

temperature change that produce a unit change in the electrical signal to total rms noise ratio [5]. These qualitative measures will be used to judge the performance capabilities of the fabricated microbolometer array and will be compared to the analytical model predictions to verify model accuracy.

A commonly used technique for fabricating MEMS is poly-crystalline silicon surface micro-machining. For the case of a microbolometer sensor, the MEMS platforms will act as a thermal isolator for the PIP material, as well as the electrical connections to the sensor processing circuitry. A commercial MEMS fabrication process called Polysilicon Multi-User MEMS Processes (PolyMUMPs) [6] is available through the company, MEMSCAP. The PolyMUMPs fabrication process design rules will be described in detail in Chapter 3: Design and Fabrication.

1.5 Scope

Since the goal of this thesis is to demonstrate that the PIP material can be used to make a practical thermal sensor, this research will only concentrate on the following topics: building pixels using a commercial surface micromachining process, using PIP material supplied by AFRL, deriving figures of merit from experimental measurements on pixels, and comparing experimental results to modeled predictions of the figures of merit.

1.6 Contributions

The research performed in this thesis established fabrication techniques for incorporating a novel IR sensitive material into a surface micro-machined structure to

5

create a microbolometer. The first MEMS-based IR imaging bio-sensor was created using PIP material applied on top of a polysilicon micro-machined structure with a back cavity etched by laser-machining.

1.7 Chapter Outline

The following chapters will include the background and brief history of IR sensors and a current literature review in Chapter 2, a fabrication process for each pixel sensor in Chapter 3, theory of heat transfer, equations of the figures of merit, and mechanical residual stress in Chapter 4, the models derived from theory and calculated figures of merit for each pixel sensor in Chapter 5, experimental procedures for testing each pixel sensor for figures of merit and the results of testing in Chapter 6, and the findings and conclusions derived from the experiments in Chapter 7. Appendix A describes the circuit analysis and equation derivation for the readout integrated circuit (ROIC) used in the initial test setup. Appendix B describes the Agilent VEE program used for recording data and controlling the ammeter, signal generator, and voltmeter in the initial test setup. Appendix C describes the analysis of the ROIC signal bandwidth.

II. Background

2.1 Chapter Overview

The purpose of this chapter is to provide a short history of IR sensing and imaging technology and its uses, an overview of the military applications, a description of transduction and IR detection methods, and an explanation of the specific PIP material detection methodology and application.

2.2 History

In the development stages of IR detection technologies, several avenues and approaches to imaging with IR radiation were considered by scientists working for the US military. Over the course of several decades, the physics inherent in detecting IR radiation have begun to narrow the possibilities to a handful of practical devices. Research that initially investigated passive image intensifiers that use ambient or reflected light and cryogenically-cooled camera tubes has begun exploring uncooled staring (non-mechanically or optically-scanned) focal plane arrays (FPA), quantum-well IR photodetectors (QWIP), and mechanically-scanned cooled sensors [1]. Figure 4 shows a complete thermal sensing system on chip built using complementary metal-oxide semiconductor (CMOS) foundry processes.

2.2.1 EM Radiation Detection in the Military. One method of seeing in darkness or under obscured visibility is by generating a source of artificial illumination, ranging from radio waves, IR spotlight or visible light, to laser emissions. One drawback to using artificial illumination is that the source of illumination is then detectable to both the
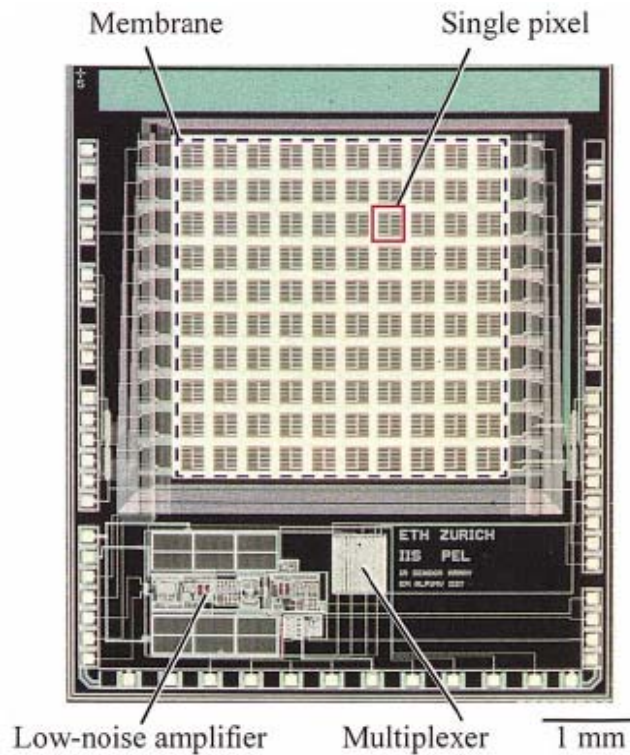
Figure 4. 100 pixel staring FPA thermocouple detector with on chip controls made using standard CMOS processes [7].

target and the sensor. This is a key vulnerability that alerts enemy targets to the presence of searching radar or spotlight systems [1].

Another method of seeing in darkness and obscured conditions is by amplifying ambient light, which does not actively emit any radiation and thus cannot be detected by an enemy target. Passive light enhancers amplify existing ambient near-IR light to render an image or scene. For passive light enhancers to function properly, a minimum level of ambient light must be present. Typically, the light level present must be approximately the same conditions that exist on a clear starry night or a moonlit night. This limitation

can severely hamper or exclude image intensifiers from use in many combat or security situations [1].

Passive IR imaging does not emit radiation nor does it rely on the presence of near-visible light. IR imaging does require the presence of EM energy, but Planck's radiation law states that energy is emitted by any object that is above absolute zero Kelvin, which is every object in the known universe. Wien's Displacement Law shows that a person at room temperature emits peak detectable IR radiation at a wavelength around 10 μm [8]. Thus, many military targets of interest are at temperatures that can be sensed by the two common methods of IR detection, thermal absorption and photon detection [1].

2.2.2 IR Sensing and Detecting. IR radiation sensors are used in many different industrial, military, scientific research, and civil applications as shown in Figure 5. Industrial uses include monitoring process temperatures, tracking heat flow within objects, detecting heat stress, and various other uses [13-15,27]. Scientific research has found use for IR sensors in satellites for tracking weather, monitoring deep space and star emissions, analyzing chemicals, and performing spectroscopy measurements [10,12-14,26,27]. In the civil sector, they are used for security monitoring, consumer electronics, and a variety of medical uses [14,15,23,25,27]. Military applications include night vision devices, target tracking sensors and devices, and fiber optic communications [11,14,15,17,19-23,25,27]. The applications and uses are widespread across many different fields, and interest in improving sensor quality, reducing weight, size and cost,
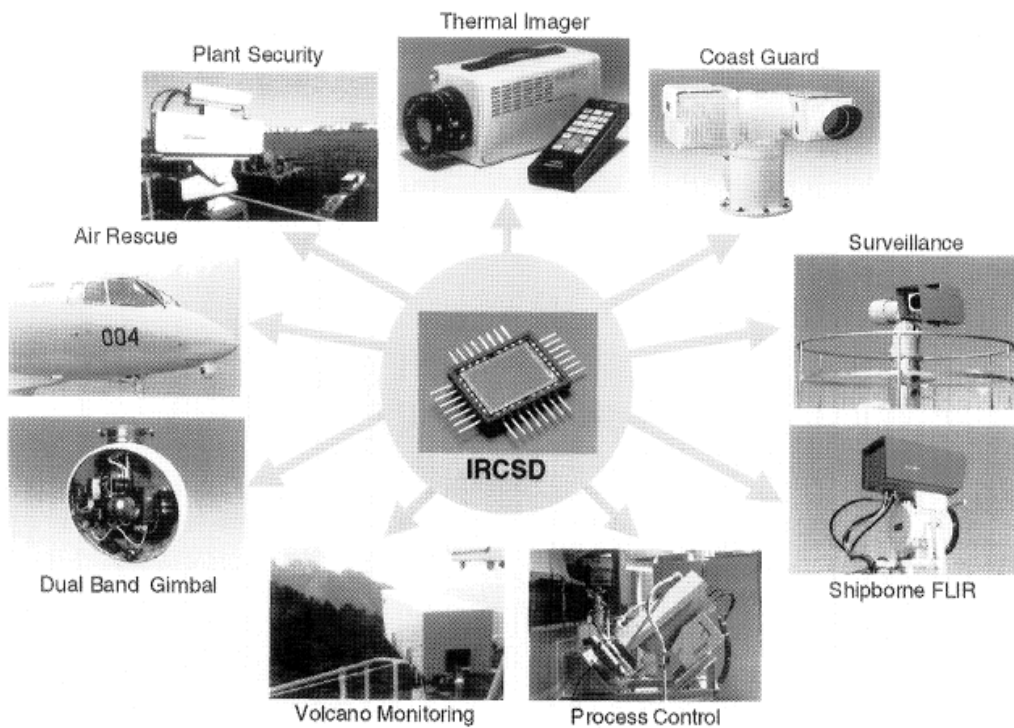
Figure 5. Infrared Charge Sweep Device technology and uses developed by Mitsubishi Electric Corporation [9].

and increasing the number of strategic and tactical field uses are driving further developments in the field of IR sensing [10,14-25,27,28].

Military interest in sensor information capabilities has been guided by the desire to conduct operations at night time and under harsh visibility conditions. By exploiting the omnipresence of non-visible EM energy emissions, a battlefield or tactical image can be created real-time under adverse conditions. A subset of non-visible EM energy, the IR spectrum, includes the blackbody spectral radiation emission curves for temperatures at or around 21 °C (293 Kelvin) which is commonly known as "room temperature." By Wien's Displacement Law, there are peak-energy-emission-spectra differences between

targets and backgrounds which allow objects at different temperatures near room temperature, such as people, vehicle engines, and buildings, to be imaged relative to their background temperature [29].

2.2.3 *IR Imaging in the Military.* The US Army began developing near-IR (0.7 – 2 µm) image intensifiers in the 1920s. The S-1 silver-oxygen-cesium (Ag-O-Cs) photocathode system was the first generation of IR imaging technology to be explored for military use. Its development eventually led to the S-25, which is the third generation of image intensifiers developed in the mid 1960s, and still in use by the military today. Early exploration of passive near-IR imaging led to thermal difference imaging using mid-IR (3 – 5 µm) and far-IR (8 – 14 µm) during the 1940s through the 1950s. In order to improve imaging techniques, opto-mechanically scanned single sensors and linear arrays were developed during the 1960s. Also during the 1960s, the next breakthrough of sensing materials using a cooled mercury-cadmium-telluride (MCT) compound, further improved the quality of sensors. The added weight and cost of actively cooling the sensors spurred exploration in alternative materials and sensing methods leading to ideas for uncooled arrays based on ferroelectric-pyroelectric, resistive (bolometric), Golay cells, quartz microresonators, and various other optical, mechanical, and electrical material properties. Most of the initial research in uncooled IR imaging, which began in the early 1980s, was done primarily by the US Army Night Vision and Electronic Sensors Directorate (NVESD), the Defense Advanced Research Project Agency (DARPA), and the Naval Air Warfare Center (NAWC) [1].

As the Air Force develops smaller Unmanned Aerial Vehicles (UAV), the requirements for maximum allowable size and weight of onboard sensors, demand smaller and lighter weight sensors. In order to use micro UAVs in zero visibility, obscured visibility, and night operations, they must be equipped with sensors capable of operating within these environments. Currently, cooled IR sensors are too large and heavy and require large amounts of energy to function. Similar light amplification and night vision sensors lack the capability and spectral range of IR sensors. Figure 6 shows the StarSAFIRE III, a currently employed IR sensing and optical viewing system produced by FLIR Systems, Inc. The system and turret mounting is 17.55" by 15.10" and weighs approximately 98 lbs.

Systems like the StarSAFIRE III are too large and bulky for use in small and micro sized UAV designs. In order to achieve a small, lightweight, and inexpensive IR sensor, there are several problems that will have to be overcome to which uncooled thermal sensors potentially offer the solution. The PIP material developed by

Figure 6. StarSAFIRE III IR detection system employing 640 x 480 indium antimonide mid-IR FPA made by FLIR Systems, Inc [30].

the AFRL has the potential to achieve a small, rugged, lightweight and cheaply fabricated IR sensor.

2.3 Literature Review

There are two principal methods of IR detection. Both methods transduce IR radiation energy into a useable electrical, optical, or mechanical signal. First, the direct method where semiconductor photon detectors absorb photons in the IR energy range directly and produce free electron-hole pairs. Second, the indirect method where thermal detectors absorb photons causing a temperature change, which must be inferred by measuring a corresponding change in the detector's temperature dependent property [31].

2.3.1 Temperature Effect Transducing. The effect of IR radiation on an object can cause a variety of useful effects for measuring changes in temperature. Since temperature cannot be measured directly, it must first be transduced, typically in three steps. First, a non-thermal signal is transduced into a heat flow. Second, the heat flow is converted into a temperature difference. Third, the temperature difference is transduced, typically into an electrical signal [32]. The two methods by which this is done for micro-sized structures are photon transduction and thermal transduction. Photon transduction is said to be a direct method because it is used to convert a non-thermal signal directly to an electrical signal. Thermal transduction is said to be an indirect method because it must follow all three steps [29].

2.3.2 Direct Detection Methods. Currently, photon transduction methods are applied by using photoconductive, photovoltaic, and photoemissive effects. An example

13

of an MCT IR detector is shown in Figure 7. The detector is a dual-band multilayer

photovoltaic detector. The methods for direct transducing involve producing an electrical

signal by increasing conductivity by generation of free carriers, generation of electrical

current by generating free carriers in a p-n junction, or by internal emission of electrons

by incident light. The generation of carriers with or without a p-n junction determines

whether the transducer is a photoconductor or photovoltaic sensor. For photoconductive

and photovoltaic detectors, the photon must have the same or more energy than the

energy bandgap of the semiconductor. For the photoconductor, where sensing is done

without a p-n junction, the sensor is depending on incident light to generate electron-hole

pairs to alter the number of free carriers in the material, changing its resistive properties.

The photoelectric effect is when a material absorbs high energy photons that generate

electrons in a material that overcome the work function of a barrier material or electric
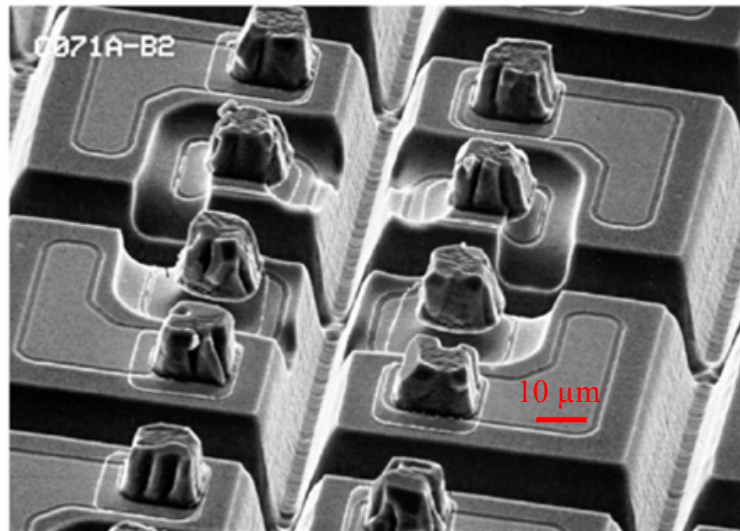
Figure 7. SEM image of a 75 µm x 75 µm dual-band wavelength MCT photovoltaic IR detector pixel [27].

field. A common photoemissive detector is a metal-semiconductor Schottky barrier. The photo-generation of electrons occurs in the metal and generated electrons with enough energy are detected as they are swept across the electric field of the Schottky diode. For the case of a photovoltaic detector, the generation of electron-hole pairs is done on or within one diffusion length of the depletion region, the carriers are swept across the depletion region causing current to flow. A photoconductive sensor requires the proper electrical bias and signal processing to detect a change in resistance which is used to detect incident IR radiation. All of these effects require that the incident light have sufficient energy in order to generate carriers or cause electrons to be released. The photon energy is directly related to its wavelength, which determines the IR band in which the detector is sensitive [32].

Some direct detection methods require electrical biasing in order to process the electrical signals generated by transducing. Also, devices that use quantum effects to sense IR radiation require that the sensor be cooled in order to achieve practical sensitivities and feasible sensors. Cooling the devices comes with a high cost, increased energy consumption, larger size and increased weight [33]. For this reason, most photon detection methods are not considered for use as ambient temperature IR sensors.

2.3.3 Indirect Detection Methods. The indirect thermal transduction methods typically implemented are pyroelectric/ferroelectric effects, thermoelectric effects, and resistive bolometers. Other novel attempts have been made using opto-mechanical devices [34] as shown in Figure 8, Golay cells [33], and quartz crystal resonators [35], but these devices fall outside of the common attempts to create practical uncooled IR

imaging systems. Figure 8 shows an SEM image of gold covered silicon nitride

diffraction grating pixels controlled by thermally generated stress in cantilever arms.

The most success in uncooled imaging has been met by using

pyroelectric/ferroelectric materials or resistive bolometers [29], as shown by images in

Figures 9 and 10. Figure 9 shows an IR image taken using a thin-film ferroelectric pixel

array camera with f/1 optics. Figure 10 shows an IR image taken using a monolithic

silicon 240 x 336 FPA at room temperature using f/1 optics and 30 Hz camera frame rate.

Recently implemented designs include devices and materials such as CMOS n-

wells, demonstrated in Figure 11, yttrium-barium-copper-oxide (YBaCuO) compound,

shown in Figure 12, and pyrolized parylene [40]. Figure 11 shows a CMOS n-well pixel

Figure 8. SEM of pixels using optical gratings controlled by thermally generating stress in SiN cantilever arms [34].

16

Figure 9. IR image taken with thin-film ferroelectric pixel array camera with f/1 optics [36].

suspended by two arms over an etched pit. Figure 12 shows an array of pixels using

semiconducting YBaCuO as a microbolometer.

Figure 10. IR image obtained using monolithic silicon 240 x 336 FPA operating at room temperature with camera f/1 optics and 30 Hz frame rate [37].

17
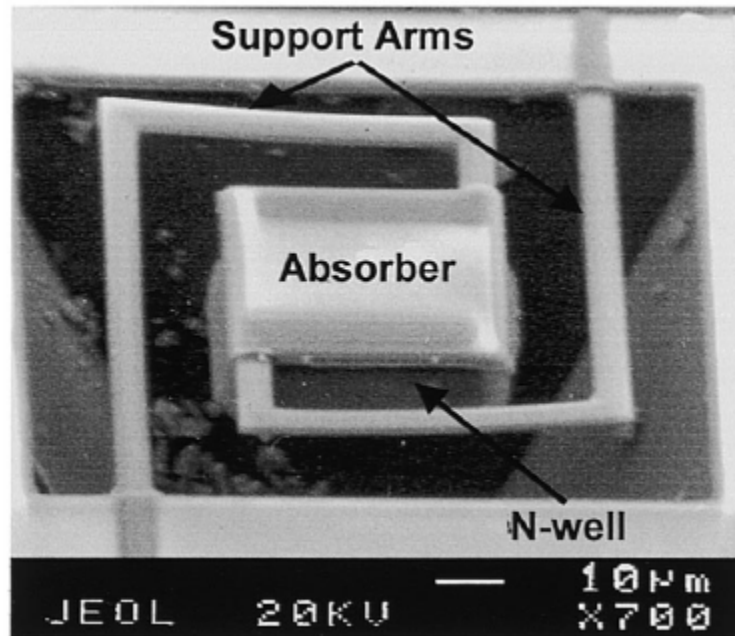
Figure 11. SEM image of single pixel CMOS n-well microbolometer with 100 μm x 100 μm pixel size [38].
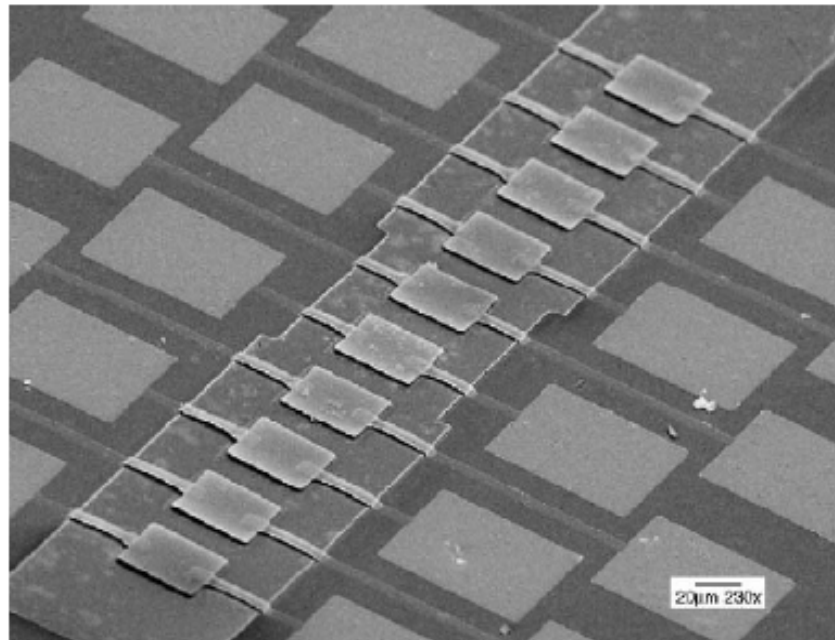
Figure 12. One by ten array of 60 μm x 60 μm YBaCuO bolometer pixels [39].

18

The pyroelectric/ferroelectric effect is the spontaneous electric or magnetic polarization of opposite crystal faces caused by a change in the temperature of the material. The charge from the polarization is neutralized by internal charge flow. If the crystal's temperature is changed rapidly in time, a pulsed electrical signal is generated. The nature of pyroelectric/ferroelectric detectors requires optical chopping of the incident IR energy to cause a rapid temperature change. The pyroelectric/ferroelectric properties of a crystal disappear above a certain temperature, called the Curie temperature, requiring the sensor to remain below the Curie temperature in order to function properly [29]. Figure 13 shows an image of a thin film lead-calcium titanate (PCT) ferroelectric array with pixel size of 50 μm x 50 μm.
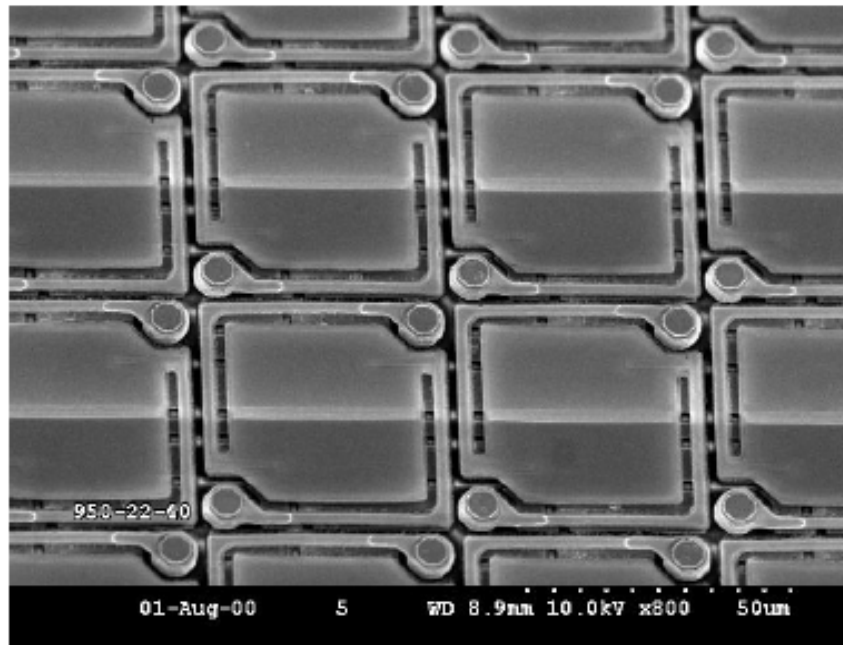
Figure 13. SEM of uncooled thin-film PCT ferroelectric infrared imaging array with pixel size of 50 μm x 50 μm [36].

A thermopile is a collection of thermocouples which are used to amplify absorbed IR radiation signals. Thermocouples are junctions of dissimilar conductors that, when heated on one end, generate a proportional voltage to the temperature difference of one junction to another. This property is known as the Seebeck effect, named after its discoverer [33]. Figure 14 shows an example of a 250 µm x 250 µm thermopile pixel using polysilicon and aluminum junctions in 12 thermocouples. Figure 14 shows the relative cold and hot contacts across which a voltage difference is generated, and gold lines that are used for heat sinks and to minimize electrical noise between pixels.
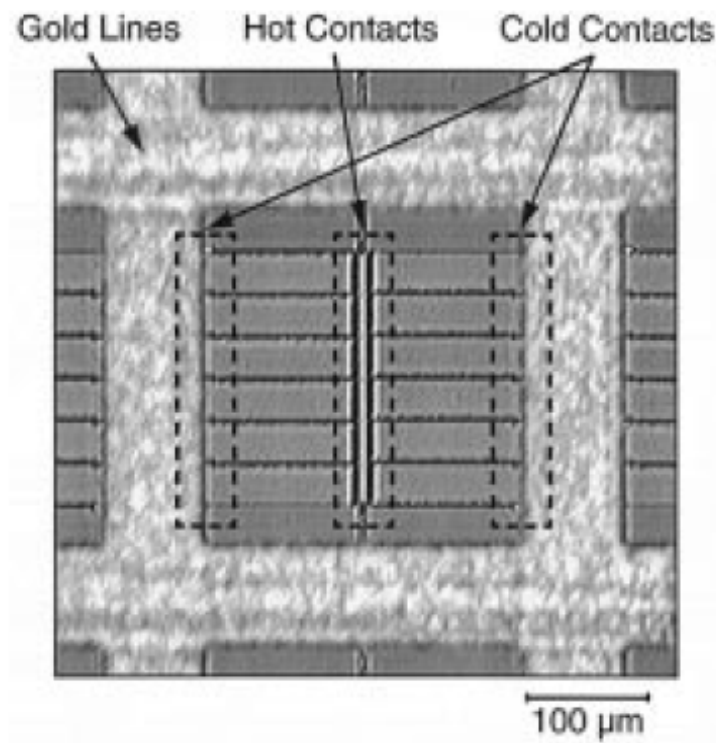
Figure 14. SEM image of uncooled 250 µm x 250 µm thermopile pixel using polysilicon and Al thermocouple junctions [41].

By absorbing thermal energy, a resistive bolometer changes temperature, causing the resistance of the material to change. This process is similar to photoconductive sensing, but the resistance can either increase or decrease as a function of increasing temperature. The property of the material, called temperature coefficient of resistance, will determine how its resistance changes with temperature and can change either positively or negatively [5]. Figure 15 shows an example of a 100 μm x 100 μm bolometer pixel using amorphous germanium silicon oxygen ($Ge_xSi_{1-x}O_y$) compound suspended over a bulk micromachined pit.

Indirect detecting methods are common methods used for uncooled detector arrays with a variety of exotic sensing materials. These methods make several qualitative trade-offs, such as requiring optical chopping systems, electrical biasing circuitry, or
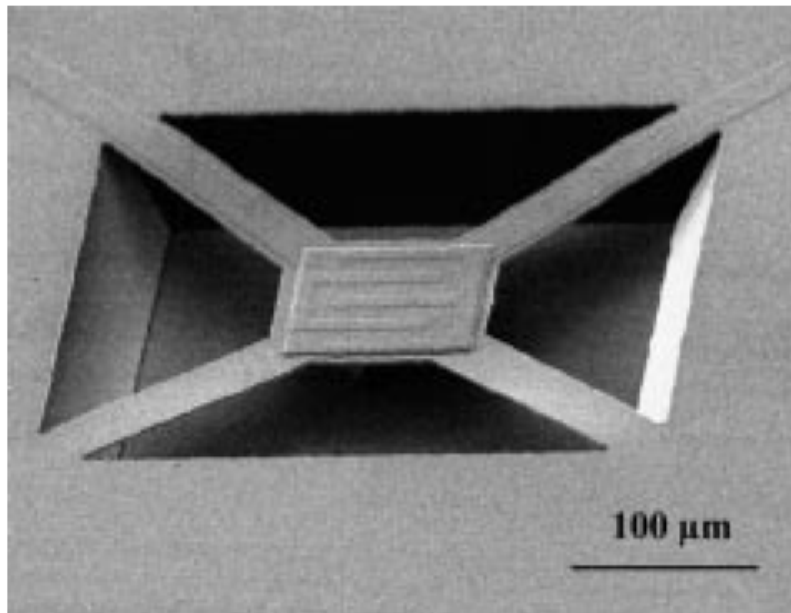
Figure 15. SEM image of uncooled 100 μm x 100 μm bolometer pixel based on amorphous $Ge_xSi_{1-x}O_y$ on bulk micromachined Si structures [42].

large pixel sizes, in order to save in cost, energy consumption, size, and weight. Depending on the application, these trade-offs may be necessary to make a suitable sensor [29].

2.4 PIP Material Sensing Properties

The PIP material incorporates a biological protein and powdered carbon black by suspending the protein and carbon within a polymer mixture of polyvinyl alcohol and polyethylene glycol to create a novel thermal sensitive material. The PIP material has demonstrated indirect thermal detecting properties similar to a bolometer. The AFRL scientists have shown the PIP material to have a negative temperature coefficient of resistance and resistive properties that can be quantified similarly to a semiconductor, poly-crystalline, or amorphous compound. The protein material is a helically coiled structure that uncoils and expands as a function of temperature. The expansion of the uncoiling protein re-agglomerates the carbon black, thereby changing the resistance of the PIP material. The carbon black powder is designed to act as an electrically conductive element and an IR absorbing element for the PIP material. The polymer suspension structure gives the PIP material a viscous liquid form that dries after 24 hours and forms a thin rubbery material [3,43]. To date, the PIP material is a unique IR sensing material that has not been used for detecting or imaging, beyond the exploratory research performed at the AFRL.

2.5 Summary

This chapter has covered a brief history of IR imaging and military uses. The primary direct and indirect methods for detecting and imaging IR radiation were discussed. The PIP material is unique among materials currently being used for thermal imaging sensors because the active IR sensing material is purely biological. Other research being done currently is exploring materials and compounds commonly used or derived from silicon micromachining and solid state physics technology, refining pixel size and fill factor, and optimizing figures of merit. The completed microbolometer sensors will be characterized according to the figures of merit, which will be explained in detail in Chapter 3, Theory, but because this research is exploratory, the figures of merit will not be compared to the state of the art.

III. Design and Fabrication

3.1 Chapter Overview

The purpose of this chapter is to explain the commercial MEMS foundry processes and secondary post-processing methods used to create a micro-sized pixel platform for the PIP material. The first section of the chapter will break down the MEMS foundry processes into individual steps that are used to create the Suspended Membrane Pixel and the Raised Cantilever Arm Pixel designs. Using the fabricated MEMS design, a series of post-processing steps are applied to individual die to create a pixel sensor. The post-processing steps for creating a Suspended Membrane Pixel Sensor are explained in the second section and the Raised Cantilever Arm Pixel Sensor steps are explained in the third section of the chapter. The last section of the chapter summarizes the types of pixels designed and fabricated and the processes used to create each pixel sensor.

3.2 Commercial MEMS Fabrication

This section describes the sequential steps and micromachined layers that compose the PolyMUMPs service offered by the company MEMSCAP as explained in the PolyMUMPs Design Handbook, Revision 10.0 [6]. The PolyMUMPs process is a three-layer polysilicon surface micromachining process that uses standard micro-electronics fabrication technology to create MEMS structures [6]. Figure 16 shows a cross-section of the primary structural and sacrificial layers and reactive ion etch (RIE) steps used to build and pattern the PolyMUMPs structures. Figure 16 shows the five structural layers, two sacrificial layers (silicon dioxide), and four RIE steps with their nominal thicknesses or etch depths [6]. The five structural layers are three polysilicon

layers (Poly) intended to be primary structural layers, one silicon nitride layer (Nitride) used for electrical isolation from the silicon wafer substrate, and one chromium/gold layer (Metal) used for electrical pathways, probing, bonding, and as a highly reflective mirror surface. The Metal layer is primarily gold, but uses a thin layer of chromium to help the gold adhere to the Poly 2 layer [6]. The two sacrificial layers are phosphorous-doped silicon dioxide (Oxide), called phosphosilicate glass (PSG). The four RIE steps create connections from polysilicon layers to the silicon nitride or other polysilicon layers and also pattern dimples in the Poly 1 layer [6]. The Anchor cuts are designed to etch through both Oxide layers to create openings for the Poly layers to attach to the Nitride or
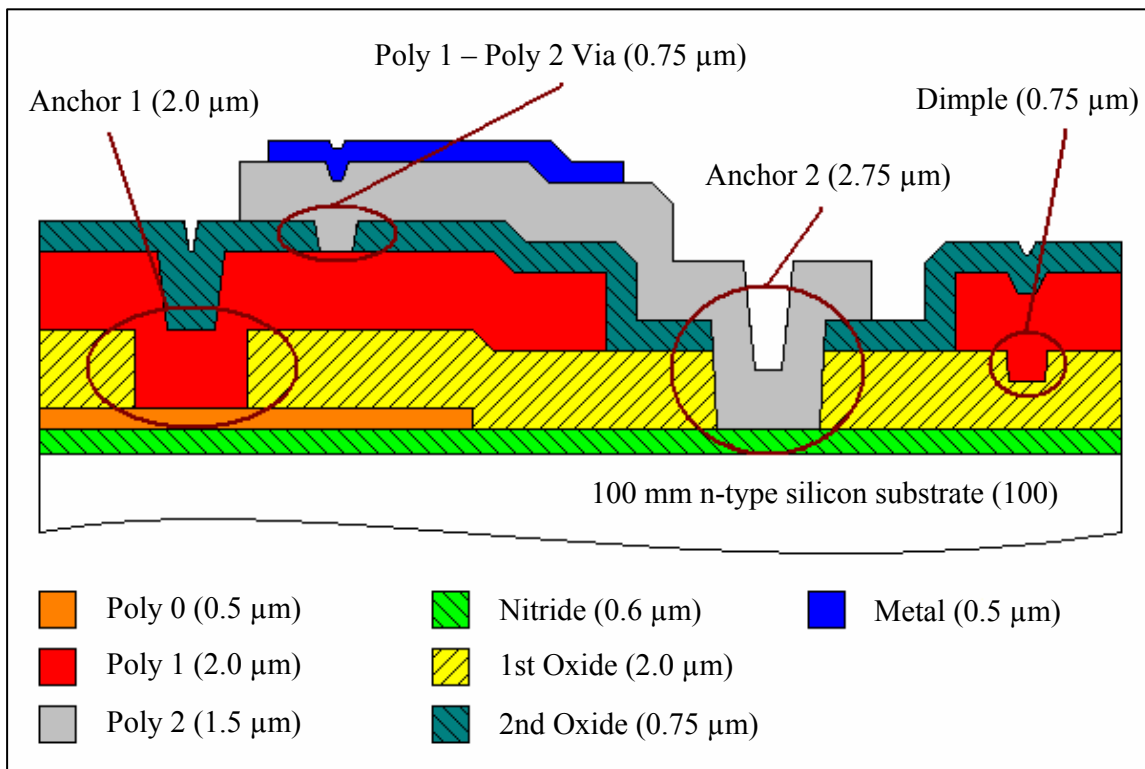
Figure 16. Cross-section of PolyMUMPs overview showing representative structural layers, sacrificial layers, and reactive ion etch steps.

Poly 0 layer. The Poly 1 – Poly 2 Via cut is designed to etch through the 2nd Oxide layer to create an opening for the Poly 2 layer to attach to the Poly 1 layer. The Dimple layer patterning under the Poly 1 layer is designed to add small area stand-offs to large structures to prevent them from adhering to the substrate permanently. Table 1 outlines the sequential steps performed by the PolyMUMPs service to create MEMS structures.

Table 1. Micromachining technique sequence performed by PolyMUMPs procedure.

Step #	Micromachining techniques performed
1	Deposit 0.6 μm of silicon nitride (Nitride layer) by LPCVD
2	Deposit 0.5 μm of polysilicon (Poly 0 layer) by LPCVD
3	Pattern and etch Poly 0 layer by photolithography using photoresist and RIE
4	Deposit 2.0 μm of PSG (1st Oxide layer) by LPCVD
5	Anneal wafer at 1050 °C in argon for 1 hour
6	Pattern and etch 0.75 μm Dimple cut in 1st Oxide layer by photolithography using photoresist and RIE
7	Pattern and etch 2.0 μm Anchor 1 cut in 1st Oxide layer by photolithography using photoresist and RIE
8	Deposit 2.0 μm of polysilicon (Poly 1 layer) by LPCVD
9	Deposit 0.2 μm of PSG by LPCVD
10	Anneal wafer at 1050°C in argon for 1 hour
11	Pattern and etch Poly 1 layer by photolithography using PSG and photoresist and RIE
12	Deposit 0.75 μm of PSG (2nd Oxide layer) by LPCVD
13	Anneal wafer at 1050 °C in argon for 1 hour
14	Pattern and etch 0.75 μm Poly 1 – Poly 2 Via cut in 2nd Oxide layer by photolithography using photoresist and RIE
15	Pattern and etch 2.75 μm Anchor 2 cut in 1st and 2nd Oxide layers by photolithography using photoresist and RIE
16	Deposit 1.5 μm of polysilicon (Poly 2 layer) by LPCVD
17	Deposit 0.2 μm of PSG by LPCVD
18	Anneal wafer at 1050 °C in argon for 1 hour
19	Pattern and etch Poly 2 layer by photolithography using PSG and photoresist and RIE
20	Pattern Metal layer by photolithography using photoresist
21	Deposit 200 Å/0.5 μm of chromium/gold by evaporation, excess removed by lift-off with photoresist chemical bath

The techniques used to deposit, pattern, and condition layers, and remove material are common microelectronics techniques. These techniques are low-pressure chemical vapor deposition (LPCVD), annealing, RIE, and photolithography. LPCVD builds material layers on a substrate by heating the substrate and passing a chemical vapor over the substrate. The vapor reacts and bonds to the heated substrate, causing a uniform thin film to grow on the exposed surface. Annealing places the substrate and thin films in a heated and pressurized inert gas environment close to the thin film melting temperatures to diffuse dopant materials and reduce residual stress within the thin films. RIE is a method of heating reactant gases and accelerating the molecules as ionized plasma to anisotropically remove exposed material. Photolithography is a multi-step process used to create and pattern a protective layer on thin films that prevents etching by placing either placing a protective or sacrificial barrier between the reactant and the material.

The next set of figures will outline Step 7 from Table 1 as an example of the PolyMUMPs photolithography procedure. Figure 17 shows a cross-section of the PolyMUMPs sequence up through Step 6 of Table 1, showing the 1st Oxide layer ready for photolithography.

In photolithography, the first step is to deposit a protective material on the wafer. The PolyMUMPs process can use either positive photoresist, or a combination of positive photoresist and PSG to create a conformal protective layer. If PSG is used, then it is applied first by LPCVD [6]. Then, photoresist is applied by spin coating a liquid photoresist onto the wafer and then baking the wafer at a raised temperature to dry the
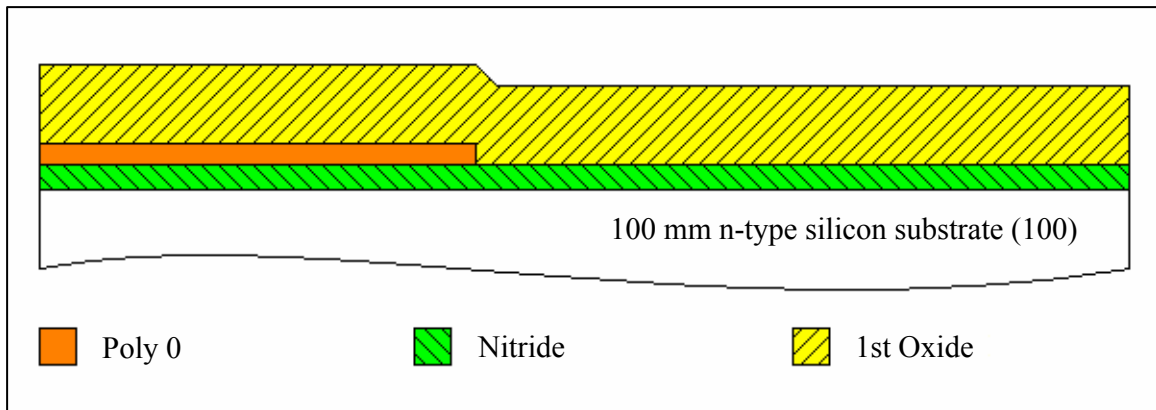
Figure 17. PolyMUMPs cross-section after 1st Oxide deposition and annealing and before photolithography.

photoresist. Figure 18 shows a cross-section of the PolyMUMPs sequence after the

photoresist has been spun on the wafer and baked to form a protective layer.

Next, the photoresist-covered wafer is exposed to ultraviolet (UV) light through a

protective patterning mask. The photoresist exposed to the UV light is then removed by

developing in a chemical bath. Figure 19 shows a cross-section of the PolyMUMPs
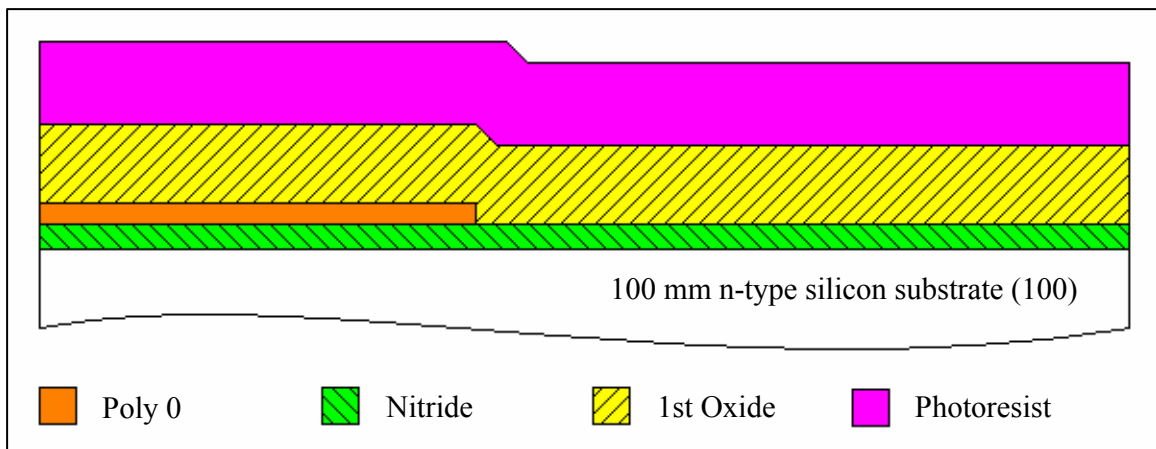
Figure 18. PolyMUMPs cross-section of 1st Oxide layer with photoresist applied.

28
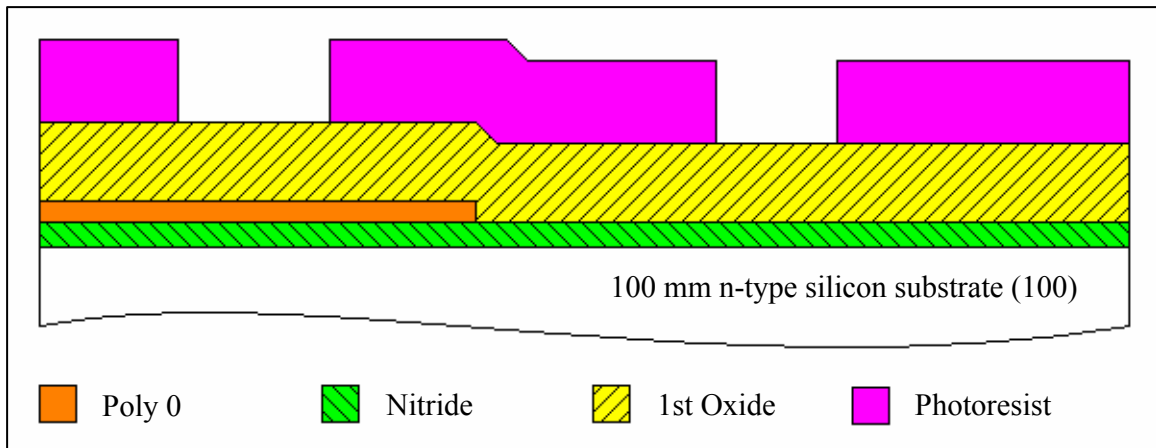
Figure 19. PolyMUMPs cross-section of 1st Oxide layer with patterned and developed photoresist.

sequence after the photoresist has been patterned by exposure to UV light through a mask and developed in a chemical bath.

After patterning and developing the photoresist, a RIE is performed to remove the unprotected material below the photoresist. When both PSG and photoresist are used as a protective layer, as in Steps 11 and 19 in Table 1, then two RIEs are performed to etch the PSG and then the material below the PSG layer. The dual protective layers of PSG and photoresist are used for cases when the photoresist cannot adequately protect the material from the RIE reactant plasma for the etch time. After the exposed material is patterned by RIE, the photoresist is stripped by chemical bath and the protective PSG is removed by RIE. Figure 20 shows a cross-section of the PolyMUMPs sequence after RIE patterning and etching of the 1st Oxide layer and removal of the photoresist. Figure 20 shows the PolyMUMPs sequence after completing Step 7 from Table 1.
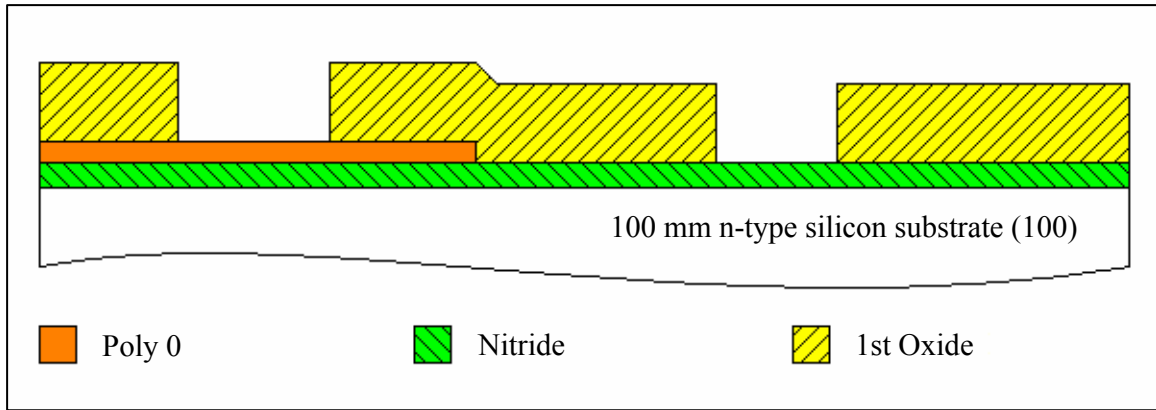
Figure 20. PolyMUMPs cross-section of 1st Oxide layer after patterning and etching.

During the PolyMUMPs processing of the wafers, the deposition steps outlined in Table 1 occur to both sides of the wafer with the exception of Step 21. The Metal evaporation step does not occur on the backside of the wafer, but all LPCVD steps deposit material on both sides, with varying PSG thicknesses occurring on the backside. Figure 21 shows a cross-section of the PolyMUMPs layers and nominal thicknesses deposited on the front and back of the wafer. The backside layers are important for the development of the Suspended Membrane Pixel Sensor design as outlined in the next section.

The completed PolyMUMPs wafers are coated with a protective layer of photoresist and diced into 1-cm^2 square chips. Fifteen copies of the chip are provided per order.

This section has covered the sequence and type of micromachining techniques used to fabricate MEMS structures as performed by MEMSCAP's PolyMUMPs service.

Frontside	Poly 2 PSG hard mask (0.2 μm)
	Poly 2 (1.5 μm)
	2nd Oxide (0.75 μm)
	Poly 1 PSG hard mask (0.2 μm)
	Poly 1 (2.0 μm)
	1st Oxide (2.0 μm)
	Poly 0 (0.5 μm)
	Nitride (0.6 μm)

100 mm, n-type silicon wafer, (100) orientation (500 – 550 μm)

Backside	Nitride (0.6 μm)
	Poly 0 (0.5 μm)
	1st Oxide (~8000 Å)
	Poly 1 (2.0 μm)
	Poly 1 PSG hard mask (~800 Å)
	2nd Oxide (~3000 Å)
	Poly 2 (1.5 μm)
	Poly 2 PSG hard mask (~800 Å)

Figure 21. PolyMUMPs cross-section of front and backside layers deposited on wafer [44].

3.3 Suspended Membrane Pixel Sensor Fabrication

This section will explain the design implemented using the PolyMUMPs service and the processing steps performed on the PolyMUMPs chips to create a Suspended Membrane Pixel Sensor. The creation of a Suspended Membrane Pixel Sensor follows these steps: 1) computer aided drawing (CAD) design and submission of the Suspended

31

Membrane Pixel Sensor PolyMUMPs layers to MEMSCAP, 2) sub-dicing of the PolyMUMPs chips into individual test die by Microdicing Technologies, 3) etching of backside layers and silicon wafer substrate, 4) securing, wire bonding, and checking the test die and package, and 5) coating the sensor package with PIP material.

Each Suspended Membrane Pixel is designed to function with the silicon substrate wafer etched away from the back of the silicon nitride layer to leave a thin film membrane that can be spin coated with the PIP material to create the Suspended Membrane Pixel Sensor. Figure 22 shows a cross-section of an ideal Suspended Membrane Pixel Sensor with PIP material. The crystalline silicon substrate is selectively etched away by an anisotropic wet etchant, leaving slanted walls formed from the remaining silicon substrate. Etching the silicon substrate forms a pixel sensor from the remaining PolyMUMPs layers and is then coated by PIP material. Poly 0 and Poly 1 electrical address lines are designed to be encased by the 1st and 2nd Oxides to electrically isolate the signal lines from cross-talk.

Using the equations from Chapter 4, Theory, the thin membrane substrate with a thin film of PIP material has a calculable heat capacity, thermal conductance, and thermal response time. Each Suspended Membrane Pixel design has parameter variations intended to change the electrical or thermal resistance of the pixel and the method of addressing individual pixels. The parameters were varied to create multiple designs to increase the possibility of fabricating a working or more optimal design. Creating multiple designs also increased the number of available test dice for use in experiments.

32
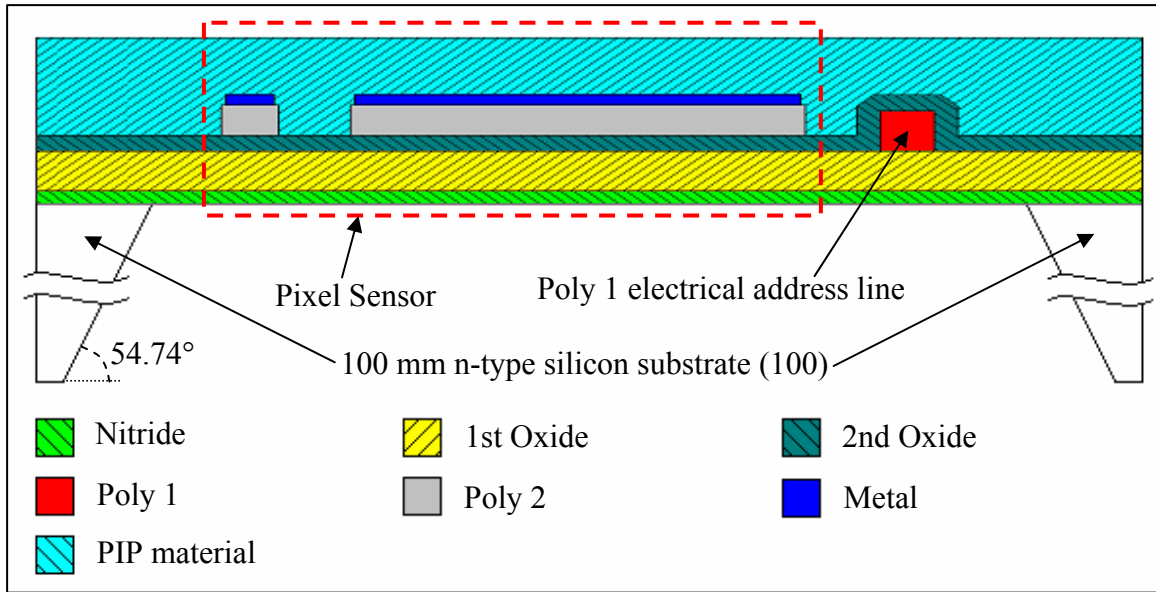
Figure 22. Cross-section of ideal Suspended Membrane Pixel Sensor showing substrate etched away by anisotropic wet etch.

The parameters varied in each design were 1) pixel "finger" spacing, 2) pixel layer composition, and 3) pixel addressing. The pixel "finger" spacing was intended to vary the overall resistance of the pixel by changing the electrical path distance of the PIP material. The pixel layer composition included or left out the Metal layer to change the thermal conductance and electrical resistance of the pixel. The pixel address lines either addressed pixel rows and columns or addressed a common row for ground and each pixel individually. The area of the pixel was chosen to balance the trade off of filling the given test space, design of the address wiring, and creating a uniform pixel array. The pixel address wiring uses Poly 0 and Poly 1 layers to run conductive lines from the pixel to bond pads. The 1st and 2nd Oxide layers, which do not conduct electricity, encase the Poly 0 and Poly 1 layers to electrically isolate the wiring from the PIP material. Figure

23 shows two Suspended Membrane Pixel CAD designs with all implemented design variations. Figure 23 part (a) shows a 190 μm x 200 μm pixel designed using the Poly 2 and Metal layers to have small pixel resistance, small gap between pixel "fingers", and common-row and common-column pixel addressing. Figure 23 part (b) shows a 190 μm x 200 μm pixel designed using Poly 2 to have large pixel resistance, large gap between pixel "fingers", and common-row and individual pixel addressing.

The designs submitted to MEMSCAP for the PolyMUMPs service are created using a CAD program called L-Edit Pro v10.0. The Suspended Membrane Pixel design layers are drafted in L-Edit and submitted to MEMSCAP. MEMSCAP uses the CAD drawings to create masks used for photolithographic patterning of the PolyMUMPs layers. MEMSCAP processes the designs through the steps outlined in Section 5.2. The
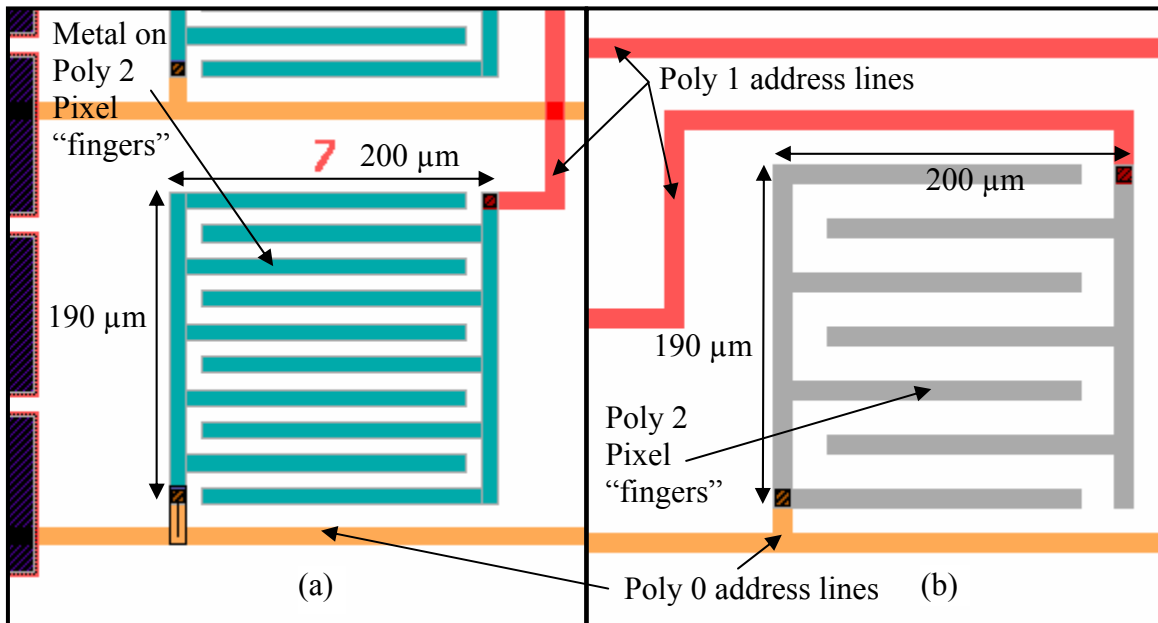
Figure 23. Two Suspended Membrane Pixel CAD designs showing multiple parameter variations.

CAD designs created for the PolyMUMPs service are constrained to a 1.9 mm x 1.9 mm square to ensure they fit within the 2 mm x 2 mm space allocated for each pixel test bed. Each 1-cm^2 square chip provided by MEMSCAP is sub-diced using a specialized micro dicing procedure implemented by the company, Micro Dicing Technology, located in Sunnyvale, CA. The 1-cm^2 square chips are sub-diced into twenty-five 2 mm x 2 mm square dice by making four vertical cuts and four horizontal cuts. A path of material approximately 10-µm wide is destroyed with each saw cut. After sub-dicing, the individual pixel test die are returned and are ready for individual processing. Figure 24 shows two example Suspended Membrane Pixel designs implemented using the PolyMUMPs process.

In order to remove the silicon substrate from the back of the PolyMUMPs design, a bulk silicon micromachining technique using an anisotropic wet etch of potassium
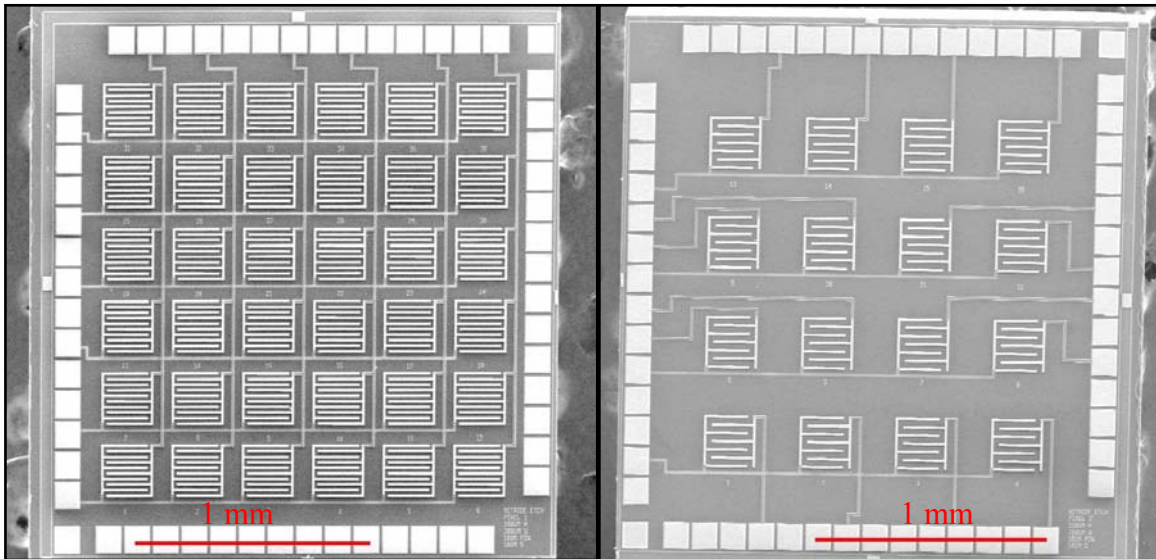
Figure 24. SEM image of two Suspended Membrane Pixel designs implemented in PolyMUMPs.

hydroxide (KOH) was chosen. This technique has demonstrated a capability to etch bulk

crystalline silicon with high selectivity to the (100) plane at a rate of 1.4 μm/minute [45].

By corresponding with a MEMSCAP technical representative, a specific recipe was

obtained of 15% KOH weight by volume (W/V) at a temperature of 80 °C, which will

etch the PolyMUMPs wafer substrate at a rate of 1.3 μm/minute [46]. The nominal

thickness of the silicon wafer is 500 – 550 μm, requiring an etch time of approximately 7

hours. Due to the small nature of the individual test die, securing the die during the wet

chemical bath at a raised temperature required a method to protect the front and sides of

the test die that can withstand the wet chemical etchant attack, raised temperature, and

aqueous conditions for several hours. It is necessary to protect the front because the

polysilicon layers that define the pixel and address wiring will be etched away if exposed

to KOH. Multiple methods of securing the PolyMUMPs test dice during wet chemical

etching were developed to find a useable method of etching a large pit on the backside of

the test dice. Several materials, including Crystal Bond, a machined sheet of stainless

steel, electrical tape, photoresist, and a UV cured polymer, were tested as new methods of

forming a protective barrier around the test dice during the wet chemical etch. Crystal

Bond is a translucent material at room temperature that becomes viscous and liquid at

high temperatures. It can be dissolved from its solid state by acetone. Crystal Bond was

heated until the material was semi-liquid and pliable, and a test die was inserted and the

material was formed around it to create a solid barrier as the Crystal Bond cooled. A

section of a stainless steel sheet metal 1-mm thick was machined with a three-by-three

array of 2 mm x 2 mm holes to protect the test dice. Photoresist was used to secure the

36

metal dice holder to a glass slide and fill in the cracks around the sides of the test dice. Electrical tape with a square hole cut out was used to secure a PolyMUMPs test die face down to a glass slide. Also, a liquid monomer was used to form an imprint of a single test die, and then cured under a UV light to form a polymer mold of the test die. A test die is inserted into the mold with a clear acetate tape covering the back side. A small hole is then cut out of the tape to expose the back side to the wet chemical etchant. Figure 25 shows examples of the methods used to hold the test dice for wet chemical etching. Figure 25 part (a) shows a test die secured to a glass slide by electrical tape. A hole is cut out to expose the back side to the wet chemical etchant. Figure 25 part (b) shows a stainless steel dice holder. Figure 25 part (c) shows a polymer mold with a test die secured using clear tape. Figure 25 part (d) shows several test dice secured in Crystal Bond to a glass slide.

The material deposition steps that PolyMUMPs performs create thin films on the reverse side of the wafer in addition to the front-side. The thicknesses are approximately the same, except for the PSG layers, which are approximately 40% of the desired front-side thickness [44]. To etch the wafer substrate with KOH, the backside layers must first be removed because the KOH solution will not appreciably etch PSG or silicon nitride. The methods tested for removing the backside layers were drilling with a 0.001"-diameter tungsten carbide drill bit, grinding with a diamond bit, and scribing with a diamond tipped scribe pen. Figure 26 shows examples of test dice with the backside layers partially removed. Figure 26 part (a) shows a test die with the backside layers removed in a three-by-three array of drill holes. Figure 26 part (b) shows a test die with

37
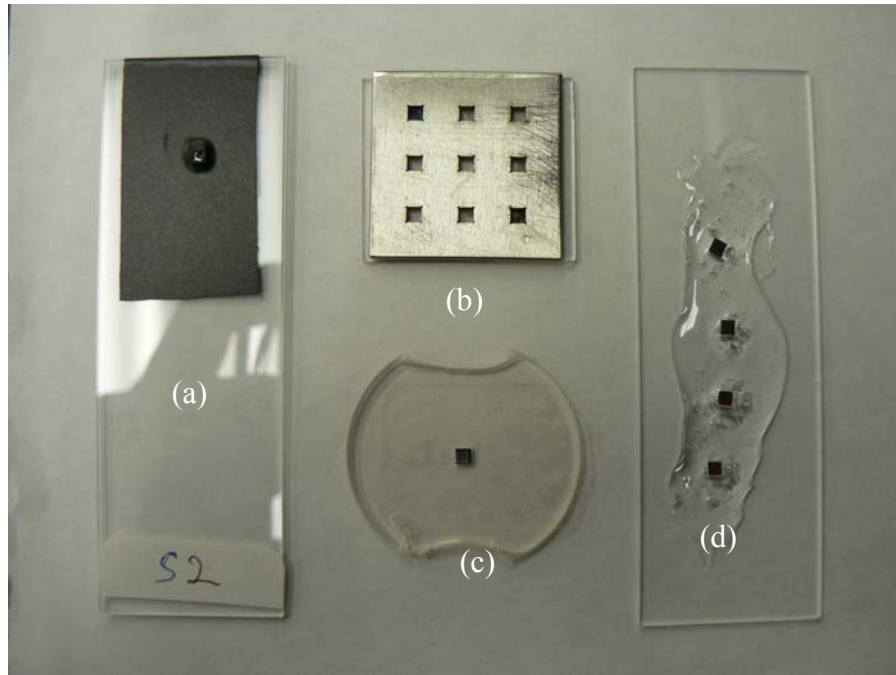
Figure 25. Picture of wet chemical etch test dice holders showing multiple materials and methods tried.

the backside layers removed by grinding using a diamond grinding bit. Figure 26 part (c)

shows a test die with the backside layers removed using a diamond tipped scribe pen.
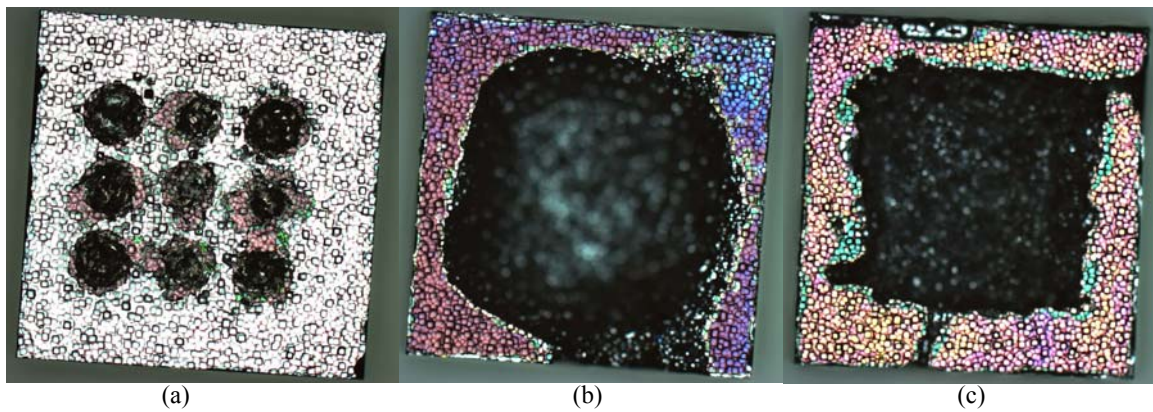
Figure 26. Picture of multiple test methods for removing the backside layers of PolyMUMPs test dice.

The wet chemical etchant was purchased in an aqueous solution of 50% KOH W/V and de-ionized water (DIW). The solution was diluted in a 1:3 ratio of 50% KOH W/V and DIW to create a 12.5% KOH W/V solution. Etch testing used both the 50% and 12.5% KOH W/V solutions. The solution is heated indirectly by placing it in a heated DIW bath on a Dataplate PMC 730 Spinner + Heater. The secured test dice are placed in the heated KOH bath for a set time, temperature, and concentration to control the etch depth and to monitor the status of the test dice. Figure 27 shows the equipment setup for wet chemical etching using a Dataplate PMC 730 Spinner + Heater, Pyrex dish, Teflon wet etchant holder, thermometer, and secured test dice.

The desired result after wet etching the test dice is a thin film membrane supported by the remaining silicon wafer substrate. The silicon wafer substrate is etched
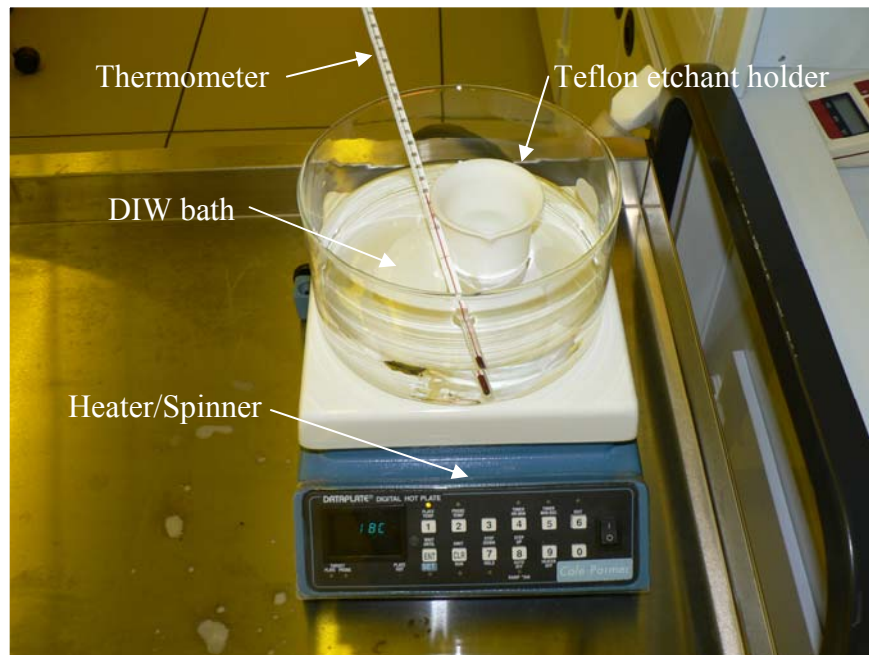
Figure 27. Picture of equipment setup used to etch PolyMUMPs test dice.

in an anisotropic manner, yielding a cavity under the remaining thin film membrane. The anisotropic etch behavior preferentially attacks the (100) crystal plane of silicon, causing the sloped walls at 54.74° due to the orientation of the (111) silicon crystal plane [45].

Wet chemical etch testing of the PolyMUMPs test dice yielded results that were unusable for creating a Suspended Membrane Pixel Sensor. The test dice secured with Crystal Bond were unintentionally released into the chemical etchant after prolonged exposure to the raised temperature bath. The raised temperature bath caused the Crystal Bond to slowly deform and break free of the glass slide, releasing or exposing an entire test die to the etchant solution. The results of multiple wet chemical etch tests using PolyMUMPs test dice secured by the stainless steel dice holder and photoresist, electrical tape, and UV cured polymer with clear tape yielded eroded or destroyed results that were similar to the etch tests using Crystal Bond to secure test dice. The test dice show indications of etchant attack on the front-side and in some cases the test dice are released into the etchant bath. The photoresist, electrical tape adhesive, and clear tape adhesive were attacked and did not withstand the etchant bath, allowing the wet chemical bath to etch the front and sides of the test dice. Examples of failed results and a discussion are included in Chapter 6, Experiments and Results.

All wet chemical etch attempts yielded unusable test dice for creating a Suspended Membrane Pixel Sensor due to front-side polysilicon etching or release and exposure of the test dice into the etchant bath. An alternative method of removing the silicon substrate without using wet chemical etching is laser-micromachining.

The Mound Laser and Photonics Center, Inc. (MLPC) perform precision laser micromachining on various microelectronics and MEMS materials, including crystalline silicon. Using precision scanning optics and control machinery, the backside of a test die was removed by heating and vaporizing the silicon wafer substrate in a controlled pattern. The laser system was a Spectra Physics YHP40-355 Q-switched Nd:YVO$_4$ laser operating at 355 nm with an objective lens focal length of 103 mm. The machining laser average power was 700 mW. A Scanlab HurrySCAN II laser beam scanner performed the laser beam scanning. The laser beam was focused to a 13-μm diameter spot and was scanned across the silicon surface until the desired depth was achieved. The typical depths achieved were between 450 – 470 μm. Attempts to etch beyond the range of 470 μm caused damage to the front-side of the test die. Due to front-side damage caused by over-machining, the etch depth limit of the laser-micromachining technique was limited to approximately 470 μm which left a layer of silicon substrate anywhere from 30-μm to 80-μm thick. The remaining silicon substrate was not accounted for in initial modeling and attempts were made to wet chemical etch the remaining silicon substrate. Examples and a discussion of results are included in Chapter 6, Experiments and Results.

After removing the backside substrate, the next step in creating a Suspended Membrane Pixel Sensor is to secure and wire bond the PolyMUMPs chip into a ceramic dual inline package (DIP). Before wire bonding, the test die is cleaned of photoresist using a 10-minute acetone bath followed by a rinse in isopropyl alcohol, a rinse in methanol, and then dried with pressurized nitrogen. The clean chips are secured to a ceramic DIP using a thin layer of common Super Glue, ensuring that the glue doesn't fill

the backside etched cavity. The glue is allowed to dry overnight and secure the test die to the package. The test die is wire bonded to the DIP with an F&K Delvotek Model 5410 using 0.001-inch diameter gold wire at a vacuum chuck substrate temperature of 175 °C. Figure 28 part (a) shows the F&K Delvotek Model 5410, vacuum pump, vacuum/heater chuck, ultrasonic generator, flame-off unit, and viewing optics. Figure 28 part (b) shows a close-up of the vacuum/heater chuck with a stainless steel vacuum spacer for DIPs and a sample DIP with test die.

If a test die package is not properly secured during the wire bonding process, the possibility of electrical shorts developing increases significantly. The F&K Delvotek Model 5410 uses ultrasonic vibration, heat, and force to bond the gold wire to the target substrate. An improperly secured test die package can cause invisible electrical shorts to develop between bond pads and the test die wafer substrate. A properly secured test die

(a)   (b)
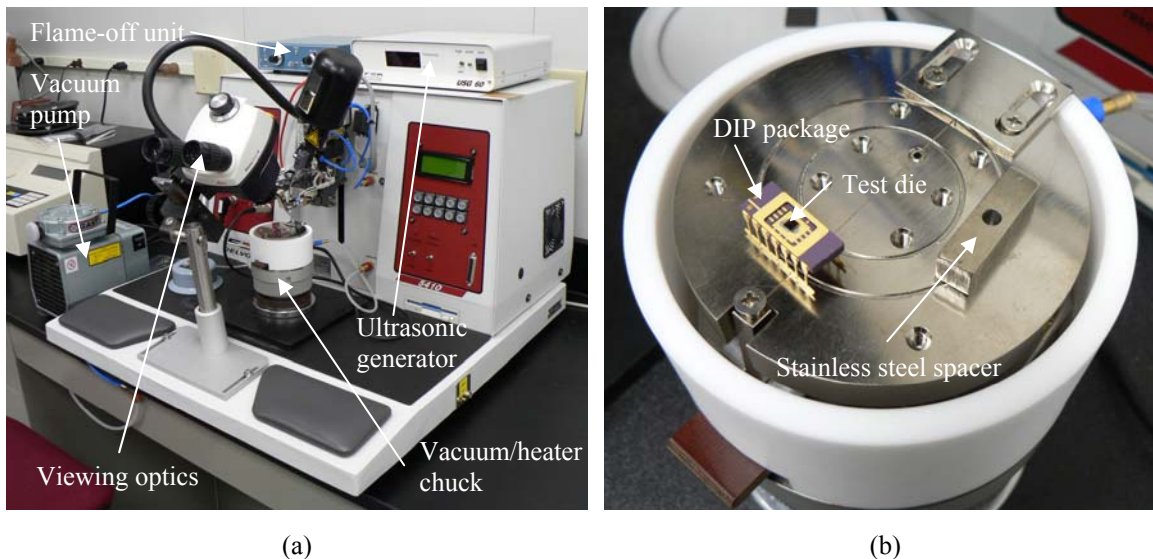
Figure 28. Picture of wire bonding setup and close-up of vacuum/heater chuck with stainless steel DIP spacer and sample DIP with test die.

package should have a secure vacuum seal between the package body and the stainless steel spacer. A proper bond created by the wire bonder depends on a balanced trade-off of ultrasonic power, bond time, substrate temperature, and bond force. Increasing the ultrasonic power, bond time, and bond force will increase the risk of developing electrical shorts if the package is improperly secured. Several packaged test dice were found to have intermittent electrical shorts with resistances varying between a few $k\Omega$ and several $M\Omega$, between several random test points on the PolyMUMPs test dice. By reducing the ultrasonic vibration power and applied force while raising the heater temperature, the occurrence of electrical shorts was minimized or altogether eliminated from the wire bonding process. After wire-bonding a test die to a ceramic DIP, the sensor package pins were tested for electrical shorts using an Agilent Model 34401A 6 ½ Digit Digital Multimeter.

Once the test die is secured, wire bonded to the DIP, and tested for short circuits, the sensor package is ready for PIP material application. The PIP material is applied by pipette to the packaged test die and then spin coated onto the sensor package using a Solitec Photoresist Spinner. In order to evenly apply a PIP layer approximately 1 μm thick, the PIP material is spun onto the sensor package at a rate of 4000 rpm for 30 seconds. Figure 29 shows a picture of the Solitec Photoresist Spinner control module and vacuum chuck spinner assembly.

The sensor package with applied PIP is dried at ambient room conditions. A completed Suspended Membrane Pixel Sensor is then ready to be tested to experimentally derive the figures of merit.

43

Figure 29. Solitec Photoresist Spinner used to apply PIP material to packaged test dice.

This section outlined the CAD design process of the Suspended Membrane Pixel Sensor, the methods of removing the wafer substrate from test dice using a wet chemical etch and laser-micromachining, the wire bonding and short circuit testing of packaged test dice, and the method of applying the PIP material to the completed sensor package.

3.4 Raised Cantilever Arm Pixel Sensor Fabrication

This section will explain the design implemented using the PolyMUMPs service and the processing steps performed on the PolyMUMPs chips to create a Raised Cantilever Arm Pixel Sensor. The creation of a Raised Cantilever Arm Pixel Sensor follows these steps: 1) CAD design and submission of the Raised Cantilever Arm Pixel Sensor PolyMUMPs layers to MEMSCAP, 2) sub-dicing of the PolyMUMPs chips into individual test die by Microdicing Technologies, 3) hydrofluoric (HF) acid release of test dice, 4) securing, wire bonding, and checking the test die and package, and 5) spin coating the sensor package with PIP material.

Each Raised Cantilever Arm Pixel is designed to thermally isolate each pixel from the substrate by raising the pixel using residual stress cantilever arms. The raised pixel is

designed to act as a platform when the PIP material is spun onto the Raised Cantilever Arm Pixel Sensor, creating pixel sensors thermally isolated from the substrate. Each Raised Cantilever Arm Pixel design has varied parameters that change the pixel resistance, pixel height from the substrate, pixel area, and pixel addressing method. The parameters were varied to create multiple designs to increase the possibility of fabricating a working or more optimal design. Creating multiple designs also increased the number of available test dice for use in experiments. The design parameters that were varied are 1) number of cantilever arm sections, 2) cantilever arm section length, 3) cantilever arm section width, 4) pixel "finger" spacing, 5) pixel area, and 6) pixel addressing. There were forty-eight individual pixel designs created by combining the different design parameters. The number of cantilever arm sections and arm section length controlled the overall length of the residual stress arms. The longer distance along the length of the cantilever arms the pixel "fingers" were, the higher the pixel will be suspended from the substrate, increasing the pixels thermal isolation from the substrate. The cantilever arm width was changed to add resiliency to the cantilever arms in case spinning the PIP material onto the pixel might damage the cantilever arms sections. The pixel "finger" spacing was varied to examine the effects of catching and retaining the PIP material in the pixel area. The pixel "finger" spacing also varied the volume of polysilicon in the pixel, changing the heat capacitance value of the pixel. The pixel area was varied to increase the sensitivity of the pixel designs. The pixel address lines either addressed pixel rows and columns or addressed a common row for ground and each pixel individually. The Raised Cantilever Arm Pixel design requires that the sacrificial PSG

45

layers are removed to release the residual stress pixel structures. The PSG layers were removed by wet chemical etching in HF, which removes all silicon oxide from the test dice, exposing the Poly 0 and Poly 2 addressing lines to the PIP material when spin coating. Figure 30 shows two Raised Cantilever Arm Pixel CAD designs. Figure 30 part (a) shows a Raised Cantilever Arm Pixel CAD design with three cantilever arm sections of 75-µm length and 12-µm width, 1-µm pixel "finger" spacing, and maximized pixel area. Figure 30 part (b) shows a Raised Cantilever Arm Pixel CAD design with two cantilever arm sections of 100-µm length and 6-µm width, 3-µm pixel "finger" spacing, and maximized pixel area.

The CAD design and submission to MEMSCAP of the Raised Cantilever Arm Pixel Sensor follows the same procedure as the Suspended Membrane Pixel Sensor
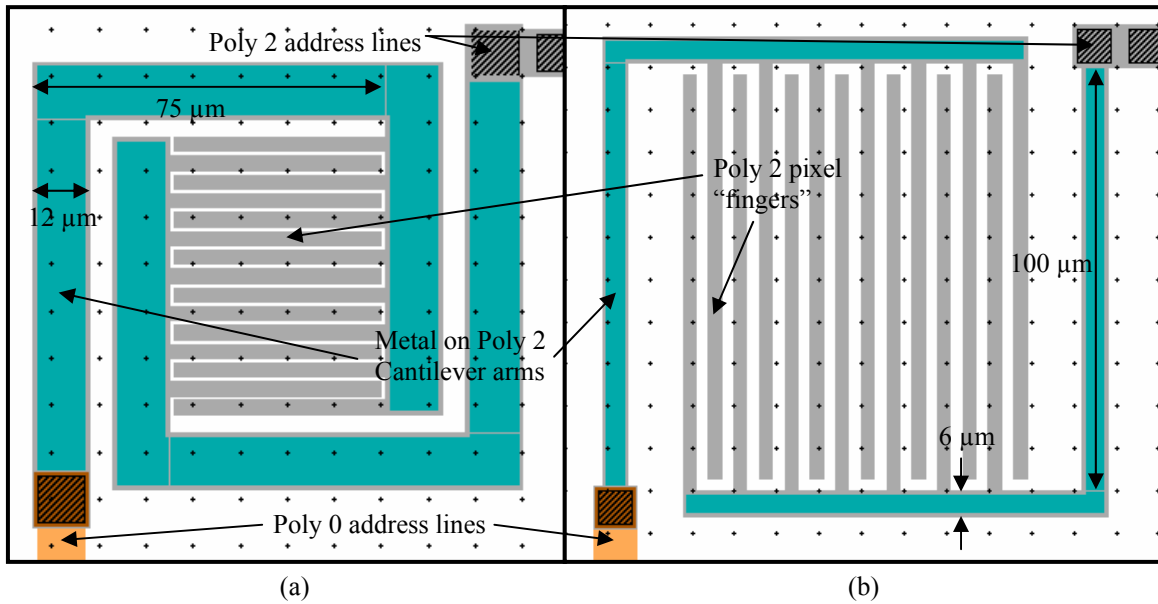
Figure 30. Two Raised Cantilever Arm Pixel CAD designs showing multiple parameter variations.

design outlined in Section 3.3. The sub-dicing of the PolyMUMPs chips also follows the same procedure as the Suspended Membrane Pixel Sensor outlined in Section 3.3. The sub-diced test dice are then ready for the release process. Figure 31 shows two example Raised Cantilever Arm Pixel designs implemented using the PolyMUMPs process.

The design submitted for the PolyMUMPs process shown in Figure 30 part (a) has Poly 2 pixel "finger" spacing of 1 μm. Spacing of less than 2 μm violates the PolyMUMPs minimum spacing design rule for Poly 2 structures. By unintentionally violating the design rule, the PolyMUMPs mask error tolerances were larger than the 1-μm space allowed for, causing the pixel area to be a solid Poly 2 structure instead of interdigitated fingers. The dashed boxes in Figure 31 are solid Poly 2 pixels fabricated with the 1-μm design error. The solid pixels are low resistance electrical pathways compared to the PIP material resistance, effectively shorting the pixel bias current and rendering the pixel useless. There were sixteen individual pixel designs that incorporated the 1-μm design error, rendering those pixel designs useless.

The PSG layers on the PolyMUMPs test dice are designed to act as sacrificial layers that can be removed through a wet chemical etch without attacking other layers or features on the chip. The release process follows these steps: 1) clean off photoresist in 10-minute acetone bath, 2) briefly dip and rinse in DIW, 3) 3 ½-minute bath in 48% HF W/V, 4) briefly dip and rinse in 3:1 methanol:DIW, 5) dry chips in AutoSamdri-815B Supercritical CO_2 Dryer. The AutoSamdri-815B Supercritical CO_2 Dryer is an automated critical point CO_2 dryer that dries the test dice in an environment designed to
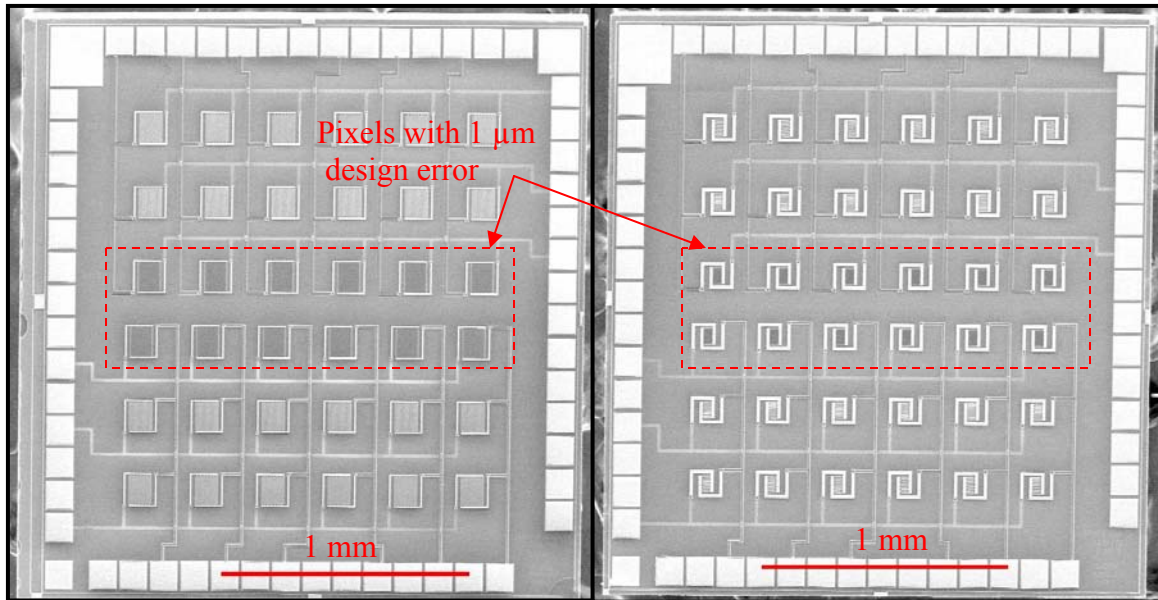
Figure 31. SEM image of two Raised Cantilever Arm Pixel designs implemented in PolyMUMPs.

prevent stiction. Stiction is caused when surface tension forces pull raised or suspended structures into contact with the substrate and prevent return movement. Figure 32 shows a picture of the setup for releasing PolyMUMPs test dice, including acetone, methanol, 48% HF W/V, test dice holder, Teflon chemical beakers, and AutoSamdri-815B Supercritical CO_2 Dryer.

The release process removes the sacrificial PSG layers, allowing the residual stress cantilever arms to bend upward, raising the pixels. The test dice are then ready to be wire bonded and spin coated. The fabrication of the Raised Cantilever Arm Pixel Sensors follows the same wire bonding and spin coating processes as described in Section 3.3 for the Suspended Membrane Pixel Sensor.
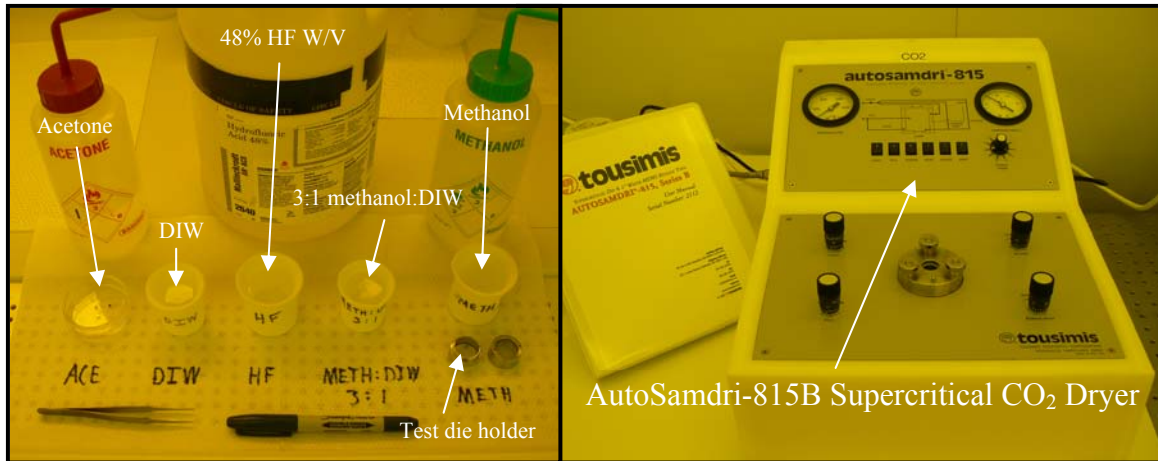
Figure 32. Picture of PolyMUMPs release setup and AutoSamdri-815B Supercritical CO_2 Dryer.

This section outlined the CAD design process of the Raised Cantilever Arm Pixel Sensor, the sacrificial layer removal process, the wire bonding and short circuit testing of packaged test dice, and the method of applying the PIP to completed sensor packages.

3.5 Summary

This chapter describes the micromachining techniques used by the PolyMUMPs service to create the MEMS structures for the Suspended Membrane Pixel Sensor and the Raised Cantilever Arm Pixel Sensor. The Suspended Membrane Pixel Sensor is a thin film membrane of silicon nitride, polysilicon, and PSG coated with PIP material. The thin film membrane structure isolates pixel address wiring and defines a pixel area. The post foundry processes used to create the Suspended Membrane Pixel Sensor are sub-dicing, backside wafer substrate removal, wire bonding and short circuit checking, and spin coating with PIP material. The Raised Cantilever Arm Pixel Sensor is gold and polysilicon residual stress cantilever arms with polysilicon "fingers" holding PIP material

as pixels. The processes for creating a Raised Cantilever Arm Pixel Sensor are sub-

dicing, sacrificial layer removal, wire bonding and short circuit checking, and spin

coating with PIP.

IV. Theory

4.1 Chapter Overview

The purpose of this chapter is to provide an overview of the theory of heat transfer, IR sensor figures of merit and residual stress, and how each is applied to the creation of the microbolometer model.

4.2 Heat Transfer

The general pixel sensor model is shown in Figure 33. The general model begins with the pixel, ambient environment, PIP material coating the sensor, and the substrate each at a different temperature. The methods of heat transfer into and out of the system are by radiation, convection, and conduction. Heat transfer by convection and conduction occurs between objects of dissimilar temperature, where power (q) flows from the highest temperature objects to the lower temperature objects.
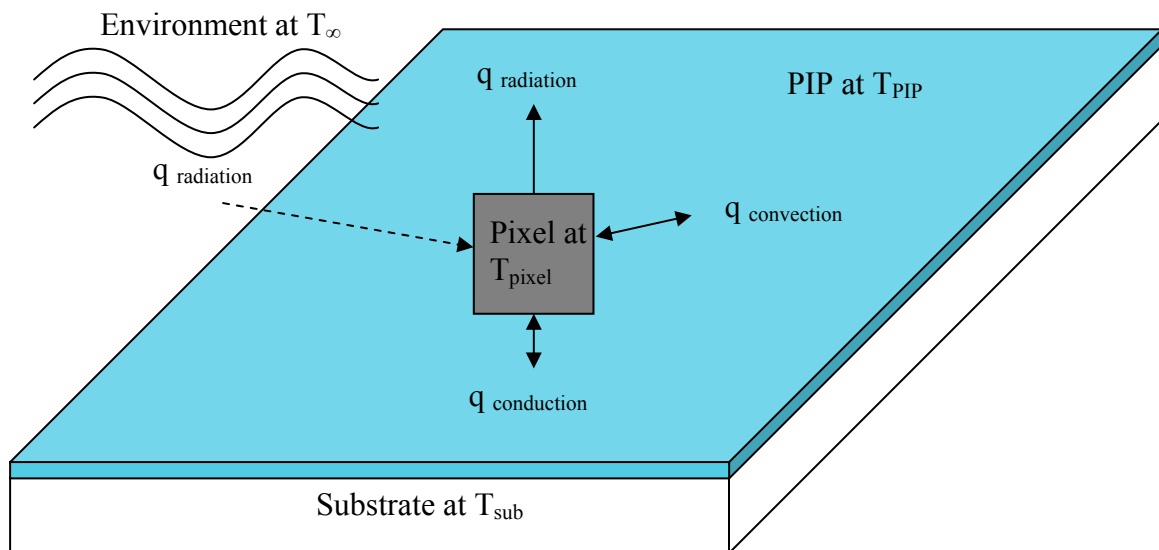
Figure 33. Diagram of general heat transfer model.

Using the theory of heat transfer, a heat balance equation can be used to describe the flow of heat within the microbolometer system. Starting with Fourier's heat transfer equation in differential form, shown in Equation (1), applying assumptions will yield an equation that can be used to describe indirect thermal transduction for a resistive bolometer:

$$\frac{dQ}{dt} = -kA\frac{dT}{dL}$$ (1)

where dQ/dt is change in energy over change in time, k is the thermal conductivity of the material, A is the cross-sectional area normal to the heat flow, and dT/dL is the change in temperature per unit length through the material [47].

For a specific case of Fourier's heat transfer equation assuming no heat loss through the sides of an object, Equation (2) describes the quantity of heat flow conducting through a medium:

$$q_{cond} = \frac{kA(T_2 - T_1)}{L}$$ (2)

where q_{cond} is heat power, T_2 is the higher temperature end of the solid, T_1 is the lower temperature end of the solid, and L is the length of the solid [47]. By examining the microbolometer system as a lumped heat capacitance system, individual materials will have a thermal conductance, G, or its inverse, a thermal resistance, R, that can be defined by [47]:

$$G = \frac{1}{R} = \frac{kA}{L}.$$ (3)

In the case of small sources of heat conducting through a medium that is very large relative to the heat source, Equation (4) describes a change applied to Equation (2):

$$\Delta T = T_2 - T_1 = q(R_{Ts} + R_T) \tag{4}$$

where q is the heat power loss, R_{Ts} is an additional thermal resistance added, and R_T is the thermal resistance of the conducting body [48].

For a square heat source, the additional thermal resistance added can be described by:

$$R_{Ts} = \frac{0.55}{Lk} \tag{5}$$

where L is the side length of the square [48].

Heat can also flow by convection away from the microbolometer pixel. In such a case, the heat flow is described by:

$$q_{conv} = \bar{h} A (T_S - T_f) \tag{6}$$

where $\bar{h}$ is the average heat transfer coefficient, A is the surface area, T_S is the surface temperature, and T_f is the fluid temperature [49].

In a similar manner to conduction, the thermal convection coefficients in Equation (6) can be viewed as effective thermal resistances or conductances by the lumped heat capacitance model, expressed by:

$$G = \frac{1}{R} = \bar{h} A . \tag{7}$$

The convective heat transfer coefficient, $\bar{h}$, is described by a series of experimentally derived relationships. The equations describing $\bar{h}$ are dependent on the

calculation of the Nusselt and Rayleigh numbers for the fluid undergoing convection.

Equation (8) describes the Rayleigh number for natural convection from a rectangular

plate in which the surface of the plate is hotter than the fluid in contact with the plate:

$$Ra_L = \frac{g\beta}{\alpha v} L_c^3 \left(T_S - T_f\right) \qquad (8)$$

where g is gravitational acceleration, β is coefficient of volume expansion, α is thermal

diffusivity of the fluid, v is kinematic viscosity of the fluid, and L_c is characteristic length.

The characteristic length for a hot rectangular plate in contact with a cooler fluid is

defined as the surface area of the plate divided by the perimeter of the plate [49].

For reasonable ranges of values for characteristic lengths of micro-sized pixels

and small temperature differences, the average Nusselt number is assumed to be

described by [49]:

$$\overline{Nu}_L = 0.54 \, Ra_L^{\frac{1}{4}}. \qquad (9)$$

The average heat transfer coefficient is described by [49]:

$$\overline{h} = \overline{Nu}_L \frac{k}{L_c}. \qquad (10)$$

The basic equations of heat transfer form a comprehensive description of the heat

flow of the microbolometer.

4.3 Figures of Merit

The derivation of the figures of merit begins with the differential Fourier heat

equation and assumptions of the significant heat loss paths. The assumptions are that the

dominant heat loss paths are through thermal conductance of the legs of the bolometer

(for the Raised Cantilever Arm Pixel), thermal conductance through the pixel area to underlying layers (for Suspended Membrane Pixel), conduction through the air gap underneath the pixel (for the Raised Cantilever Arm Pixel), and convection from the top surface of the pixel (both pixel types) and that the primary source of heat is from incident radiation. From the Fourier heat equation and these assumptions, the Fourier heat equation can be expressed through:

$$C \frac{d(\Delta T)}{dt} + G_{total} (\Delta T) = \eta \beta_f A_D P_o \exp(j\omega t) \tag{11}$$

where C is the heat capacity of the pixel, ΔT is the temperature difference between a heat source and heat sink, G_{total} is the sum of effective thermal conductances, η is the absorptance, β_f is the fill factor of the pixel, A_D is the pixel area, P_o is the total incident radiant power, t is time, and ω is the angular modulation frequency of the incident radiation. The steady-state solution to Equation (11) is:

$$\Delta T = \frac{\eta \beta_f A_D P_o}{G_{total} \sqrt{1 + \omega^2 \tau_T^2}} \tag{12}$$

where τ_T is the thermal response time defined as C/G_{total} [29].

The basic equations needed for the figures of merit have been established using the Fourier heat transfer equation and operating assumptions of the microbolometer and its material structure.

4.3.1 Responsivity and Time Constant. The microbolometer responsivity, shown in Equation (13), is defined as the output signal voltage, V_s, from a pixel divided by the incident radiant power, P_o, falling on the pixel [50]:

55

$$\Re = \frac{V_s}{P_o}. \qquad (13)$$

To process the sensor signal, a bias current is required to complete the electrical modeling of the bolometer readout circuit. The only effective change is that the previous thermal conductance, G, adds the heating effect of dissipating electrical power and can be modeled as an effective thermal conductance, G_{total}, shown as:

$$G_{total} = G - G_0 \left(T_1 - T_0 \right) \alpha_R \left(\frac{R_L - R_S}{R_L + R_S} \right) \qquad (14)$$

where G_0 is the average thermal conductance through a medium from the bolometer at temperature, T_1, to its surroundings at temperature, T_0, α_R is the temperature coefficient of resistance, R_L is the load resistance of the circuit, and R_B is the bolometer resistance [29]. The temperature coefficient of resistance (TCR) is defined as:

$$\alpha_R = \frac{1}{R_B} \frac{dR_B}{dT}. \qquad (15)$$

Assuming the TCR is independent of temperature allows the responsivity to be expressed in terms of the thermal properties derived from the heat equation and measurable properties of the bolometer pixel, shown as:

$$\Re = \frac{\alpha_R \beta_f i_B R_B}{G_{total} \sqrt{1 + \omega^2 \tau_T^2}} \qquad (16)$$

where i_B is the bias current and τ_T is the thermal time constant redefined in terms of the average thermal conductance [5].

56

4.3.2 Detectivity and Noise Equivalent Power. The microbolometer detectivity and NEP are closely related to the responsivity. Given the responsivity, the NEP can be defined as the required irradiant power on the pixel that generates an equivalent signal equal to the rms pixel noise within the system bandwidth, or a signal-to-noise ratio (SNR) of 1. For a resistive bolometer, the pixel noise is characterized by the total mean square noise voltage which is the sum of the squares of Johnson noise, temperature fluctuation noise, 1/f noise, and background fluctuation noise [5,29,51].

The mean squared Johnson noise is expressed as:

$$\overline{V_J^2} = 4k_B T R_B B \tag{17}$$

where k_B is Boltzmann's constant, T is the temperature of the pixel, and B is the noise bandwidth expressed as $1/(2\Delta t)$ where Δt is the bias pulse duration [5].

The mean squared temperature fluctuation noise is expressed as [29]:

$$\overline{V_{TF}^2} = \frac{4k_B TG\Re^2}{\eta} \tag{18}$$

The 1/f noise is an experimentally observed phenomenon that appears to be affected by non-ohmic electrode contacts and is expressed as:

$$V_f = i_f R_B \propto R_B \sqrt{\frac{\overline{i^{\sim 2}} B}{f^{\sim 1}}} \tag{19}$$

where $\overline{i}$ is the DC bias current and f is the modulation frequency [51]. Since the 1/f noise is an experimentally observed phenomenon, the exponent values for modulation frequency and DC bias current are approximated in the proportional relationship.

The background fluctuation noise can be expressed as:

$$\overline{V_{BF}^2} = 8A_D\eta\sigma k_B\left(T_{pixel}^5 + T_B^5\right)\mathfrak{R}^2 \tag{20}$$

where σ is the Stefan-Boltzmann constant, T_{pixel} is the pixel temperature, and T_B is the image background temperature [29]. For modeling purposes, the Johnson noise was assumed to be the largest significant noise source by purposely adjusting parameters so that the responsivity and bolometer resistance are dominant over all other parameters and, thus, the temperature fluctuation and background fluctuation noises will not significantly contribute to the total mean square noise voltage. The bias signal for the pixel is an AC current signal, so 1/f noise is not expected to contribute to the overall system noise.

Combining the expressions for responsivity and total mean square noise voltage the expression for NEP is shown as:

$$NEP = \frac{\sqrt{\overline{V_N^2}}}{\mathfrak{R}} \tag{21}$$

where V_N is the total noise voltage.

Detectivity is a normalized responsivity for system bandwidth, B, and pixel area, A_D, shown as [50]:

$$D* = \frac{\sqrt{\beta_f A_D B}}{NEP}. \tag{22}$$

4.3.3 Noise Equivalent Temperature Difference. While responsivity is a measure of power sensitivity, noise equivalent temperature difference (NETD) is a measure of object and background temperature sensitivity and is expressed by:

58

$$NETD = \frac{4F^2 V_N}{\tau_0 A_D \Re\left(\dfrac{\Delta P}{\Delta T}\right)_{\lambda_1 - \lambda_2}}$$

(23)

where F is the focal ratio of the optics, τ_0 is the transmittance of the optics, and

$\left(\dfrac{\Delta P}{\Delta T}\right)_{\lambda_1 - \lambda_2}$ is the change in power per unit area radiated by a blackbody at temperature, T,

with respect to T, measured within the spectral band from λ_1-λ_2 [50].

4.4 Residual Stress Cantilevers

The design of the Raised Cantilever Pixel uses residual stress between the Metal

and Poly 2 layers to calculate the distance that the pixel will be above the substrate for

the purposes of modeling conduction and convection from the pixel to the substrate and

its surroundings. Figure 34 shows a diagram of a two-layer system of differing stresses.

Equation (24) expresses the Timoshenko radius of curvature for a two-layer

system of differing residual stresses:
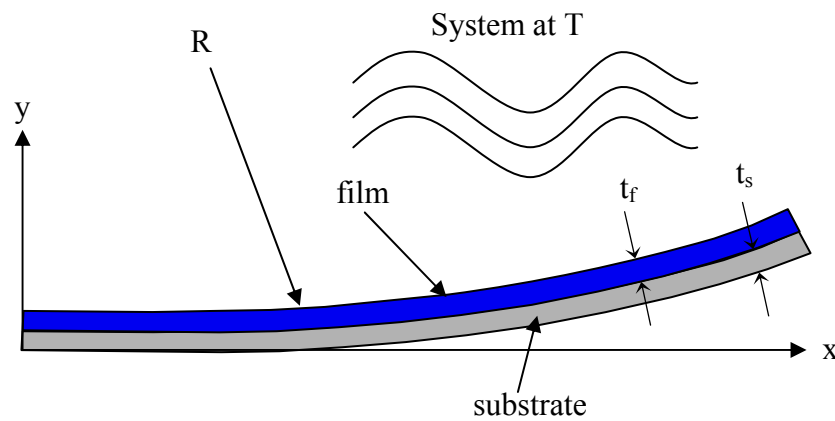
Figure 34. Diagram of two-layer system of differing stresses.

$$R = \frac{\left(t_s + t_f\right)^3}{6\left(\alpha_{substrate} - \alpha_{film}\right)\left(T - T_0\right)t_s t_f} \tag{24}$$

where t_s is the substrate thickness, t_f is the film thickness, $\alpha_{substrate}$ is the substrate temperature coefficient of expansion, α_{film} is the film temperature coefficient of expansion, T is the temperature of the system, and T_0 is the zero misfit strain temperature [52].

The zero misfit strain temperature can also be represented by:

$$T_0 = T - \frac{\sigma_{thermal}}{E'_{film}\left(\alpha_{substrate} - \alpha_{film}\right)} \tag{25}$$

where E'_{film} is the Biaxial Modulus of the film and $\sigma_{thermal}$ is the effective thermal stress of the overall system. The Biaxial Modulus of the film is expressed in Equation (26) as a function of Young's Modulus and Poisson's Ratio:

$$E'_{film} = \frac{E_{film}}{1 - v_{film}} \tag{26}$$

where E_{film} is Young's Modulus of the film and v_{film} is Poisson's Ratio of the film [52].

The thermal stress of the system can be expressed in terms of the stresses of the film and the substrate as shown as:

$$\sigma_{thermal} = \sigma_{residual} - \sigma_{internal} \tag{27}$$

where $\sigma_{residual}$ is the stress of the film and $\sigma_{internal}$ is the stress of the substrate [52].

The Timoshenko radius of curvature can then be used to calculate the displacement of the pixel cantilever arm at any point along the length of the cantilever

arm. Equation (28) expresses the vertical displacement as a function of the length of the arm:

$$y = \frac{1}{2R} x^2$$

(28)

where y is the vertical displacement and x is the distance along the cantilever arm [52].

4.5 Summary

Starting with the Fourier heat equation and using the principles of heat transfer, this chapter outlines the basic equations used to derive the figures of merit. Chapter 4, Theory also included residual stress theory to complete the model of a pixel suspended from the substrate by cantilever arms. The figures of merit are measures by which similar photonic and thermal detectors can be compared, and are qualitative measures of sensor performance. The figures of merit are the main focus for modeling and characterization purposes.

V. Modeling

5.1 Chapter Overview

The purpose of this chapter is to provide the derivation of models for heat transfer and residual stress displacement. The models with pixel parameters and material property values provide estimated figures of merit to compare to measured performance and evaluate the accuracy of the models and data input into the models.

5.2 Heat Transfer Model

The heat transfer model of a pixel in steady state heat transfer is derived from Equation (11). Figure 35 shows a general heat transfer model that assumes the primary heat input method is by incident IR radiation. Figure 35 shows heat power transfer through conduction, convection, and radiation to the substrate and surrounding environment due to temperature differences between the pixel, substrate, and environment. The heat power (q) is shown transferring through several different paths of differing materials and methods. Each pixel model includes different heat loss mechanisms for each of the two types of designs. Each heat loss mechanism acts in an additive manner and can be expressed through a single total thermal conductive loss, as mentioned in Section 4.3. For the Suspended Membrane Pixel Model, the heat loss mechanisms are by convection, conduction through substrate, conduction through PIP material to the substrate, and conduction through Poly 0, Poly 1, Oxide 1, Oxide 2, and Nitride PolyMUMPs layers to the substrate. For the Raised Cantilever Arm Pixel Model, the heat loss mechanisms are by convection, conduction through air below the pixel to

62

Environment at T_∞

q radiation loss

q convection

PIP at T_{PIP}

q conduction substrate

q radiation IR

Pixel at T_{pixel}

q conduction silcon dioxide

q conduction air gap

q conduction silicon nitride

q conduction PIP

q conduction polysilicon

q conduction metal
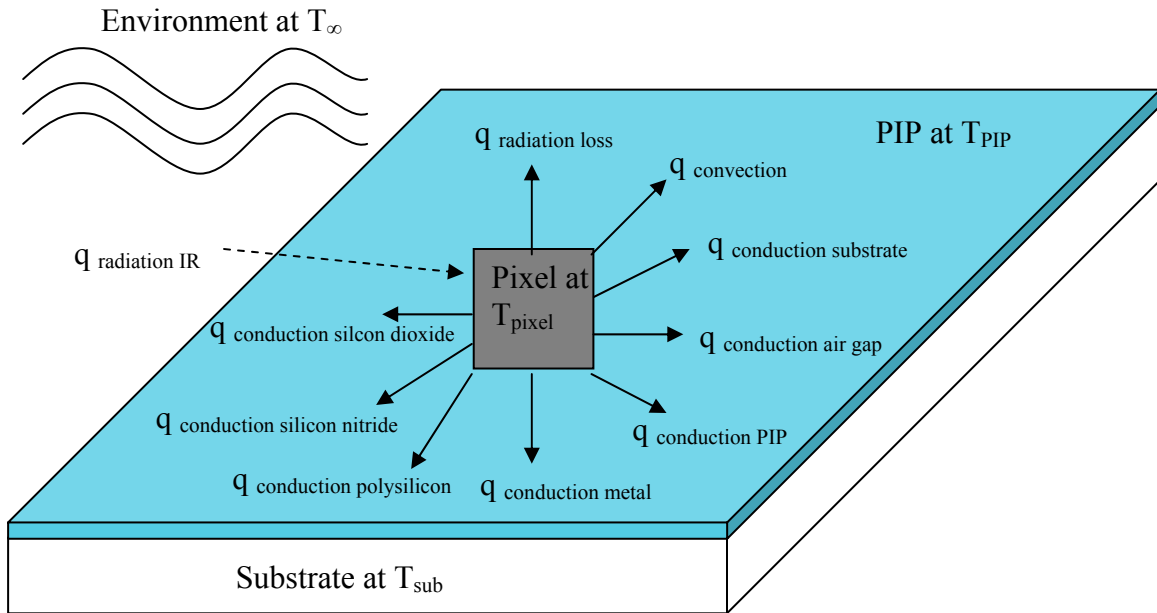
Substrate at T_{sub}

Figure 35. Heat transfer diagram of heat gains and losses due to radiation, convection, and conduction.

the substrate, and conduction through the PIP material, the Metal layer, and the Poly 2 layer to the substrate.

5.3 Residual Stress Displacement Model

The purpose of the Residual Stress Displacement Model is to provide a pixel height above the substrate for the Raised Cantilever Arm Pixel Model. The pixel height is used to calculate the thermal conduction from the pixel to the PIP material covering the substrate through the air gap beneath the pixel. The PIP material is primarily composed of polyvinyl alcohol, and for the purposes of modeling, the PIP material is considered to have identical physical properties. The film layer is the PolyMUMPs Metal layer which is composed of chromium and gold. For the purposes of modeling, the film properties

are assumed to be that of gold. The substrate layer is the PolyMUMPs Poly 2 layer

which is composed of PSG. For the purposes of modeling, the substrate properties are

assumed to be that of polysilicon. Rearranging and substituting the zero misfit strain

temperature, T_0, Equation (25), and substituting the Biaxial Modulus of the film, E'_{film},

Equation (26), into Equation (24) yields a new radius of curvature, R, shown as:

$$R = \frac{E_{film}\left(t_s + t_f\right)^3}{6\left(1 - v_{film}\right)\sigma_{thermal}t_s t_f}. \tag{29}$$

Using Equations (27), (28), and (29), a pixel displacement is calculated using

stress data and material layer thicknesses provided by MEMSCAP and nominal material

properties. Table 2 summarizes the material properties, stress data, and nominal

dimensions applied to the Residual Stress Displacement Model equations to yield a pixel

displacement.

The cantilever arm height above the PolyMUMPs Nitride layer for a total

cantilever arm length, x, of 225 μm, is the post height, h, which is the thickness of the 1st

and 2nd Oxide layers, totaling 1.75 μm, plus the calculated Residual Stress Pixel

Displacement, y_{max}, totaling 4.30 μm, which is 6.05 μm. The cantilever arm height is

modeled as the thermal conductance path length of the air gap below the pixel.

Table 2. Material property values, MEMSCAP stress data, MEMSCAP nominal
dimensions, and calculated Residual Stress Pixel Displacement.

Material Property[53,54]		Cantilever Dimensions		Calculated values	
E_{film} [GPa]	78	t_s [μm]	1.50	$\sigma_{thermal}$ [MPa]	36 tensile
v_{film} [unitless]	0.35	t_f [μm]	0.52	R [μm]	5880.98
$\sigma_{internal}$ [MPa]	15 compressive	x [μm]	225	y [μm]	4.30
$\sigma_{residual}$ [MPa]	21 tensile				

5.4 Raised Cantilever Arm Pixel Figures of Merit

The calculated figures of merit for the Raised Cantilever Arm Pixel assume that the MEMS structures are uniformly coated with a thin film of PIP, applied by spin coating. Incident IR radiation will heat the pixel and cause a difference in temperature between the pixel and the substrate. The heat capacity and thermal loss paths of the pixel system will determine the thermal time constant described in Section 4-3. The heat capacity of the pixel system is described entirely by the volume, density, and specific heat of the materials. The primary thermal loss paths for the Raised Cantilever Arm Pixel are conduction through the two cantilever arms, conduction through the air gap below the pixel, and convection from the pixel surface. Re-radiation is assumed to be negligible compared to other thermal loss paths. Figure 36 shows the general form of the Raised Cantilever Arm Pixel System including design variables and a cross-section view of the pixel, thin films, and substrate.

Assuming that the temperature of the substrate (T_{sub}) and the temperature of the environment (T_∞) are equal, the temperature difference will be highest at the pixel (T_{pixel}) and lowest at the substrate. The temperature difference causes a positive heat flow away from the pixel to the environment by convection and to the substrate by conduction. The total thermal loss paths can be represented by G_{total} from Equation (11), which is the summation of the thermal conductance's and effective conductance's expressed by Equations (3) and (7). The total heat capacitance, C_{total}, and the total effective thermal conductance, G_{total}, are the components that describe the thermal time constant, τ_T. Equations (8), (9), and (10) describe the calculations used for the Rayleigh
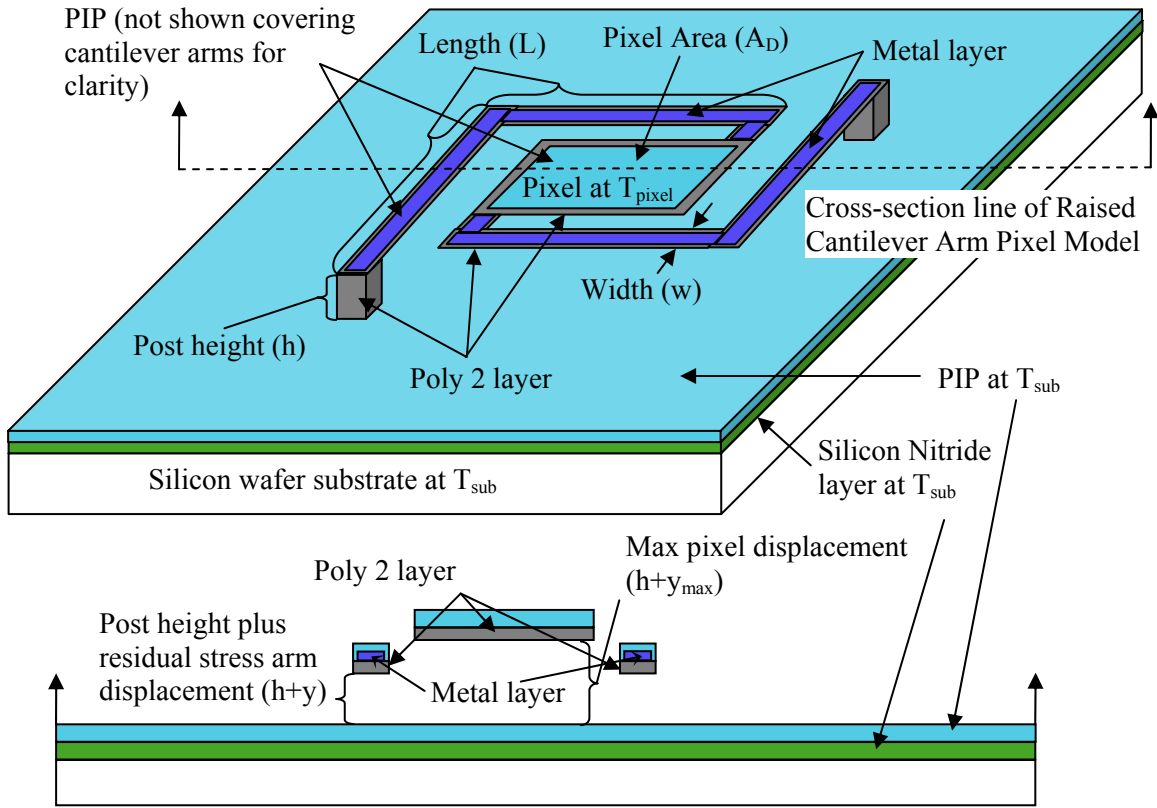
Figure 36. Picture describing general Raised Cantilever Arm Pixel System and cross-section showing pixel displacement and residual stress cantilever arm displacement.

number, Nusselt number, and the convective heat transfer coefficient. Using a one-degree temperature difference to find the figures of merit per-degree, the T_{pixel} is set at 31 °C and T_{sub} is set at 30 °C, to simulate common outside daytime temperature conditions. Table 3 summarizes the physical properties and values used to calculate the total heat capacitance, total effective thermal conductance, and thermal time constant. The calculated thermal time constant is below 1 msec, generating a quick thermal response, which allows the sensor readout circuit to sample at a high rate.

The calculations performed for the derivation of the thermal time constant establish the necessary calculations for the responsivity, using Equation (16). Based on

Table 3. Raised Cantilever Arm Pixel System material properties, dimensions, and calculated values used to determine pixel thermal time constant.

Material Properties[49,54-56]				
	k [W/m·K]	ρ [kg/m^3]	c [J/kg·K]	$g\beta/\alpha v$ [1/K·cm^3]
PIP	2	1260	1660	-
Metal	315.3	-	-	-
PolySilicon	34	2330	707.6	-
Air, dry at 30°C	0.026	-	-	90.7
Dimensions				
w [µm]		V [µm^3]		t [µm]
PIP	12	PIP	8437.5	PIP	1.5
Metal	10	PolySilicon	8445.94	Metal	0.5188
PolySilicon	12			PolySilicon	1.5015
				Air	3.6508
A_D [µm^2]	5625	L [µm]	100	
Perimeter [µm]	300	# arm sections	2	
Calculated Values				
		G [W/K]		C [J/K]
L_c [µm]	18.75	PIP	1.800E-07	PIP	1.765E-08
Rayleigh # [unitless]	5.979E-07	Metal	8.179E-06	PolySilicon	1.392E-08
Nusselt # [unitless]	0.01502	PolySilicon	3.063E-06	
$\bar{h}$ [W/m^2-K]	20.822	Air Conduction	4.006E-05	
τ_T [s]	6.119E-04	Air Convection	1.171E-07	

initial research performed by the AFRL and assuming the absorptance of carbon black to be approximately its emissivity, the responsivity is demonstrated for a specific set of modeling conditions in Table 4. Table 4 shows the material properties, electrical properties, and geometry of the pixel that affect the responsivity. To simplify the model, the angular modulation frequency is assumed to be set by a slowly-chopped blackbody radiation source at 1 Hz. The calculated responsivity is sensitive to small changes in irradiant power, which allows the sensor readout circuit voltage to operate within

Table 4. Raised Cantilever Arm Pixel System properties and test conditions modeled to calculate responsivity.

Properties and Calculations[43,57]					
α [%/K]	15	i_B [μA]	0.769	G_{total} [W/K]	5.160E-05
η [unitless]	0.88	R_B [MΩ]	6.5	τ_T [s]	6.119E-04
β [unitless]	0.378	ω [rad/s]	6.283	$\Re$ [V/W]	4833.97

nominally low millivolt ranges. The responsivity is comparable to other exploratory research responsivities [39].

Using the responsivity calculation and by theoretically limiting the bandwidth of the bias signal and the system bandwidth, the Johnson, temperature fluctuation, and background fluctuation noises can be calculated using Equations (17), (18), and (20). The system bandwidth and bias signal are controllable design parameters of the readout integrated circuit design and for modeling purposes are limited to 1 kHz to allow for the 33 ms refresh speed standard of common video screens plus faster read rates, if required in the future. For a given total system noise voltage and responsivity, the NEP can be calculated using Equation (21). The parameters for the Johnson, temperature fluctuation, and background fluctuation noises and the calculated NEP are shown in Table 5. The calculated NEP value is approximately 2 nW, which allows a readout circuit sensitive to millivolt changes to identify a microwatt power signal in an environment of comparable noise power.

By using values from Tables 4 and 5 and Equation (22), the detectivity is calculated to be 6.747×10^7 [cm·Hz$^{\frac{1}{2}}$/W]. The calculated detectivity indicates the normalized pixel design is also sensitive to microwatt signal powers, normalized for bandwidth and pixel area.

Table 5. Raised Cantilever Arm Pixel System noise properties and calculated Noise Equivalent Power.

Noise properties					
k_B [J/K]	1.38E-23	R_B [MΩ]	6.5	T_{pixel} [K]	304.15
σ [W/cm^2·K^4]	5.67E-12	A_D [μm^2]	5625	T_B [K]	303.15
η [unitless]	0.88	B [Hz]	1000	G_{total} [W/K]	5.160E-05
				$\Re$ [V/W]	4833.97
Calculations					
V^2_J [V^2]	1.091E-10	V^2_{TF} [V^2]	2.300E-17	V^2_{BF} [V^2]	3.738E-18
V_{total} [V]	1.045E-05	NEP [W]	2.161E-09		

The NETD is calculated using Equation (23). Table 6 tabulates the values used to calculate the NETD. The calculation assumes that the focal length of the optics is an f/1 ratio and the transmittance of the optics is the value used previously by the AFRL for the spectral range of 8 to 12 μm. The calculated NETD is below 4 K, allowing the sensor to distinguish objects with a temperature difference of 4 K or greater from each other.

In this section, the figures of merit of a Raised Cantilever Arm Pixel were calculated using the Residual Stress Cantilever Model, material properties, geometry of the test system setup, and previous data provided by the AFRL.

Table 6. Raised Cantilever Arm Pixel System optical properties used to calculate Noise Equivalent Temperature Difference.

Optical System Properties[29,43,58]				
f/# [unitless]	1	$\left(\dfrac{\Delta P}{\Delta T}\right)_{\lambda_1-\lambda_2}$ [W/cm^2·sr·K]		6.000E-05
τ_0 [unitless]	0.7			
Previously Calculated Results				
V_{total} [V]	1.045E-05	A_D [μm^2]	5625	
$\Re$ [V/W]	4833.97			
Calculations				
NETD [K]	3.659			

5.5 Suspended Membrane Pixel Figures of Merit

The calculation of the figures of merit for the Suspended Membrane Pixel assume that the PIP is applied in a thick planar layer either by spin coating or directly by pipette. The heat loss paths of the pixel are by conduction through the substrate, conduction through the PIP, and natural convection from the top surface. In addition to conduction paths, additional thermal resistance terms are added for the PIP, Oxide 1, Oxide 2, Silicon Nitride, and Silicon substrate layers that describe the thermal resistance to heat traveling between layers, and are detailed by Equation (5). Heat loss occurs primarily as heat spreads out and away from the pixel along horizontal paths. Figure 37 shows the general form of the Suspended Membrane Pixel System including design variables and a cross-section view of the pixel, PIP, PolyMUMPs films, and substrate.

As with the previous section, the total heat capacitance and total effective thermal conductance are sums of the individual components. In the case of the thermal conductances for the PIP, Oxide 1, Oxide 2, Silicon Nitride and Silicon substrate, there are additional inverse thermal resistance terms, described by Equations (4) and (5), added directly to each individual thermal conductance term. Table 7 shows the material properties and dimensions used to calculate the thermal time constant for the Suspended Membrane Pixel System with a T_{pixel} of 31 °C and a T_{sub} of 30 °C. The calculated thermal time constant is below 10 μsec, generating a very quick thermal response, which allows the sensor readout circuit to sample at a rate that is thousands of times the nominal video sampling rate of 30 samples per second. The presence of the silicon substrate is non-optimal, but was modeled to reflect the Suspended Membrane

70
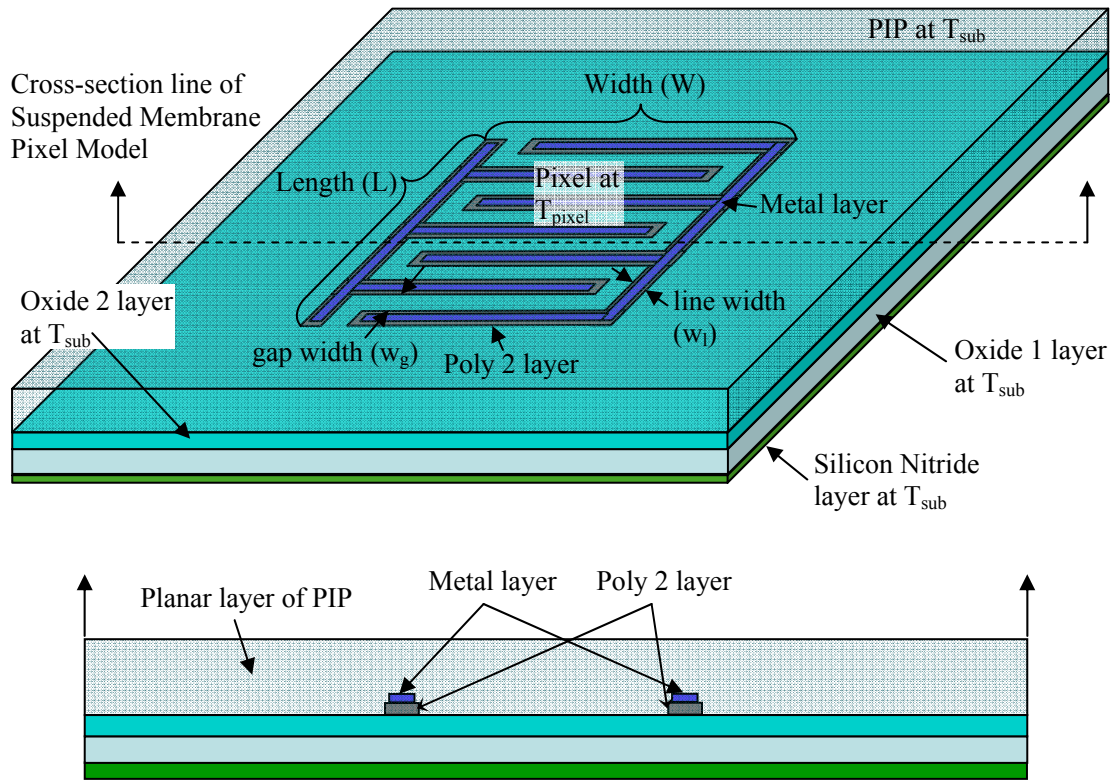
Figure 37. Picture describing general Suspended Membrane Pixel System and cross-section showing pixel layers.

Pixel Sensor used in the simplified test setup in Chapter 6, Experiments and Results. The relatively thick silicon substrate will act as a large thermal conductance, causing a non-optimal trade-off between heat capacitance and thermal conductance. This non-optimal trade-off is reflected in the modeled values which yield a short thermal time constant, small responsivity and detectivity, and large NEP and NETD values.

The same assumptions used by the Raised Cantilever Arm Pixel System for the responsivity calculations are also used for the Suspended Membrane Pixel System test setup and assumptions. Table 8 shows the properties and calculations for the responsivity of the Suspended Membrane Pixel System. The calculated responsivity is not sensitive to

Table 7. Suspended Membrane Pixel System material properties, dimensions, and calculated values used to calculate the thermal time constant.

Material Properties[49,54-56]				
	k [W/m·K]	ρ [kg/m^3]	c [J/kg·K]	gβ/αv [1/K·cm^3]
PIP	2	1260	1660	-
Metal	315.3	19300	129.3	-
PolySilicon	34	2330	707.6	-
Silicon Dioxide	1.38	2203	743.2	-
Silicon Nitride	30.1	3100	710.6	-
Silicon, crystalline	157	2330	702.24	-
Air, dry at 30°C	0.026	-	-	90.7

Dimensions					
w [µm]		V [µm^3]		t [µm]	
Metal	8	PIP	4.560E+05	PIP	12
PolySilicon	10	Metal	6.491E+03	Metal	0.5188
"finger" gap	20	PolySilicon	2.327E+04	PolySilicon	1.5015
		Oxide 1	7.772E+04	Oxide 1	2.0452
		Oxide 2	2.881E+04	Oxide 2	0.7581
L [µm]	190	Silicon Nitride	2.345E+04	Silicon Nitride	0.6171
W [µm]	200	Silicon	1.444E+06	Silicon	38

Calculated Values					
	G [W/K]	R_{Ts} [K/W]	C [J/K]		
PIP	1.680E-03	1571.429	9.538E-07	L_c [µm]	48.718
Metal	1.472E-02	-	1.620E-08	Rayleigh # [unitless]	1.049E-05
PolySilicon	3.676E-03	-	3.837E-08	Nusselt # [unitless]	0.03073
Oxide 1	1.976E-04	2277.433	1.272E-07	$\bar{h}$ [W/m^2·K]	16.400
Oxide 2	7.323E-05	2277.433	4.717E-08	τ_T [s]	8.186E-06
Silicon Nitride	1.300E-03	104.414	5.166E-08		
Silicon	4.176E-01	20.018	2.363E-06		
Air Convection	6.232E-07	-	-		

small changes in irradiant power, which inhibits the sensor readout circuit voltage from

operating within nominally low voltage ranges for small input powers. Using the

calculated responsivity, a functioning sensor would require a large change in input power

Table 8. Suspended Membrane Pixel System properties and test conditions modeled to calculate responsivity.

Properties and Calculations[43,57]					
α [%/K]	15	i_B [μA]	0.008	G_{total} [W/K]	4.394E-01
η [unitless]	0.88	R_B [MΩ]	620	τ_T [s]	8.186E-06
β [unitless]	0.805	ω [rad/s]	6.283	$\Re$ [V/W]	1.21

or an impractically-sensitive state-of-the-art readout circuit that is highly sensitive to microvolt changes.

The assumptions used in the previous section for the calculation of the noise equivalent power are duplicated for the modeling purposes of the Suspended Membrane Pixel System. Table 9 outlines the electrical and system noise properties used to calculate the NEP. The calculated NEP value is approximately 8 μW, which is a large noise power that covers microvolt signals generated by low power IR signals and may not be recoverable without state-of-the-art signal processing and readout circuitry.

By using values from Tables 8 and 9 and Equation (22), the detectivity is calculated to be 6.558×10^3 [cm·Hz$^{\frac{1}{2}}$/W]. The calculated detectivity indicates the normalized pixel design is insensitive to microwatt signal powers and would not be able

Table 9. Suspended Membrane Pixel System noise properties and calculated Noise Equivalent Power.

Noise properties					
k_B [J/K]	1.38E-23	R_B [MΩ]	620	T_{pixel} [K]	304.15
σ [W/cm^2·K^4]	5.67E-12	A_D [μm^2]	38000	T_B [K]	303.15
η [unitless]	0.88	B [Hz]	1000	G_{total} [W/K]	4.394E-01
				$\Re$ [V/W]	1.21
Calculations					
V^2_J [V^2]	1.041E-08	V^2_{TF} [V^2]	1.226E-20	V^2_{BF} [V^2]	1.581E-24
V_{total} [V]	1.020E-04	NEP [W]	8.436E-05		

to detect normal targets of military importance, such as vehicles or people against a

daytime background.

As with the previous section, the same assumptions for the optical test setup are

made for the Suspended Membrane Pixel System. Table 10 shows the optical properties

and calculated NETD for the Suspended Membrane Pixel System. The calculated NETD

is above 21000 K, making the sensor unable to distinguish between objects and their

background. IR imaging arrays fabricated with these pixels would display a constant

output independent of the source temperature or source temperature change relative to its

background. The modeled Suspended Membrane Pixel includes a silicon substrate. The

original Suspended Membrane Pixel Design did not include the silicon substrate in order

to balance the pixel heat capacity and pixel effective thermal conductance. The effect of

including the silicon substrate increases the effective thermal conductance, because the

silicon substrate acts as a large heat sink, causing a small thermal time constant, small

responsivity, small detectivity, large NEP, and large NETD.

Table 10. Suspended Membrane Pixel System optical properties used to calculate Noise Equivalent Temperature Difference.

Optical System Properties[29,43,58]					
f/# [unitless]	1	$\left(\dfrac{\Delta P}{\Delta T}\right)_{\lambda_1-\lambda_2}$		[W/cm^2·sr·K]	6.000E-05
τ_0 [unitless]	0.7				
Previously Calculated Results					
V_{total} [V]	1.020E-04	A_D [μm^2]	38000		
$\Re$ [V/W]	1.21				
Calculations					
NETD [K]	21141.882				

In this section, the figures of merit of a Suspended Membrane Pixel were calculated using material properties, geometry of the test system setup, and previous data provided by the AFRL.

5.6 Summary

The calculations were performed to derive the figures of merit for both the Raised Cantilever Arm Pixel and the Suspended Membrane Pixel. The basic heat transfer model was used to derive and calculate the total effective thermal conductance and total heat capacitance for the pixel system. Following the heat transfer calculations and using the Residual Stress Cantilever Model for the Raised Cantilever Arm Pixel Model, the thermal time constants for each system were calculated. After calculating the thermal time constants, total effective thermal conductance and total heat capacitance, the calculations for responsivity, NEP, detectivity, and NETD followed quickly with some basic assumptions of material, electrical, noise, and optical properties. The modeled figures of merit are qualitative measures of the sensor capability and will be compared to experimentally derived values.

VI. Experiments and Results

6.1 Chapter Overview

This chapter describes the experiments performed to verify material properties and to post-process and test the Raised Cantilever Arm Pixel Sensor and the Suspended Membrane Pixel Sensor. An experiment discussed in Section 6.2 was performed to understand the PIP spin thickness characteristics for modeling of the Raised Cantilever Arm Pixel Sensor. As mentioned in the Design and Fabrication chapter, a wet chemical etch was attempted to remove the bulk crystal silicon substrate and the results are discussed in Section 6.3. The initial test environment is detailed in Section 6.4 and the tests performed and the results are discussed in Section 6.5

6.2 PIP Spin Testing

In order to characterize some basic properties of the PIP material, a simple spin test was conducted to evaluate the thickness of a film coating that was spun on using the Solitec Photoresist Spinner. The polymer material provided by the AFRL was the same as the PIP material [43], except without the protein and the carbon black. The polymer conglomerate is normally used as a suspension for the protein and carbon black, which are considered the active electrical and IR absorbing materials. Two varieties of material were provided with different viscosities. The first had a "thick" viscosity which contained less water and more polymer material. The second had a "thin" viscosity which contained more water and less polymer material. For spin characteristics, these modified materials provided an upper and lower boundary for the normal PIP material. The two polymer materials were applied by pipette and spun for 30 seconds at various

rpm onto sections of scrap wafer with pieces of common clear tape over the wafer. The

polymer materials were allowed to dry overnight in a dry nitrogen box. Then, the pieces

of tape were removed leaving only strips of the polymer material on the surface of the

scrap wafer. Figure 38 shows a diagram of (a) the wafer setup with clear tape and (b) the

wafer with dried polymer material. Multiple measurements of material thicknesses were

made using a Tencor Profilometer on several edges of dried polymer material. The

measurements were made on several different pieces of scrap wafer for both types of

material and each measurement set per piece was averaged for the applied spin speed.

Figure 39 shows the results of the average measurements as a function of applied spin

speed for both types of polymer material. As shown in Figure 39, the materials behave

very similarly, and for averaging purposes, the general material thickness as a function of

spin speed can be considered the average of both data values.

(a)   (b)
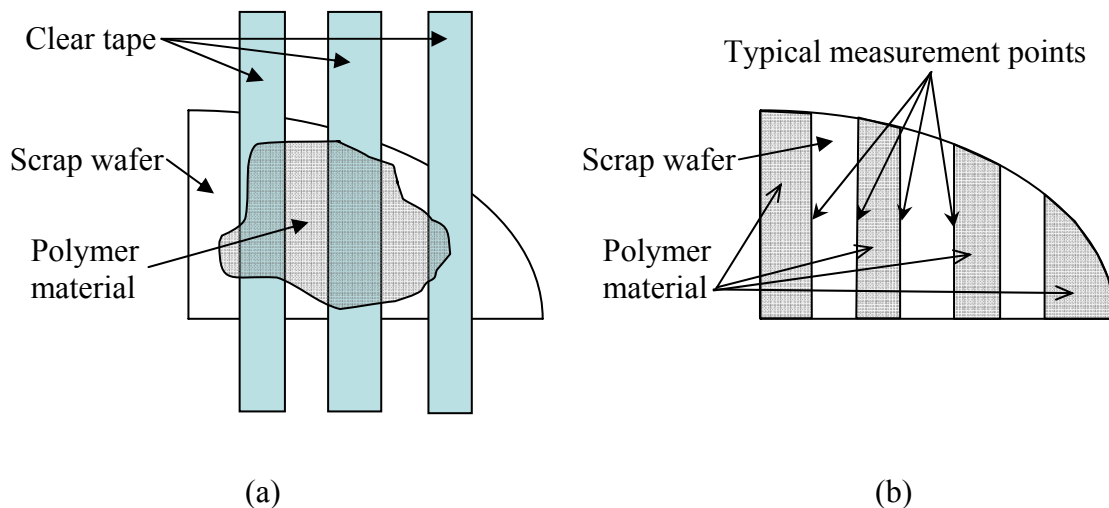
Figure 38. Diagram of (a) spin test setup using scrap wafer and clear tape and (b) wafer
with dried polymer material used to measured thickness using a Tencor Profilometer.
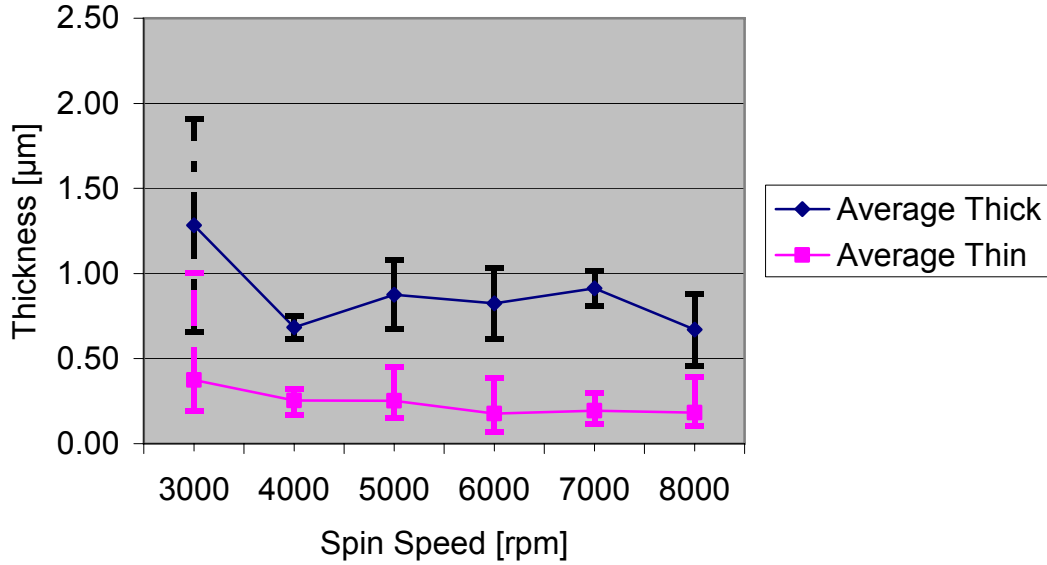
Figure 39. Average thickness of two different polymer materials and overall thickness average as a function of applied spin speed.

For a simple understanding of spin properties of the polymer material, it was then spun onto a simple four-legged raised platform structure similar to the Raised Cantilever Arm Pixel design. The "thick" version of the polymer material was spun on at 3000 rpm for 30 seconds. Figure 40 shows an SEM image of the PolyMUMPs structures before the polymer material is applied and an SEM image with a cross-section close-up of the polymer material stripped away using a razor blade. The material behaved partially as expected, with the polymer material coating the PolyMUMPs structures in a conformal manner, but also going under structures and not leaving a complete air gap between the structure and the substrate. The PIP material presence under the pixel is accounted for by assuming the conduction through air ends at the PIP material, which is at the substrate temperature, T_{sub}.
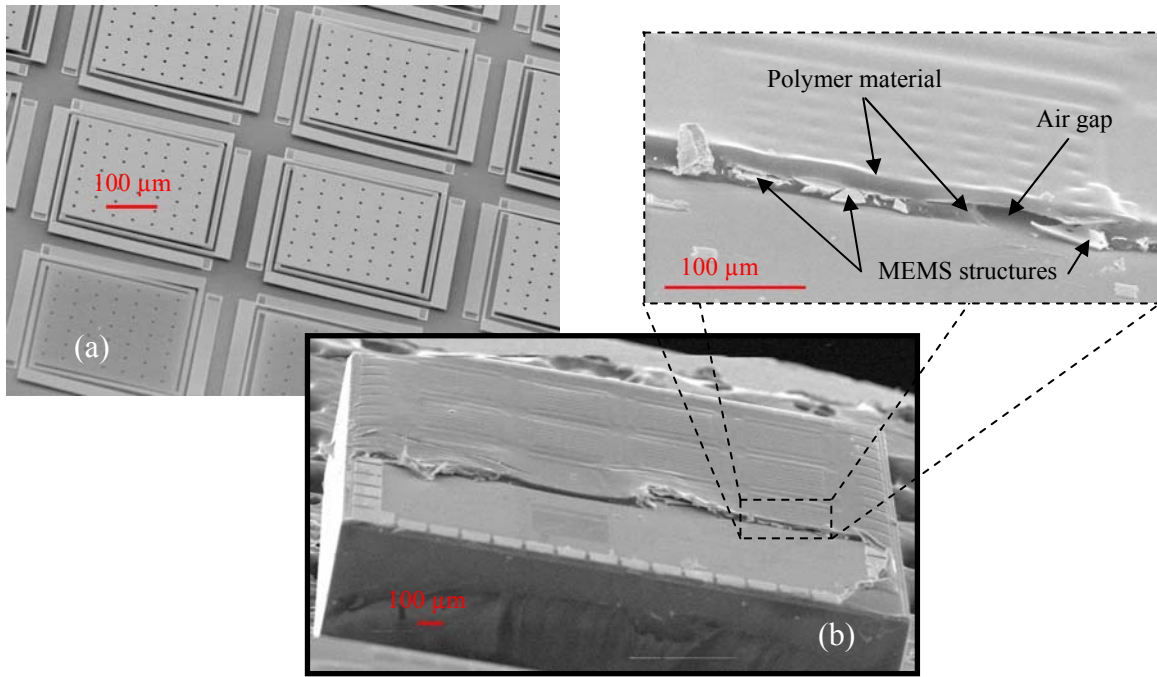
Figure 40. SEM images (a) without polymer material and (b) with polymer material spun onto PolyMUMPs raised platforms at 3000 rpm for 30 seconds.

Qualitative spin testing of the PIP material on Raised Cantilever Arm Pixels yielded varying results with properties different than indicated by initial testing. Figure 41 shows a typical sample of a Raised Cantilever Arm Pixel Sensor that has been coated with PIP. Figure 41 part (a) shows a pixel before spin coating with PIP material, whereas Figure 41 part (b) shows a close-up view of three different pixels and a profile line that will be examined in closer detail using a Zygo NewView 5000 White Light Interferometer in Figures 42, 43, and 44.

Figure 42 shows a topological color map of relative measured height. The measured area is the same area as shown in Figure 41 part (b). The center pixel is shown to be about 4.5 μm higher above the substrate than the other two sample pixels. The uniform color of the other pixel arms indicates that the residual stress of the cantilever
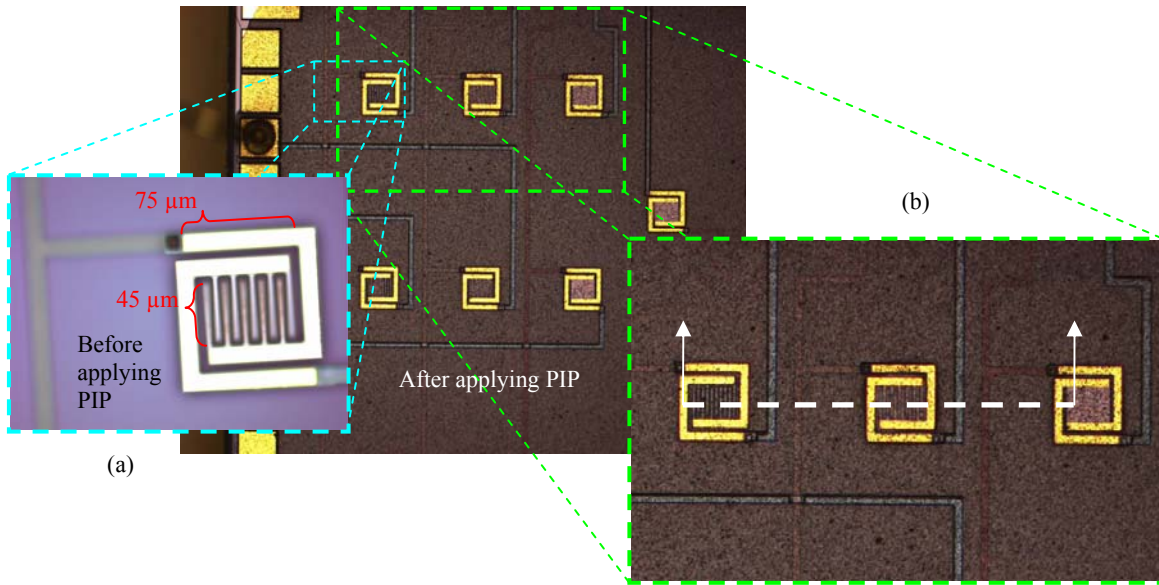
Figure 41. Pictures of Raised Cantilever Arm Pixel Sensor (a) without PIP material and (b) with PIP material applied by spin coating at 5000 rpm for 30 seconds.

arms has been overcome, possibly by stiction from the PIP material application. The

pixels stuck to the substrate are no longer thermally isolated from the substrate and will
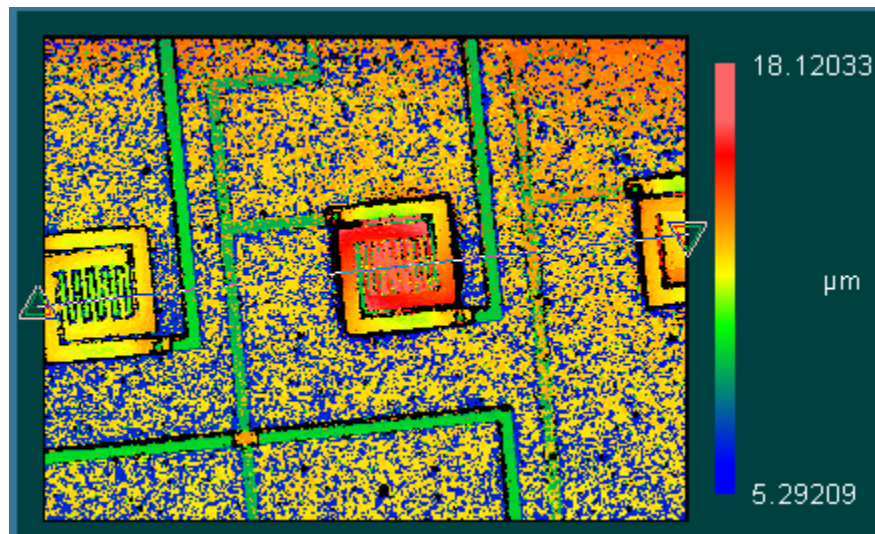
Figure 42. Topological color map of relative measured height of a Raised Cantilever Arm Pixel Sensor with PIP.

have different characteristics and figures of merit than those modeled in chapter 5.

Figure 43 shows an oblique color map plot of relative measured height for Figure 41 part (b). Figure 43 clearly shows the center pixel cantilever arms are bending in the same manner as a residual stress cantilever arm, while the pixel to the left clearly shows the identical residual stress cantilever arms are no longer bending. The application process of the PIP material overcame the residual stress cantilever arms designed to hold the pixel above the substrate to thermally isolate the pixels.

Figure 44 shows a relative measured height profile along the center of the three pixels shown in Figure 41 part (b) and Figure 42. The top dashed line indicates the maximum height of the pixel with PIP material. The bottom dashed line corresponds to the height of the Poly 2 address line. The PIP material appears conformal but thicker
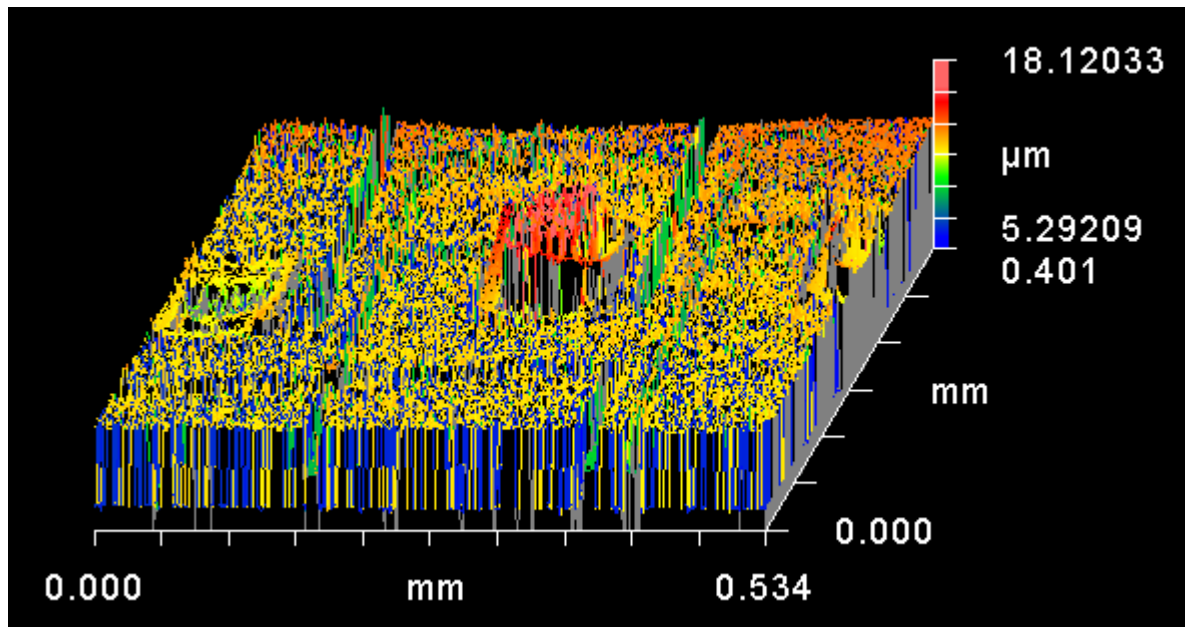
Figure 43. Oblique plot of relative measured height of a Raised Cantilever Arm Pixel Sensor with PIP.

than expected. The height from the Poly 2 address line to the top of the PIP material is about 3 μm, which is over twice the thickness of the polymer spin data indicated in Figure 39. The different spin characteristics of the PIP material may be from the smaller surface area of the PolyMUMPs test dice, the non-planar surface of the pixel arrays, and/or the inclusion of the protein and carbon black in the polymer suspension.

The PIP material spin coating process also created other problems and anomalies that would affect modeling accuracy. Figure 45 shows common problems caused by the PIP spin coating process. The PIP did not always uniformly coat the pixel surfaces, causing varying thicknesses and uncoated portions of the sensor. Also, air bubbles would randomly be caught on different surface features of the sensor. These anomalies may be attributed to not completely covering all pixels on the PolyMUMPs test dice with PIP material before spinning and/or aerating the PIP material when applying by pipette.
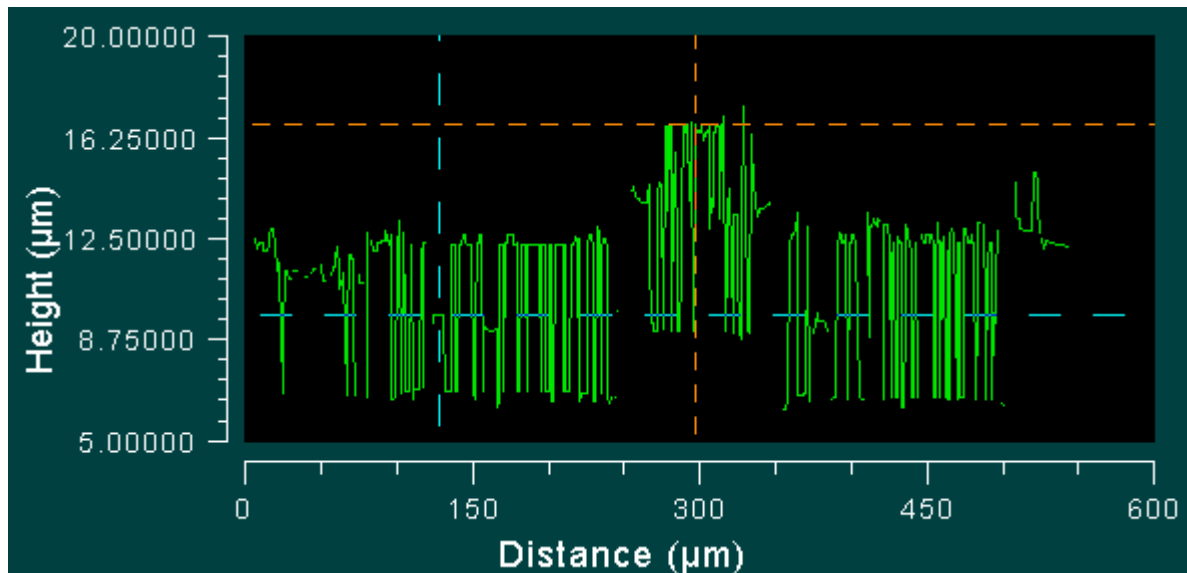
Figure 44. Profile plot of relative measured height of a Raised Cantilever Arm Pixel Sensor with PIP.
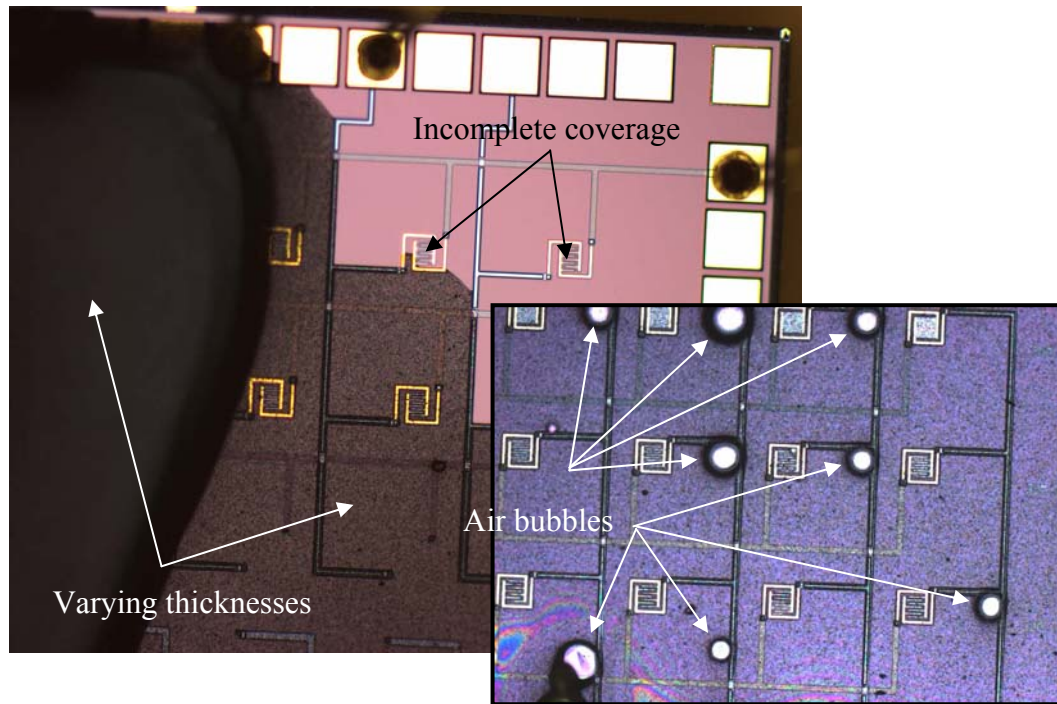
Figure 45. Common problems and anomalies caused by PIP spin coating process.

This section outlined the spin coating testing procedures performed to gain more insight into the nature of the polymer and PIP materials for use in spin coating the Raised Cantilever Arm Pixel Sensor. The results indicate that the spin coat process is affected by many extraneous attributes, such as surface area, surface coverage, pipette application procedure, and PolyMUMPs test die topography, which caused difficulties in refining and duplicating the spin coating process on the Raised Cantilever Arm Pixel Sensor.

6.3 Etch Testing

The design of the Suspended Membrane Pixel Sensor requires the removal of the bulk crystalline silicon substrate to minimize heat transfer through the substrate, as shown in Figure 22. As mentioned in Section 3.3, the initial attempts were made by

securing the test dice in a protective holder and placing it in a wet chemical etchant bath. The attempts at wet chemical etching typically failed by either releasing the test dice into the etchant solution, thereby dissolving most, if not all, polysilicon structures, or by slow leakage of the etchant solution to the front pixel face, also dissolving the polysilicon pixel structures and eroding the bond pads.

Initial wet etch tests used the strongest available pre-mixed solution of 50% KOH W/V in a solution of water at room temperature or warmed to either 50 °C or 60 °C. Initial tests yielded deformed etch surfaces that were not uniform and anisotropic, as expected with KOH on crystalline silicon. Following initial tests, a different solution of 12.5% KOH W/V at 80 °C, similar to the recipe suggested by MEMSCAP [46], was tested. Figure 46 shows an initial etch test using 50% KOH W/V at room temperature (21 °C) for 1 hour. For the etch solution conditions, an etch depth of approximately 50 to 60 µm and anisotropic (111) plane sidewall formation was expected. The test die was protected by Crystal Bond and was initially scored by a 0.001"-diameter tungsten carbide drill bit to penetrate the backside PolyMUMPs layers and expose the underlying silicon substrate for etching. The top remaining layer is either PSG or silicon nitride. There was no significantly noticeable etching; however, the test die showed signs of significant surface roughness.

Figure 47 shows a test die with significant surface roughness after exposure to the etch solution whose backside layers were scored using a diamond tipped scribe pen. The diamond-scribed test die was etched in the same etchant bath as the test die from Figure 46. The unexpected rough surface results of initial testing were cause to explore other
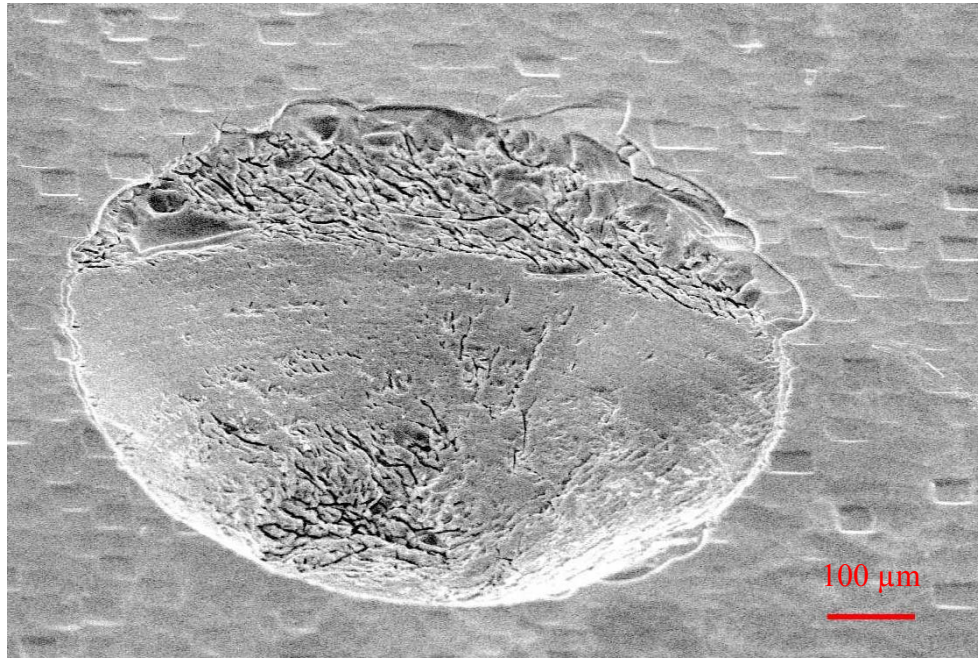
Figure 46. SEM image of test die with drill bit score of backside PolyMUMPs layers after 1 hour exposure to 50% KOH W/V at 21 °C.

wet etch recipes, exposure times, and temperature conditions. The rough surface etch results of the silicon may be caused by an over-aggressive etch solution.

Following the initial tests, a simple test was performed to observe long term exposure of the test dice to the wet chemical etchant and confirm anisotropic etch behavior of KOH on crystalline silicon for the PolyMUMPs test dice. Several test dice were placed directly in a solution of 50% KOH W/V at a bath temperature of 50 °C with a Teflon-coated solution agitator and the spinner set for 1000 rpm and left overnight to etch. Figure 48 shows the face of one test die after long term exposure for 14 hours to the wet chemical etchant solution. Significant destruction of bond pads, polysilicon structures, under etched gold structures, and anisotropic etching of the test die side walls is evident.
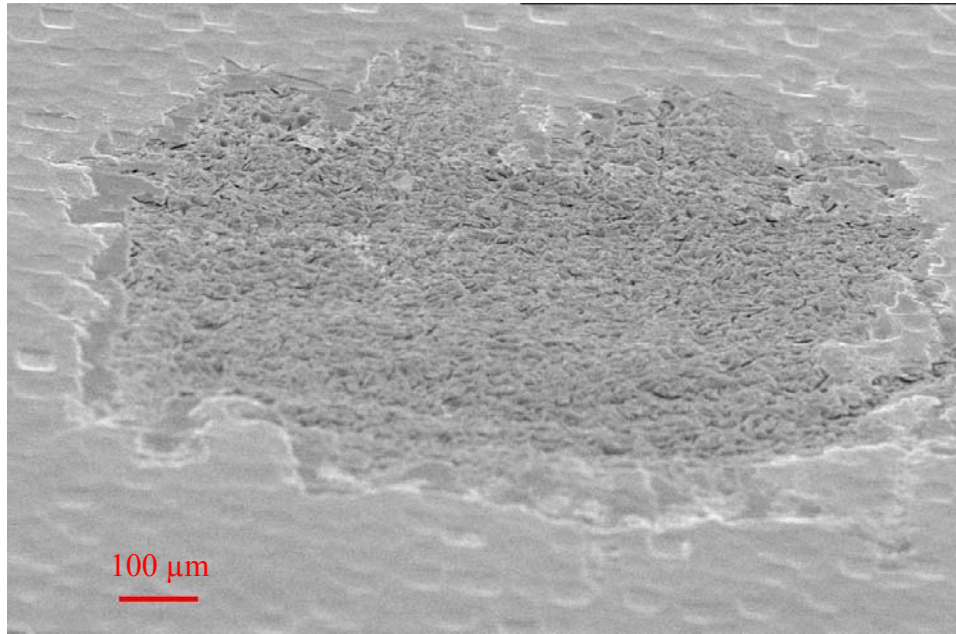
Figure 47. SEM image of test die with diamond tipped scribe pen scoring of backside PolyMUMPs layers after 1 hour exposure to 50% KOH W/V at 21 °C.
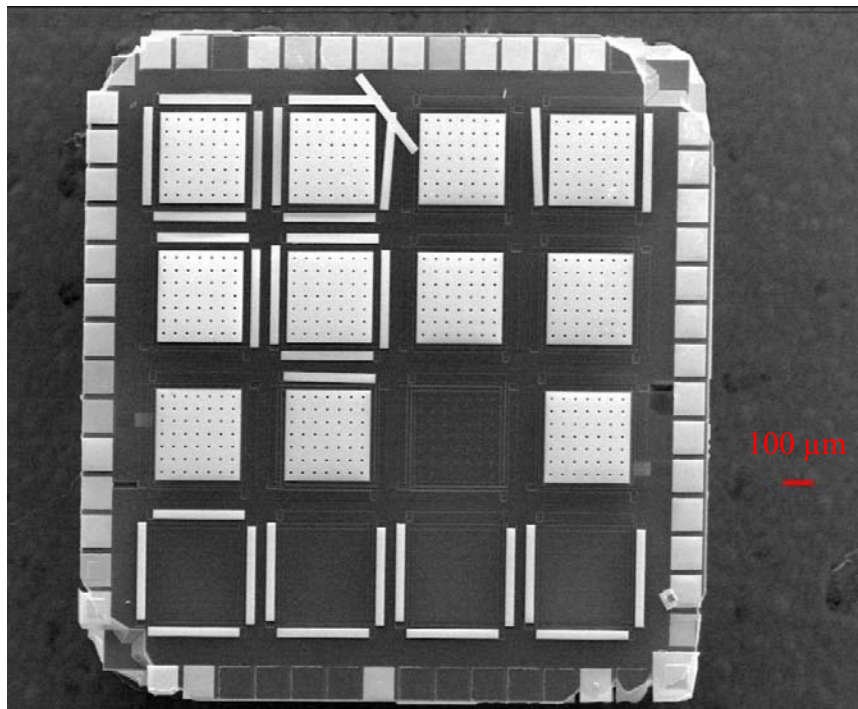

Figure 48. SEM picture of test die exposed directly to 50% KOH W/V at 50 °C with agitation for 14 hours.

Looking at the exposed corners of the test die revealed a significant anisotropic etch behavior that was analyzed to calculate the etch rate of the solution. Figure 49 shows a top view with an isometric close-up of the bottom left corner of Figure 48. The horizontal etch distance was estimated to be 45 μm from the top layer. A vertical etch distance of 64 μm was calculated from the horizontal estimate. The etch rate for the conditions outlined for Figure 48 is 0.076 μm/minute. This etch rate is significantly lower than expected and is not within the range of rates quoted by other sources [45,46]. The etch rates may be slower due to the bubble formation or due to the temperature difference between the DIW bath and the actual etch solution. Looking further at the test die from Figure 48, a backside view of the test die in Figure 50 shows two tungsten carbide drill holes that penetrated the backside layers that were etched. Anisotropic etch behavior is visible on the sidewalls and square geometry of the etch holes, which is characteristic of KOH etching. A horizontal etch distance of 120 μm is estimated from Figure 50, implying a vertical etch distance of 170 μm. For 14 hours, the etch rate is calculated to be 0.202 μm/minute, which is also lower than quoted.

Based on the etch rate of 0.202 μm/minute, a long term etch test was performed to confirm the etch rate. At an etch rate of 0.202 μm/minute, a 24 hour etch time would yield an approximate etch depth of 291 μm, which would be very visible and measurable for a substrate depth of 500 μm. Eleven chips were placed in a solution of 50% KOH W/V at a temperature of 60 °C with agitation at 500 rpm for 25 hours. Two chips were placed in the etchant solution unprotected, while the other nine were encased by Crystal Bond on glass slides. The nine samples protected by the Crystal Bond were scored using
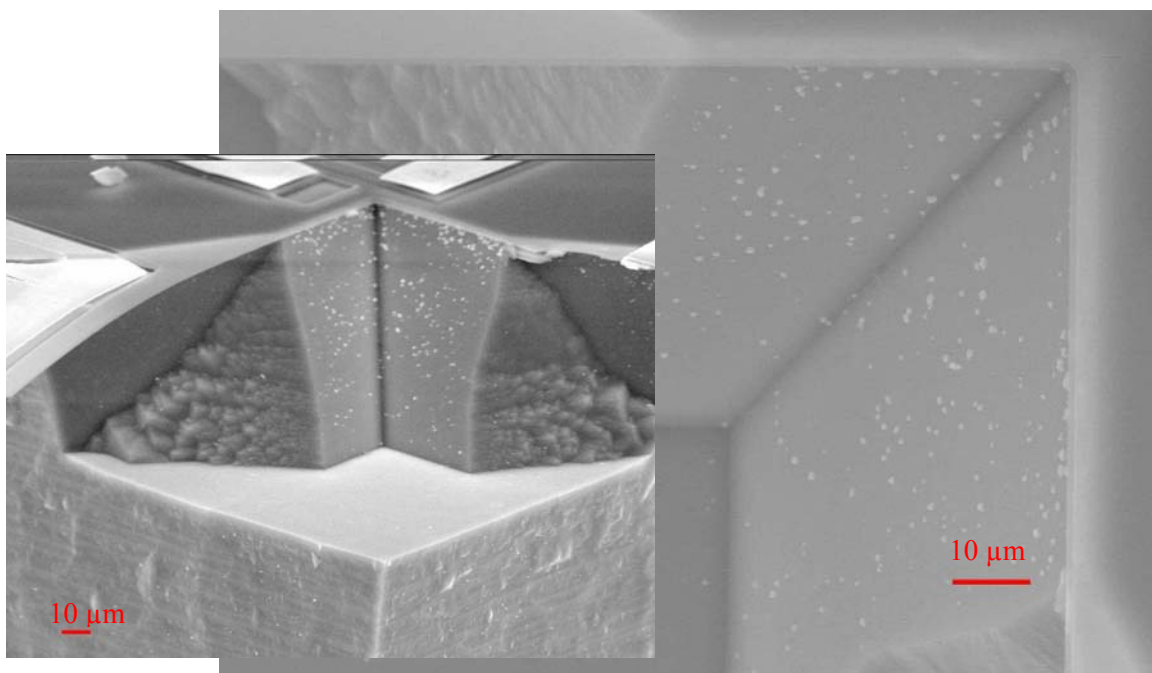
Figure 49. Front isometric close up and top view of a test die exposed directly to 50% KOH W/V at 50 °C with agitation for 14 hours.
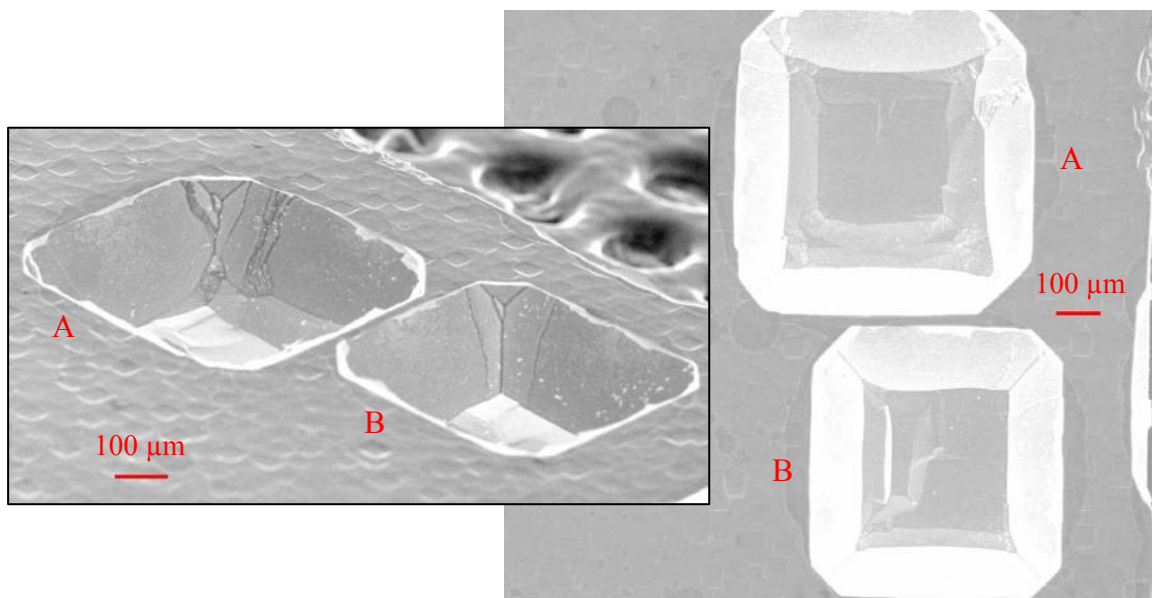
Figure 50. Rear isometric and back views of a test die exposed directly to 50% KOH W/V at 50 °C with agitation for 14 hours.

a diamond tipped scribe pen to penetrate the initial layers on the backside of the test dice. The diamond tipped scribe pen is an alternative method of removing the backside layers instead of using standard photolithography isotropic acid etches. The use of standard photolithography acid etches would add an additional wet etch step and further adds to the risk of damaging the pixels, and for these reasons was not used. At the end of 25 hours, the two unprotected test dice were not present and all 9 test dice encased by Crystal Bond had been released into the etchant solution at an unknown time, making the etch rate date invalid for comparison purposes. Figure 51 shows the typical remnants of a test die after exposure to 50% KOH W/V at 60 °C with 500 rpm agitation for 25 hours. The remaining exposed front structure etched approximately 160 μm vertically. Using the empirically determined etch rate of 0.202 μm/minute, it would have taken 13.2 hours to etch to that depth. Since the exposure was for 25 hours, the minimum etch rate would be 0.107 μm/minute. This etch rate is lower than the previously empirically determined rate; however, the unknown front exposure time by release into the etch solution for each test die does not allow this to be a definitive etch rate for this solution and etch conditions.

Following these tests, MEMSCAP was consulted directly and the solution of 15% KOH W/V at a temperature of 80 °C was quoted to etch at a rate of approximately 1.3 μm/minute for wafer-level etching [46]. The MEMSCAP representative stated that the company has only performed wafer-level etching and was not aware of any attempts to etch on the test die level.

Further etch testing occurred using materials such as photoresist and electrical
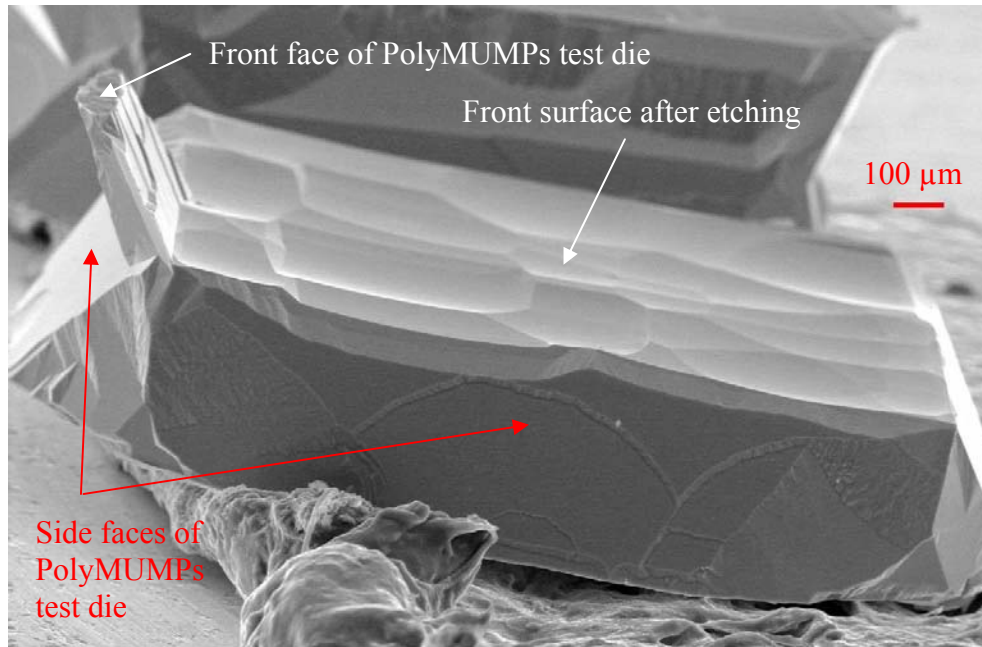
Figure 51. SEM picture of test die remains after exposure to 50% KOH W/V at 60 °C with 500 rpm agitation for 25 hours.

tape to provide the barrier to protect the pixel face from erosion by the etchant bath. Figure 52 shows the face of a test die secured by photoresist to a glass slide. The test die was exposed to an etchant bath of 12.5% KOH W/V at 80 °C for 3 hours. The etchant attacked the polysilicon electrical connection lines and the raised-temperature bath eroded the photoresist, allowing the etchant to leak onto the front pixel face.

The last phase of wet chemical etch attempts were made after the Suspended Membrane Pixel Sensor was etched using the UV laser ablation system, as discussed in section 3.3. The laser ablation technique heats, melts, and vaporizes the silicon in a repeating pattern that can selectively attack certain points of the substrate more than others. The initial examination of the laser ablation capabilities showed that it easily and quickly removed the back PolyMUMPs layers and the substrate. However, as mentioned
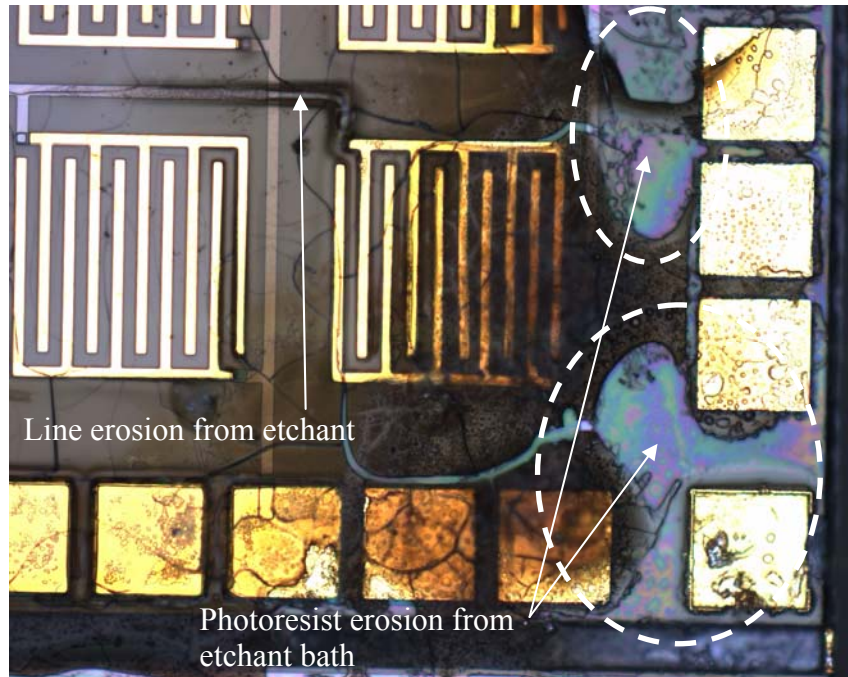
Figure 52. Suspended Membrane Pixel Sensor secured to glass slide using photoresist and exposed to etchant bath of 12.5% KOH W/V at 80 °C for 3 hours.

in section 3.3, the silicon substrate could not be completely etched away by laser-machining without damaging the front face. Wet chemical etching after laser-machining was attempted to remove the remaining silicon substrate. Figure 53 shows a view of the backside of a laser etched test die secured to a glass slide by electrical tape and an exploded view focusing on the bottom of that test die after wet chemical etching. The test die was exposed for 45 minutes to 12.5% KOH W/V at 85 °C. The rear substrate exposed to the wet chemical etchant has a rough surface texture and did not change significantly from before wet chemical etching.

However, Figure 54 is a picture of the front-side of the chip revealing laser ablation points that undetectably scored through the protective PolyMUMPs layers and
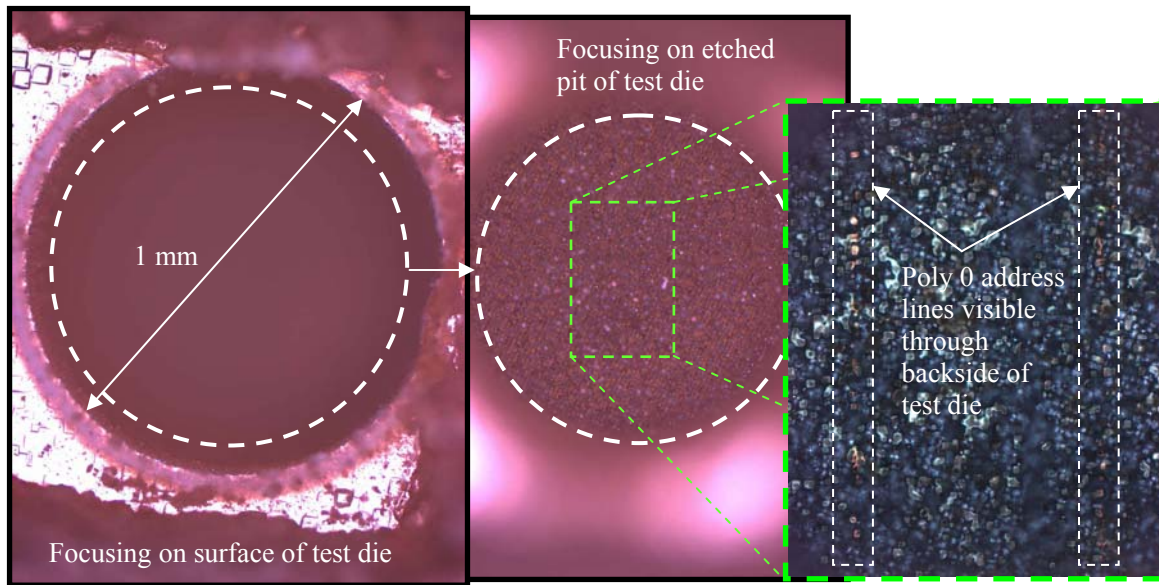
Figure 53. Suspended Membrane Pixel System with 1mm diameter laser etch and close-up view of substrate after wet chemical etch for 45 minutes in 12.5% KOH W/V at 85 °C.

allowed the wet chemical etchant to attack the front-side of the pixel system. If the wet chemical etch conditions are within a similar etch rate range of the proposed MEMSCAP etch rate, then the remaining crystalline silicon substrate should be removed after a short exposure to the etchant bath. The previous research of MLPC Inc. [59] would suggest that the silicon substrate remaining after laser-machining is a blend of crystalline silicon, polysilicon, and amorphous silicon due to the heat effects of the laser. This could lengthen the etch rate or cause the KOH etch solution to be ineffective. The remaining silicon substrate did not appear to be significantly attacked by the etch solution.

This section outlined the methods and recipes used to remove the backside PolyMUMPs layers in order to etch the bulk crystalline silicon wafer substrate. The primary methods used were wet chemical etching using a KOH solution in a raised temperature bath and laser-micromachining. The wet etch techniques coupled with
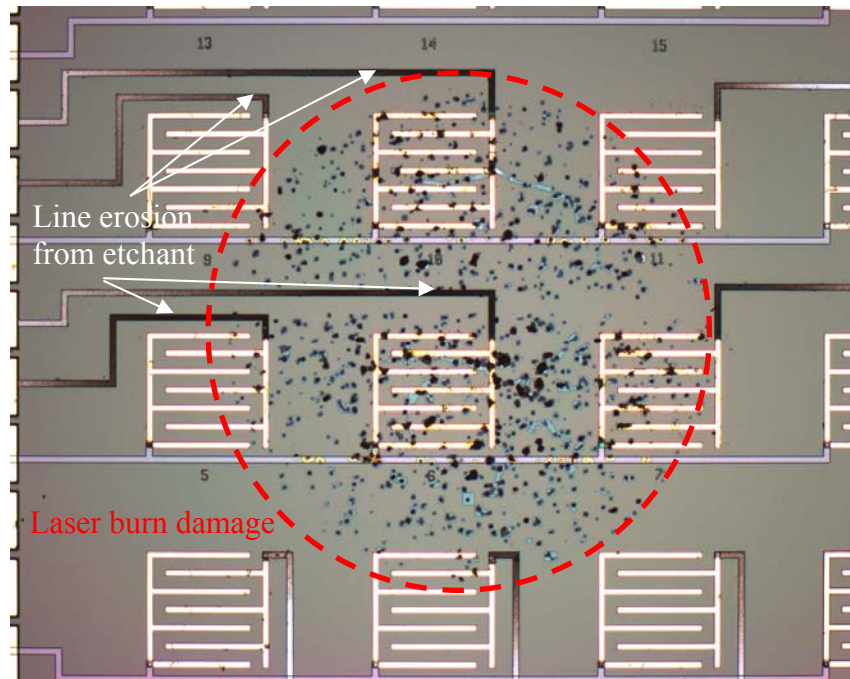
Figure 54. Front view of Suspended Membrane Pixel System with 1 mm diameter laser etch after wet chemical etch for 45 minutes in 12.5% KOH W/V at 85 °C.

extended bath times resulted in undesired etching of polysilicon structures. Laser-micromachining successfully removed most of the silicon substrate, but could not remove approximately 30 μm of substrate without undetectably damaging the front pixel face. Combined wet etch and laser micromachining efforts revealed the damage caused by laser-micromachining and etched polysilicon structures, destroying pixels in the process.

6.4 Initial Test Setup

Assuming a working pixel sensor is fabricated, an experimental test setup for determining the figures of merit is required. The experimental setup requires a known power source to excite a thermal response from the sensor, a method of electrically biasing the sensor, and a method of reading the electrical response of the sensor. Figure
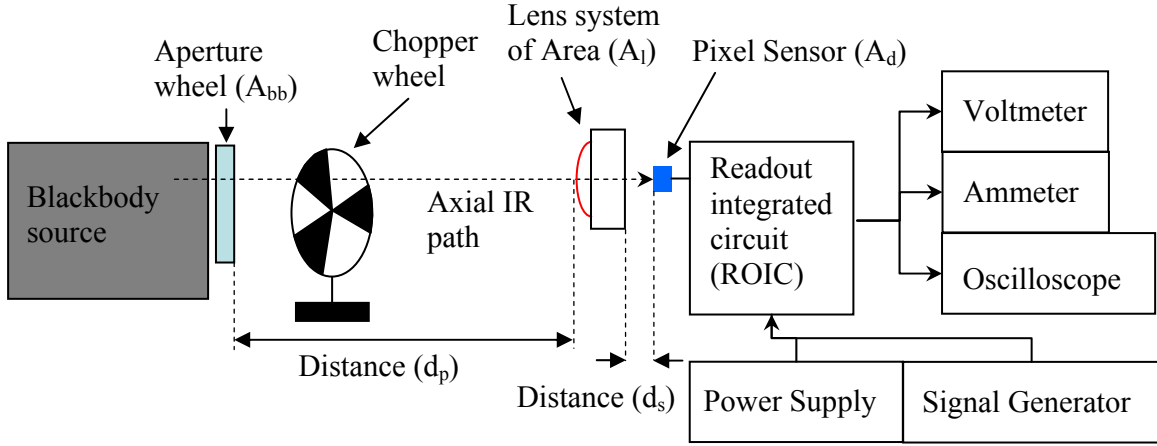
Figure 55. Diagram of the initial test setup for deriving figures of merit from fabricated pixel sensors.

55 shows a diagram of the basic components of the initial test setup.

The blackbody source is a controllable source of thermal power that can be effectively modeled as a Lambertian source for small angle differences from the axial IR path. Maximizing the irradiant power falling on the lens system requires that the angle differences of the projection vectors of the blackbody source and the lens system from the axial path be as small as possible to minimize $(\cos)^4$ losses [8]. The blackbody source has a spectral radiance derived from Planck's radiation law, defined by:

$$L_{e,\lambda}\left(\lambda,T\right) = \frac{2hc^2}{\lambda^5\left[e^{hc/\lambda k_B T} - 1\right]} \tag{30}$$

where h is Planck's constant, c is the speed of light in a vacuum, λ is wavelength, k_B is Boltzmann's constant, and T is the temperature of the source [8]. Figure 56 shows the theoretical spectral radiance curves for several temperatures within the range of the blackbody radiation source.

94
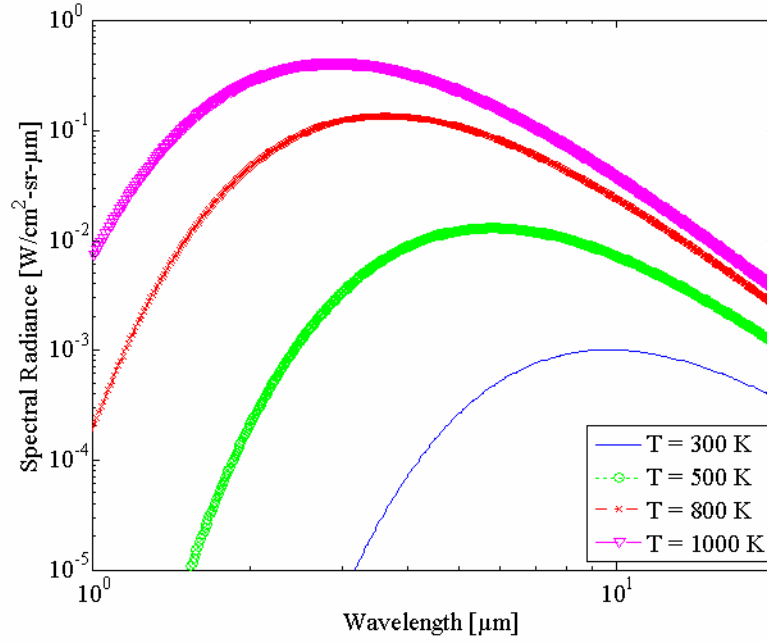
Figure 56. Spectral radiance curves of a blackbody source for 300 K, 500 K, 800 K, and 1000 K.

The flux incident on the lens system is derived from the spectral radiance equation and is expressed by:

$$\phi_d(\lambda, T) = L_{e,\lambda}(\lambda, T) A_s \Omega_o \qquad (31)$$

where A_s is the surface area of the source and Ω_o is the solid angle of the lens [8]. The flux equation is wavelength and temperature dependent as a result of Equation (30). The flux calculations assume the losses due to atmosphere are negligible and the radiance emitted at the aperture wheel for a given aperture size, A_{bb}, is the same as the radiance emitted by the blackbody source.

By setting the aperture wheel to a known area, placing the blackbody source at a known distance, and aligning the axial IR path to be in the center of the aperture and the

95
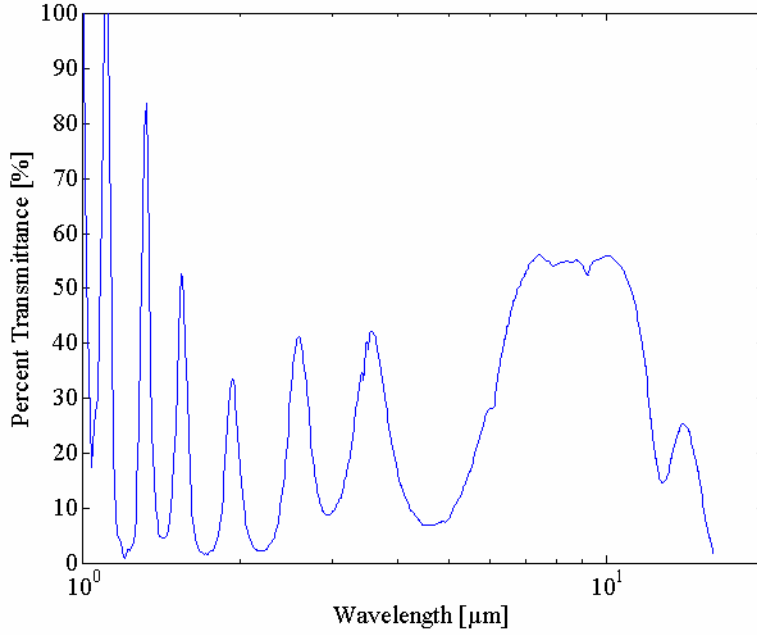
Figure 57. Graph of spectral transfer function, from 1 μm to 16 μm, for Catamount Corporation PalmIR 75-mm lens system.

center of the lens, the system should have a calculable flux incident on the lens. The lens system itself has a spectral transfer function, $T_l(\lambda)$, that transmits a percentage of the incident flux as a function of the wavelength. Using an FTIR Raman Spectroscopy system, the lens system (Catamount Corporation PalmIR 75-mm lens) was analyzed to have the spectral transfer function shown in Figure 57.

The PIP material has a high absorbtance due to the carbon black and is assumed to be independent of wavelength for this IR spectrum. Equation (32) then describes the flux transmitted through the lens system:

$$\phi_d(\lambda, T) = T_l(\lambda) L_{e,\lambda}(\lambda, T) A_s \Omega_o . \tag{32}$$

96
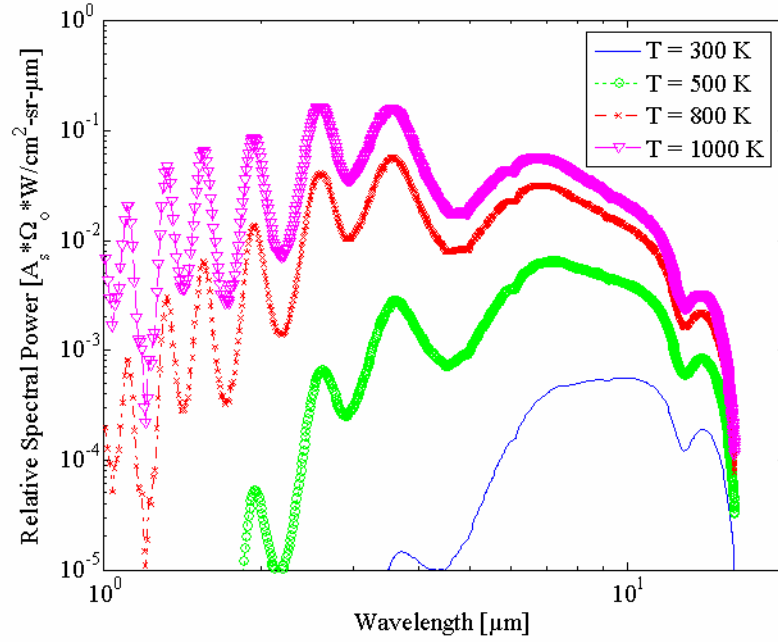
Figure 58. Relative spectral power transmitted through test lens system for blackbody radiation source temperatures of 300 K, 500 K, 800 K, and 1000 K.

By multiplying Equation (32) by the transmittance for the spectral range of the lens system transfer function, the spectral transfer function can be superimposed on the flux equation to show the relative spectral power transmitted through the lens system from a blackbody source. Figure 58 shows the relative spectral power transmitted through the lens system for the blackbody source at several different temperatures.

For a specific aperture size (A_{bb}), IR path distance (d_p), lens system surface area (A_l), blackbody radiation source temperature (T), wavelength spectrum (λ_1 to λ_2), and under the previously stated assumptions, a transmitted power can be calculated for the test setup. If A_{bb} is approximated as a point source and all sources aside from A_{bb} are negligible, a flux can be calculated at any distance from the optic, given these two assumptions. By placing the sensor a known distance (d_s) from the optic and by knowing

97

the area of the pixel under test (A_d), the incident power on the pixel sensor under test can be calculated.

The initial test setup was completed and four different un-etched Suspended Membrane designs and five different Raised Cantilever Arm Pixel Sensors were fabricated and tested at a path distance, d_p, of 35 inches, blackbody aperture, A_{bb}, of 1 square inch, blackbody temperature, T, of 90 °C, 150 °C, and 400 °C, sensor distance, d_s, at the focal point of the lens system, and optical chopping rate of 1.4 Hz. The sensors did not respond when biased by the readout circuit. If a sensor response was present, the electrical noise present in the readout circuit response was greater than the voltage response of the biased circuit. Various pixel resistances were measured directly in the range of 3.5 to 8 MΩ using an Agilent Model 34401A 6 ½ Digit Digital Multimeter. The pixel sensors may not have worked correctly because of pixel stiction due to the PIP material application process, possible electrical shorts caused by PIP material covering the pixel address wiring, or changes in the PIP material properties due to film thickness. Figure 59 shows pictures of a Raised Cantilever Arm Pixel Sensor that was tested, (a) before applying the PIP material, and (b) after spin coating with PIP material.

The following paragraphs explain the methodology attempted to experimentally derive the figures of merit for the pixel sensors tested. Recall that Equation (13) states the responsivity of the system is the voltage output per unit power incident on the system. By biasing the pixel with a known current and chopping the IR signal at a known rate, the pixel voltage output due to incident IR energy can be determined. Knowing the bias current and pixel voltage with and without IR illumination gives the base pixel resistance
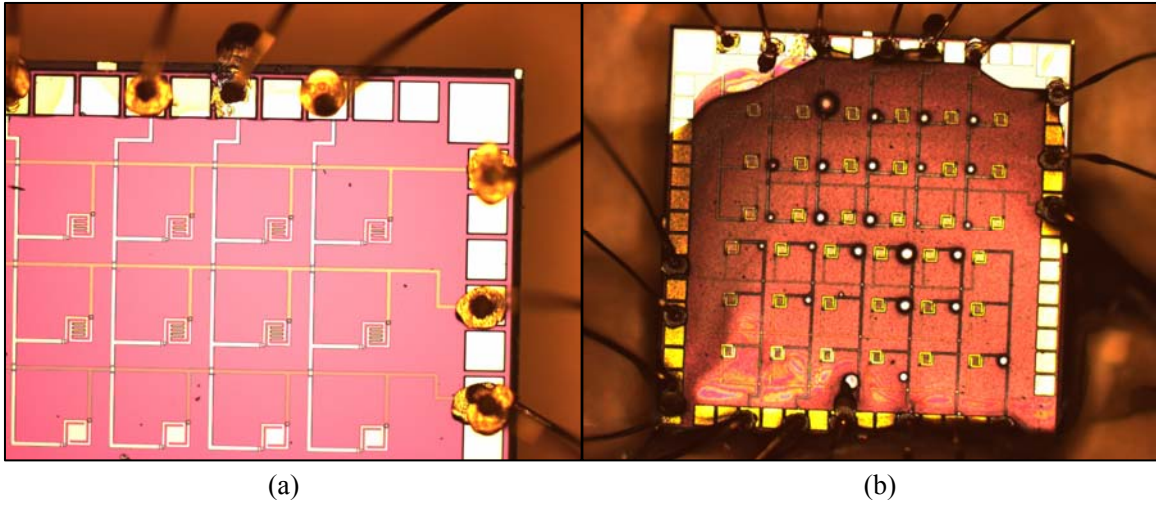
Figure 59. Pictures of Raised Cantilever Arm Pixel Sensor tested (a) before PIP material is applied and (b) after PIP material is spin coated.

by Ohm's law and the pixel system responsivity. The bias current is generated by an op-amp circuit and signal generator, and is powered by a DC power supply. Appendix A shows the circuit diagram and derivation of the circuit equation. The pixel sensor current and voltage are measured using two automated multimeters as an ammeter and voltmeter. The data recording and control program were implemented using Agilent VEE 6.1 and the details are outlined in Appendix B.

Using the oscilloscope, a transition edge of the IR signal can be determined. As mentioned in section 4.3, the thermal response time is defined as the pixel heat capacitance divided by the total effective thermal conduction. The thermal response time can be measured as the voltage fall time from 90% of signal steady state to 10% above the "dark" voltage baseline.

To determine the NEP, the pixel sensor system must be in steady state and the incident power must be reduced to cause a signal-to-noise ratio of 1. The incident power

can be reduced by changing the temperature of the blackbody radiation source, reducing the total power, and by moving the sensor closer to the lens system, reducing the power per unit area incident on the pixel. When the pixel sensor system has attained a steady state signal-to-noise ratio of 1, then the NEP is equal to the incident power.

The detectivity must be directly calculated from the known pixel area and fill factor with a measured system bandwidth. The ROIC system bandwidth is measured to be 1000 Hz. Appendix C details the experiment and measurements taken to determine the ROIC system bandwidth. The detectivity is calculable from the measured responsivity using Equation (21).

The last figure of merit, NETD, can be only calculated, using Equation (23), relative to the assumptions given during the Modeling chapter. An average transmittance of the optics and equivalent noise voltage can be calculated given the previous transmittance data and the experimentally measured NEP. The pixel area, optic's f/#, and responsivity are known quantities. However, the change in incident power per unit area relative to the temperature change over the spectral band is not measurable, but can be assumed to be the same value, 6×10^{-5} [W/cm^2·sr·K], used in the Modeling chapter for 8 – 12 μm. The calculated value from the experimentally-derived values and the value from the Modeling chapter will show the relative error of the assumptions made during modeling.

This section has outlined the initial test setup used to test fabricated Raised Cantilever Arm Pixel Sensors and the results of testing, and the methodology for deriving the figures of merit for a completed Raised Cantilever Arm Pixel Sensor or Suspended

Membrane Pixel Sensor. Due to time constraints and sensor fabrication issues, no data was recorded using the initial test setup.

6.5 Simplified Test Setup and Results

Due to the lack of sensor response from the fabricated Raised Cantilever Pixel Sensors to a controlled IR signal, a simple and straightforward test was performed to determine the viability of the fabricated MEMS designs as sensor platforms for the PIP.

A Suspended Membrane Pixel Sensor was back-etched using the MLPC laser-micromachining technique, resulting in a square hole of dimensions 1.2-mm wide by 1.2-mm long by 462-μm deep. The test die was cleaned and packaged as per the method outlined in the Design and Fabrication chapter. Instead of spin coating the sensor, a pipette was used to directly deposit a very small amount of PIP material to the surface. The PIP material was directly applied versus spin coating because it was not known if spin coating the PIP material to a thin layer was adversely affecting the PIP material

(a)   (b)
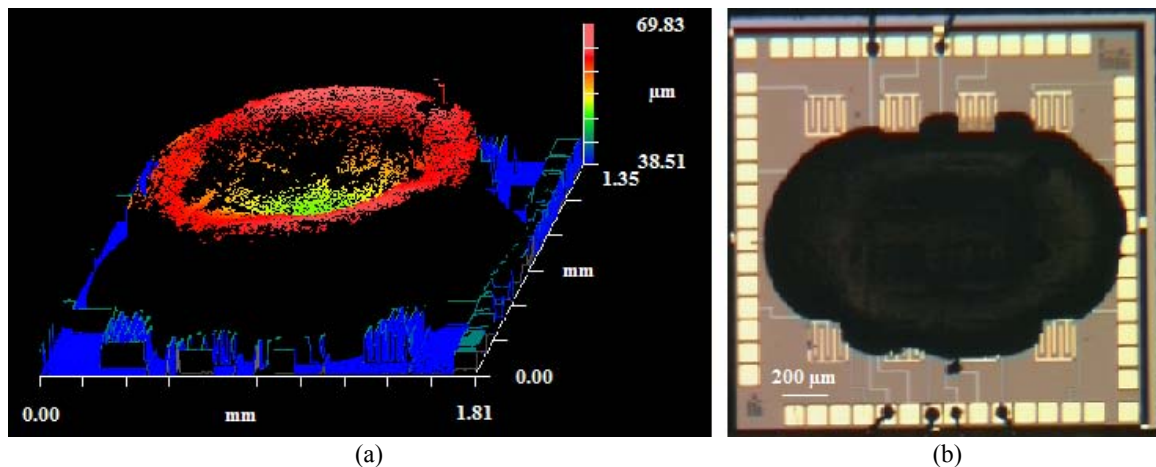
Figure 60. Zygo NewView 5000 (a) oblique color topography and (b) digital picture of fabricated Suspended Membrane Pixel Sensor.

sensing properties. The sensor was dried in a controlled humidity box. Figure 60 shows

an oblique color topography and digital picture of the fabricated sensor.

The dried PIP material shows a distinct toroid-like shape that varies in thickness

over the surface area of the Suspended Membrane Pixel Sensor. Figure 61 shows a top

view color topography map with a profile line of the PIP material on the Suspended

Membrane Pixel Sensor. The profile line plot is shown in Figure 62, which shows a

profile plot bisecting the PIP material on the Suspended Membrane Pixel Sensor. The

height is shown relative to the lowest measured point, which is the 2nd Oxide

PolyMUMPs layer.

The test setup placed the sensor facing up on a test bench and was exposed to

ambient room conditions. The sensor resistance was directly measured using a Keithley

6517A Electrometer/High Resistance Meter. A four D-cell Mag-Light with a Hoya R72
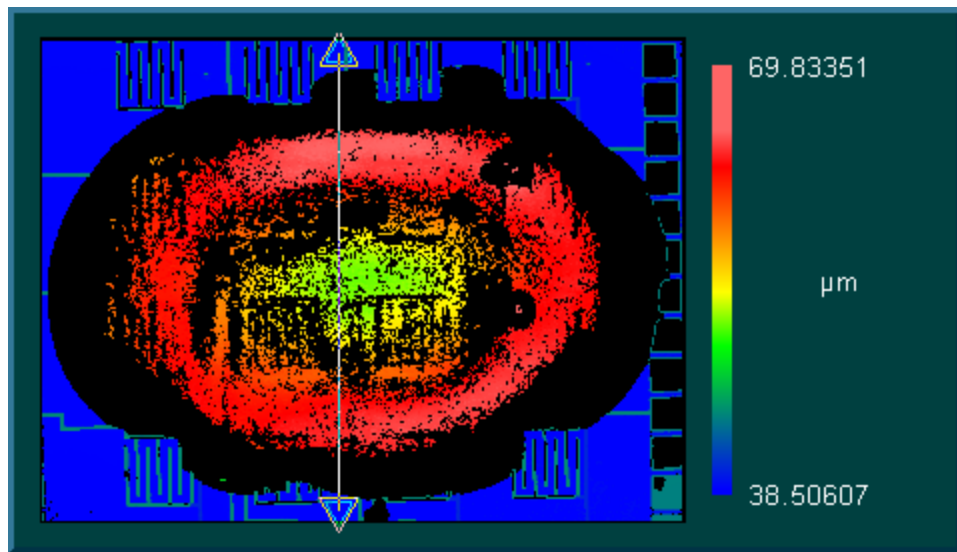
Figure 61. Top view color topography map and profile line of fabricated Suspended
Membrane Pixel Sensor.
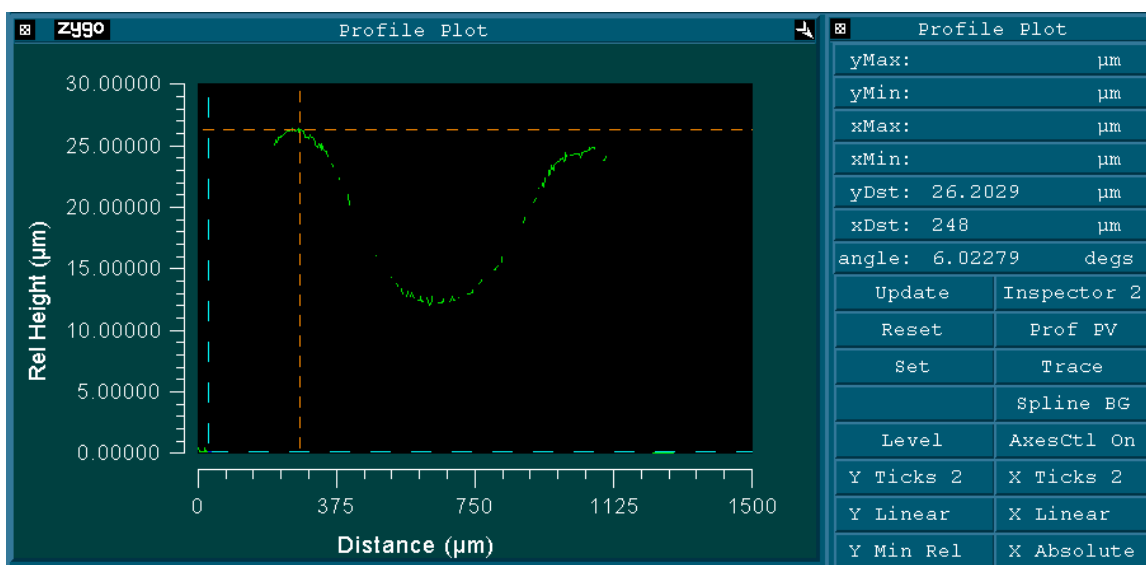
Figure 62. Profile plot of relative measured height of PIP material on Suspended Membrane Pixel Sensor.

IR filter held approximately 6 inches from the sensor provided filtered broadband IR energy to stimulate a response. The flashlight was held on for approximately 1 second. Figure 63 shows the measured sensor resistance over time. The sensor resistance was allowed to stabilize to the test environment by sitting out in the open before exposing the sensor to the flashlight stimulus.

Figure 64 shows the measured resistance data normalized by dividing the resistance data by the initial resistance and time weighting the data over the specified range to make the end data point even with the beginning data point. The time weighting was performed by subtracting one from the final normalized resistance point, multiplying by the ratio of the current time over the final time, and subtracting the value from the current normalized resistance data point. The normalized resistance plot shows percentage of resistance change, which is a part of the TCR, α_B. If a temperature change

Figure 63. Plot of measured resistance changes due to flashlight stimulus for Suspended Membrane Pixel Sensor after stabilizing for 50 seconds.

over a range could be derived or measured for this percentage resistance change, then the temperature coefficient of resistance could be calculated.

The normalized resistance decreases for a given stimulus, confirming the TCR is negative for an increase in incident energy. The differing response magnitudes suggest different amounts of power were absorbed by the sensor and the largest peak response suggests the sensor has a finite power dissipation rate, described by a thermal response time. The relatively stable "dark" times suggests that the NEP is very low compared to the signal response. The noise level during the "dark" time has a very low power compared to the power change caused by the signal source. The sampling rate of the multimeter and DC biasing of the sensor are causes of limitations and errors in the data. The sampling rate of the multimeter may be slower than the time response of the sensor
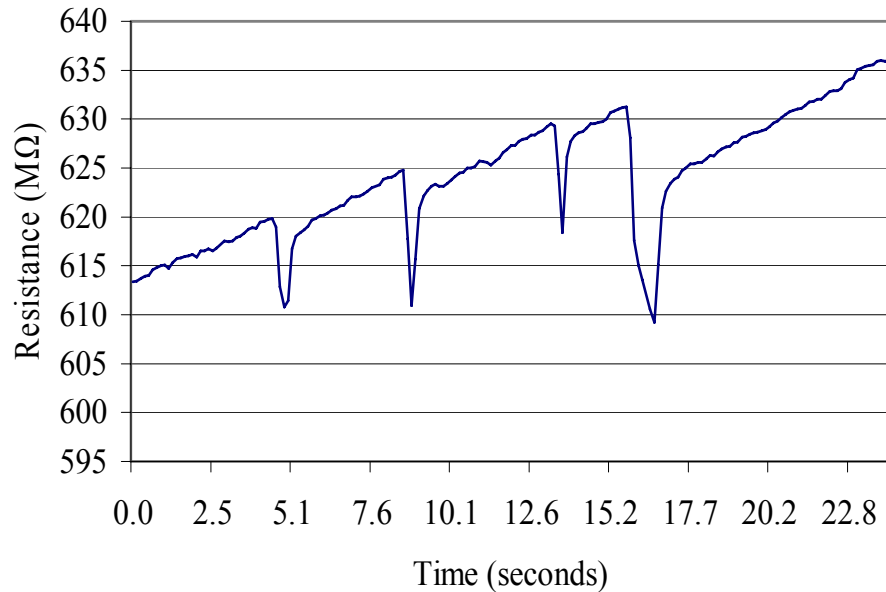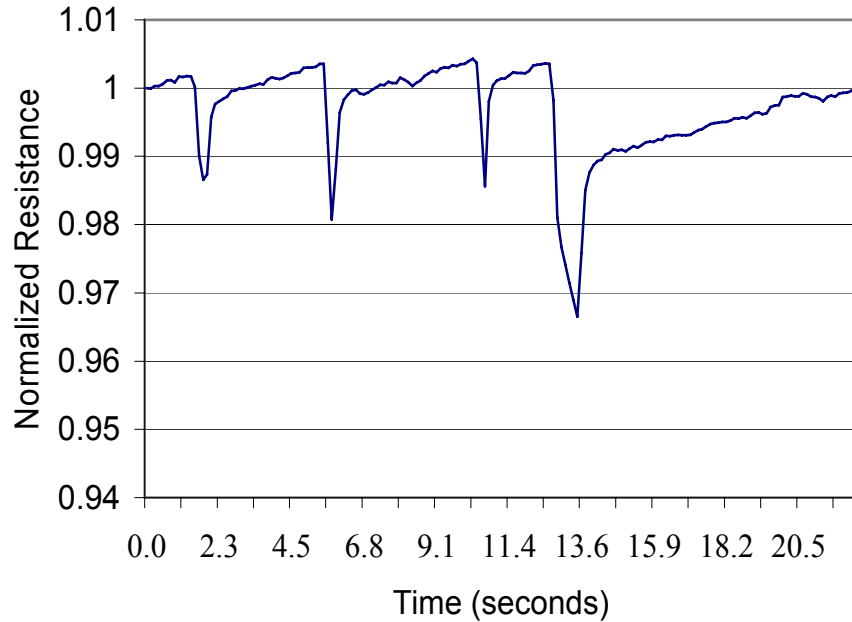
Figure 64. Plot of normalized resistance changes due to flashlight stimulus for Suspended Membrane Pixel Sensor after stabilizing for 50 seconds.

and irregular sample spacing may cause the multimeter to miss output changes. The

constant increasing resistance bias is assumed to be caused by the constant DC biasing of

the sensor generated by the multimeter to read resistance. The resistance bias

phenomenon is the same as observed by AFRL scientists when biasing the sensors with a

constant DC current to read pixel response voltages. The growing bias trend observed

previously by the AFRL scientists has shown the PIP material resistance increases until

the resistance is no longer measurable. The PIP material then becomes fixed at a very

high resistance and does not recover its previous properties. The AFRL believes this

phenomenon to be the result of inducing polarization of the PIP material which impedes

current flow. This behavior has only been observed in the PIP material when it is

subjected to a constant DC bias, which the multimeter is inducing in the PIP material in order to read the resistance of the sensor.

A simple measure of the thermal time constant may be taken if the flashlight signal were chopped or turned on and off rapidly. The multimeter sampling speed would be the shortest time constant that is measurable and the DC bias would cause a bias effect in reading the fall time of the signal cutoff.

The remaining figures of merit are not calculable from this rudimentary test setup, nor if any simple modifications were made. The responsivity, NEP, detectivity, and NETD require more accurate methods of capturing data and biasing the sensor.

6.6 Summary

The test setup and methodology for deriving and calculating the figures of merit of a Pixel Sensor was used in this chapter. Due to time constraints and fabrication complications, the initial test setup was implemented in a complete test environment but a completed pixel sensor was unable to be tested completely to derive the figures of merit. A simplified test setup was implemented instead to demonstrate that the fabricated MEMS platform was still a potential solution for a microbolometer sensor using the PIP material.

VII. Conclusions

7.1 Chapter Overview

The purpose of this chapter is to summarize the thesis, cover the thesis goals, state the conclusions derived from the fabrication experiments performed to create the Raised Cantilever Arm Pixel Sensor and the Suspended Membrane Pixel Sensor, design mistakes, the modeled figures of merit, final data derived from the test performed, and to propose further topics of exploration for research regarding PIP material for use in infrared sensors using MEMS pixels.

7.2 Summary of Thesis

This thesis has covered exploratory research, design, modeling, and fabrication of an infrared sensor using a novel protein impregnated polymer material on micromachined pixels. This research is the first to explore applying a biologically-based IR sensitive polymer material to MEMS structures to create a microbolometer IR sensor. The design and fabrication covered two different pixel designs and the modeling included five figures of merit that are used for qualitative comparisons. Although a complete functioning and modeled infrared sensor was not accomplished, much was learned about designing, modeling, and fabricating a PIP material infrared sensor.

7.3 Thesis Goals

The goals of this thesis addressed the problems of large pixel size, low density pixel arrays, and low sensitivity of the pixels created by AFRL. The MEMS structures used for pixel arrays allowed small pixel sizes and high density pixel arrays. The simple

107

test performed on a laser-machined Suspended Membrane Pixel Sensor showed that the sensor responded well to a direct stimulus of IR filtered light. This test shows that a non-optimized pixel structure with applied PIP material is sensitive enough to function as an IR sensor.

7.4 Design and Fabrication Issues

The design and fabrication of the Raised Cantilever Arm Pixel Sensor was based on simple assumptions regarding the spin thickness properties of the PIP material and the method that the material would coat a suspended pixel structure. When the PIP material was applied by pipette and then spin-coated across the surface of the PolyMUMPs test dice, the PIP material spin coating behavior differed from the thin conformal behavior shown by the initial spin testing. The spin coating procedure did not consistently coat the pixels in a conformal manner due to the inconsistent volume of PIP material applied by the pipette, the possibility of trapped air in the applied PIP material, and the imperfect alignment of the sensor package on the spinner vacuum chuck. Different volumes of PIP material coated the pixel sensors with different thicknesses. Trapped air caused the PIP material to spread unpredictably across the entire sensor package or caused anomalies as shown in Figure 45. Off-center alignment of the sensor package on the spinner vacuum chuck caused the PIP material to spread primarily in one direction. The residual stress cantilever arms did not always remain suspended above the substrate after spin coating. The cantilever arms were enveloped by the liquid PIP material as it was applied. As the PIP material dried, the residual stress of some of the cantilever arms was overcome by surface tension forces of the PIP material. The spin coating behavior of the PIP material

108

is different from the modeled behavior and will result in different figures of merit. The

spin coating procedure should be either modified or replaced with a more consistent

method of applying the PIP material in order to eliminate material uniformity problems

and to attain the best possible figures of merit.

Two design complications occurred with the Raised Cantilever Pixel designs.

First, by using the Metal and Poly 2 layers to create residual stress cantilevers, the pixel

fabrication procedure required etching away the Oxide layers to release the cantilever

arms. Etching the Oxide layers exposes all Poly layers, causing cross-talk between

address lines and pixels that are coated with PIP material. Second, the PolyMUMPs

minimum spacing design rule of 2 μm was violated by creating 1-μm Poly 2 "finger"

spaces in Raised Cantilever Arm Pixel designs. By violating the design rule, the

PolyMUMPs mask error tolerances were larger than the 1-μm space allowed for, causing

the pixel area to be a solid Poly 2 surface instead of interdigitated fingers. The solid

pixels are low resistance electrical pathways compared to the PIP material resistance,

rendering the solid pixels useless as sensors. Also, if the 1-μm finger designs were

implemented in a common-row and common-column addressing scheme, the solid pixels

were electrical shorts across the entire array. The solid pixels had to be removed to test

other designs. The design rules should be followed in the future in order to guarantee

uniformity of the PolyMUMPs test dice and to ensure working pixel designs.

The design and fabrication of the Suspended Membrane Pixel Sensor was based

on the assumption that the crystalline silicon wafer substrate could be removed from the

backside of the pixels. Wet etching with a KOH solution required a several-hour bath

under raised temperature conditions. A successful method of protecting the front and sides of the PolyMUMPs test dice during this wet-etch process was not found. The laser-machining method of removing the substrate could not achieve the desired depth and uniformity without damaging the front face of the pixel sensor. Further etching of the laser-machined PolyMUMPs test dice by wet etching with KOH did not succeed in removing the remaining substrate material. Wet etch attempts on the laser-machined test dice occasionally caused etch damage to the pixel address lines and pixel structures by seepage of etch solution through protective barriers or by etching through undetected laser-machined holes. The intent of the Suspended Membrane Pixel design is to thermally isolate a pixel by removing the bulk crystalline silicon substrate beneath the pixel. The silicon substrate can also be etched away from the pixel side if the front layers of the PolyMUMPs test dice were protected.

General fabrication and design complications that occurred included improperly wire bonding the PolyMUMPs test dice to the DIP package, causing electrical shorts within the PolyMUMPs test dice, cross talk between common-row and common-column addressed pixels, and spin coating excess PIP material across the test dice and packaging. Electrical shorts within the PolyMUMPs test dice provided low resistance electrical paths for the AC bias current to flow through. The pixel sensor response would not be discernable from the voltage response of the bias current traveling through the electrical short. A source of cross-talk noise can occur between pixels that were addressed with a common-row and common-column scheme. All pixels covered with the PIP material, in addition to the pixel being directly biased with a signal, provide a parallel electrical path

110

for the bias signal. This means the bias signal will pass through multiple pixels in series in addition to the pixel directly addressed. Also, by spin coating excess PIP material across the PolyMUMPs test dice and the package, the PIP material can act as an electrical pathway to multiple points on the test dice, allowing cross-talk between pixel sensor wire bonds and the silicon wafer substrate. Any cross-talk should add to the effective electrical noise voltage of the pixel, causing the NEP and NETD to be greater than expected.

The Raised Cantilever Arm Pixel design functions poorly when spin coating is used to apply the PIP material. A more uniform and precise method of applying the PIP material to each pixel individually could resolve complications such as pixel stiction and pixel and wire cross-talk for both Raised Cantilever Arm Pixel and Suspended Membrane Pixel designs. The Suspended Membrane Pixel design etch time can be reduced if the pixels, bond pads, and address wiring of the PolyMUMPs test dice were selectively protected during a wet chemical etch. The use of a common-row and common-column addressing scheme should be avoided to eliminate paths of electrical cross-talk.

7.5 Figures of Merit

The modeling of the figures of merit includes assumptions of the PIP material properties, such as TCR, thermal conductivity, density, specific heat, and absorptance. These material properties have not been verified for small pixel areas and micrometer film thicknesses, or variations of these properties for different factors such as time, humidity, drying processes, or material batches.

111

The modeled figures of merit for the Raised Cantilever Arm Pixel are viable for use in an infrared sensor and are on the same order of magnitude as reported by exploratory research for other infrared sensors [39]. The data measured during the simple experiment using a laser-machined Suspended Membrane Pixel Sensor suggests that the PIP material with MEMS pixels is still a viable solution for an infrared sensor. However, the modeled figures of merit suggest that the laser-machined Suspended Membrane Pixel Sensor should not be used as an infrared sensor due to its low responsivity and high NETD. The contradiction between the data measured and the modeled figures of merit suggest that the model accuracy and PIP material properties should be verified.

7.6 Topics of Exploration

It is suggested that further research be done to characterize the PIP material properties that directly pertain to the modeling of the figures of merit. The PIP material absorptance and absorption coefficient can be derived by applying varying thicknesses of PIP material to an IR transparent material and performing FTIR Raman spectroscopy measurements on the PIP material. Also, methods of applying the PIP material in a more precise and uniform way will improve modeling accuracy and prevent cross-talk noise. Further design exploration should cover methods of addressing each pixel individually and in a manner that is protected from cross-talk, different methods of thermally isolating the PIP material, and other fabrication processes that can easily incorporate the PIP material. A method of packaging the sensor under vacuum will simplify modeling, as well as provide better thermal isolation for each pixel.

Appendix A: ROIC Equation Derivation

The biasing and readout circuit is a dual op-amp, voltage-controlled current source. By driving the circuit with a controlled AC voltage signal, the pixel sensor will be biased with a controlled AC current signal. The voltage change across the pixel sensor is read using a voltmeter. The AC current signal is monitored with an ammeter. The voltage and current are used to derive the resistance using Ohm's law. The circuit description and components were obtained from AFRL. The circuit was assembled by the student at AFRL. Figure 65 shows the ROIC and component labels. The op-amp source voltage (V_s) was provided by an Agilent E3631A Triple Output DC Power and was set at 15 volts.
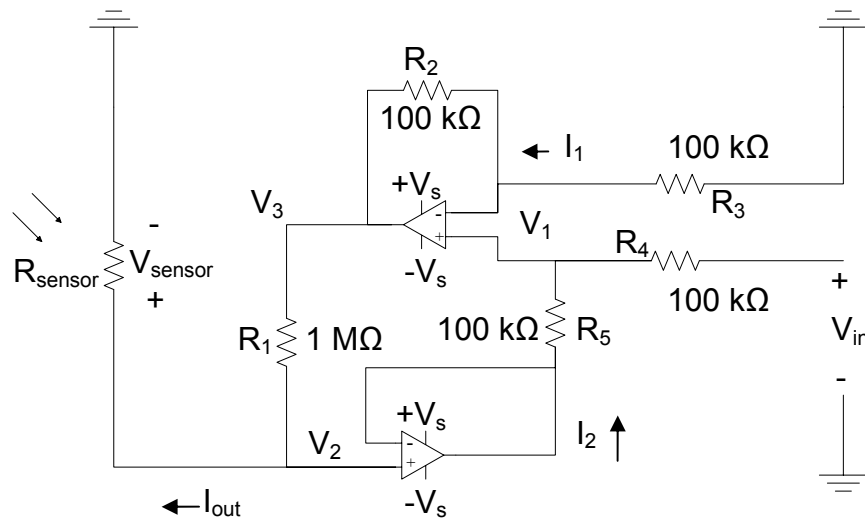

Figure 65. Readout circuit diagram and equation component labels.

Equations 33 through 36 are derived by Kirchoff's current law and assume ideal op-amp behavior:

$$I_{out} = \frac{V_3 - V_2}{R_1} \tag{33}$$

$$I_1 = \frac{V_1 - V_3}{R_2} = \frac{-V_1}{R_3} \tag{34}$$

$$I_2 = \frac{V_2 - V_1}{R_5} = \frac{V_1 - V_{in}}{R_4} \tag{35}$$

$$I_{out} = \frac{V_{sensor}}{R_{sensor}}. \tag{36}$$

Since R_2, R_3, R_4, and R_5 are equal resistances, Equations 34 and 35 can be reduced to the equivalent voltage expressions shown in Equations 37 and 38:

$$V_3 = 2V_1 \tag{37}$$

$$V_{in} = 2V_1 - V_2. \tag{38}$$

Combining Equations 37 and 38 yields Equation 39:

$$V_{in} = V_3 - V_2. \tag{39}$$

Substituting Equation 33 into Equation 39 yields Equation 40:

$$V_{in} = I_{out}R_1. \tag{40}$$

Combining Equations 36 and 40 yield an expression of the sensor voltage in terms of the input bias voltage, circuit resistance, and sensor resistance shown in Equation 41:

$$V_{sensor} = \frac{R_{sensor}}{R_1}V_{in}. \tag{41}$$

Equations 36, 40, and 41 can be used to effectively model the circuit bias voltage, sensor bias current, sensor voltage, and sensor resistance.

Appendix B: Data Recording and Control Program

The ammeter, signal generator, and voltmeter shown in Figure 55 were controlled and monitored using the lab automation program, Agilent VEE 6.1. The ammeter and voltmeter were Agilent Model 34401A 6 ½ Digit Digital Multimeters. The signal generator was an Agilent Model 33250A 80 MHz Function / Arbitrary Waveform Generator. The program controlled the hardware via an IEEE-488 General Purpose Interface Bus (GPIB) controller. The ammeter, signal generator, and voltmeter were addressed individually on addresses 715, 710, and 705, respectively. Figure 66 shows a picture of the main program dialog boxes and interconnections.

The "current setup", "siggen setup", and "voltage setup" dialog boxes controlled the initialization and setup of the hardware. The "Delay" control box allows the setup program to complete all of its functions before initializing the data recording. The "On Cycle" control box provides a time stamp (Stamp) in the "To File" control box. The
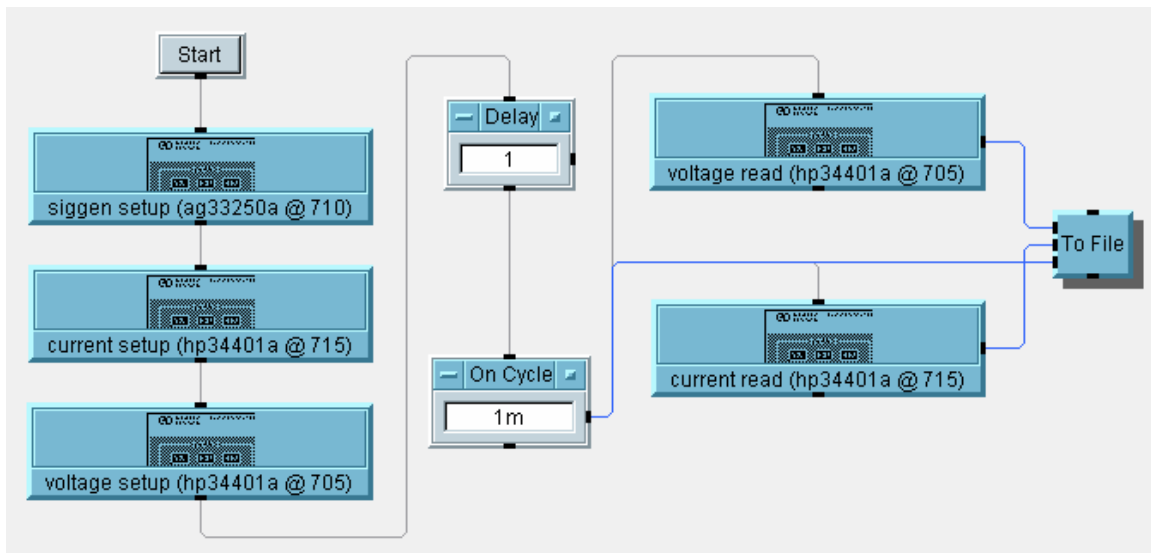

Figure 66. Agilent VEE 6.1 control program for recording sensor data.

"current read" and "voltage read" control boxes sample the sensor current (Current) and sensor voltage (Voltage) and provide the values to the "To File" control box. The "To File" control box writes the time-stamped sampled current and voltage data to a comma-delimited ASCII data file. The maximum observed data sampling rate is 30 times per second. The control box code is provided, where applicable.

"current setup" control box code:

```
WRITE TEXT "*rst" EOL
WRITE TEXT "func \'curr:dc\'" EOL
WRITE TEXT "sens:curr:DC:rang 0.01" EOL
WRITE TEXT "sens:curr:DC:res min" EOL
WRITE TEXT "sens:curr:dc:nplc min" EOL
WRITE TEXT "inp:imp:auto on" EOL
WRITE TEXT "sens:zero:auto off" EOL
WRITE TEXT "TRIG:SOUR BUS" EOL
WRITE TEXT "disp off" EOL
```

"siggen setup" control box code:

```
WRITE TEXT "func squ;:freq 0.5;:volt 5.0" EOL
WRITE TEXT "outp on" EOL
```

"voltage setup" control box code:

```
WRITE TEXT "*rst" EOL
WRITE TEXT "func \'volt:dc\'" EOL
WRITE TEXT "sens:volt:DC:rang 10" EOL
WRITE TEXT "sens:volt:DC:res min" EOL
WRITE TEXT "sens:volt:dc:NPLC min" EOL
WRITE TEXT "inp:imp:auto on" EOL
WRITE TEXT "sens:zero:auto off" EOL
WRITE TEXT "TRIG:SOUR BUS" EOL
WRITE TEXT "disp off" EOL
```

"current read" control box code:

```
WRITE TEXT "INIT" EOL
WRITE TEXT "*trg" EOL
WRITE TEXT "fetch?" EOL
READ TEXT curr REAL64
```


"voltage read" control box code:

```
WRITE TEXT "INIT" EOL
WRITE TEXT "*trg" EOL
WRITE TEXT "fetch?" EOL
READ TEXT volt REAL64
```


"To File" control box code:

```
WRITE TEXT Voltage, ","
WRITE TEXT Current, ","
WRITE TEXT Stamp EOL
```

Appendix C: ROIC Bandwidth Analysis

Information provided by the AFRL indicated the highest sampling frequency of the ROIC in Figure 65 was around 1 kHz. The circuit bandwidth was tested for a value to use in the Modeling chapter for the noise bandwidth, B. The sensor resistance, R_{sensor}, was 1 MΩ resistor and the supply voltage, V_s, was 15 volts. The oscilloscope used to capture the pictures was an Agilent Model 54641D 2+16 Channel, 350 MHz Mixed-Signal Oscilloscope. The input voltage was provided by an Agilent Model 33250A 80 MHz Function / Arbitrary Waveform Generator. All figures show the output sensor voltage, V_{sensor}, as the top waveform and the reference input signal voltage, V_{in}, as the bottom waveform. Figures 67, 68, 69, and 70 show the circuit voltage responses to an input frequency of 20, 100, 300, and 500 Hz, respectively.
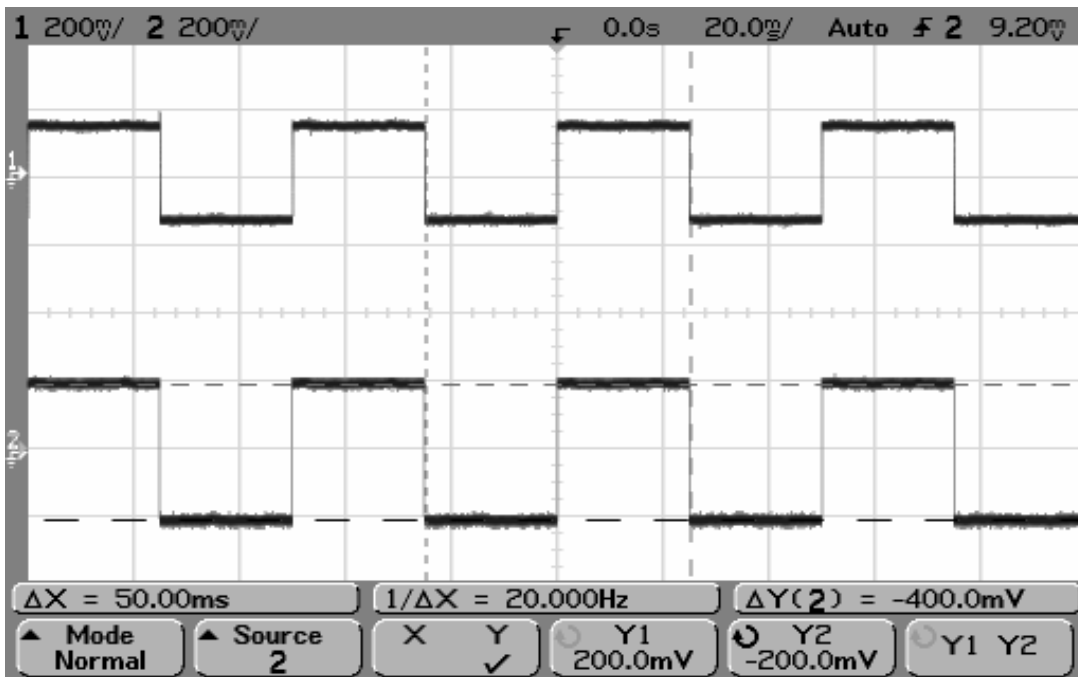
Figure 67. ROIC voltage response to 20 Hz input bias signal.
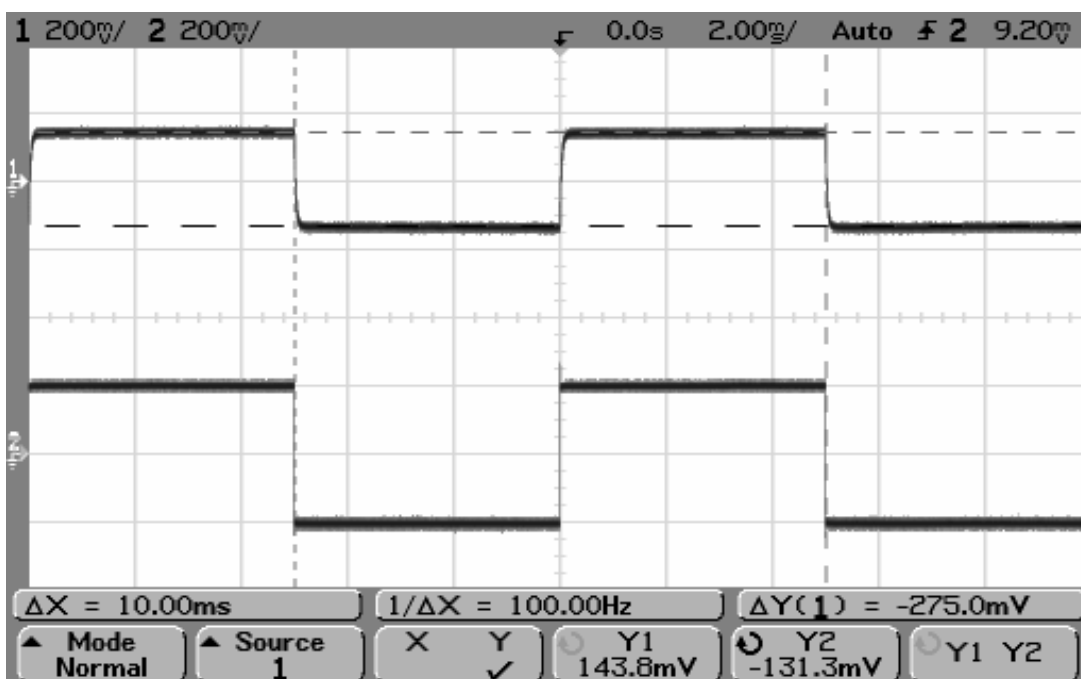
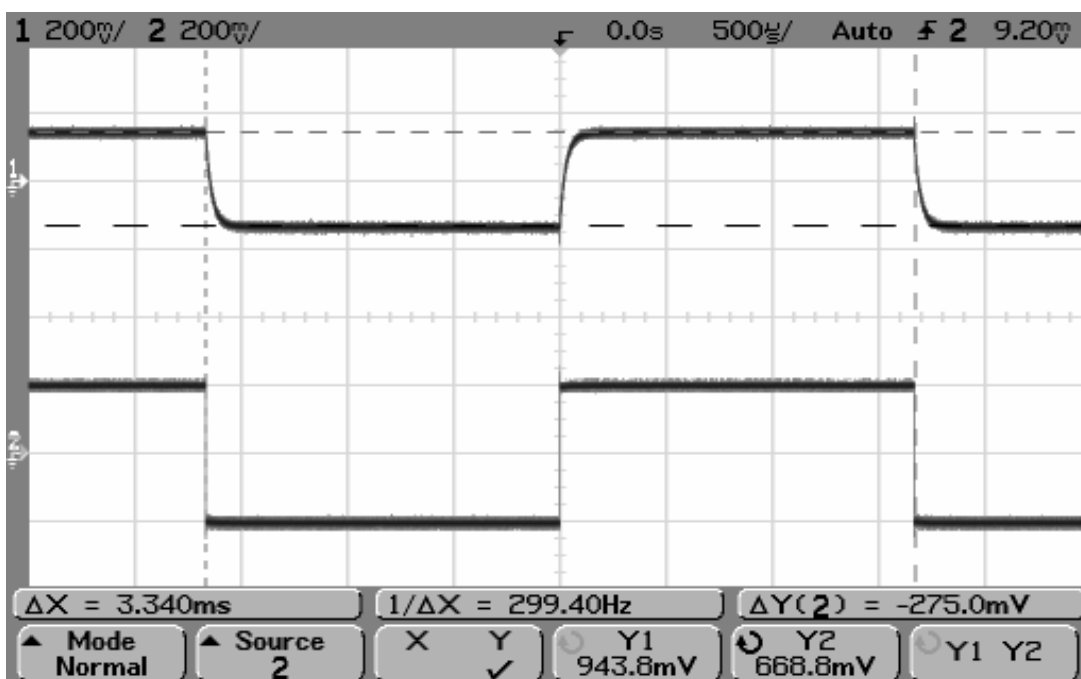Figure 68. ROIC voltage response to 100 Hz input bias signal.

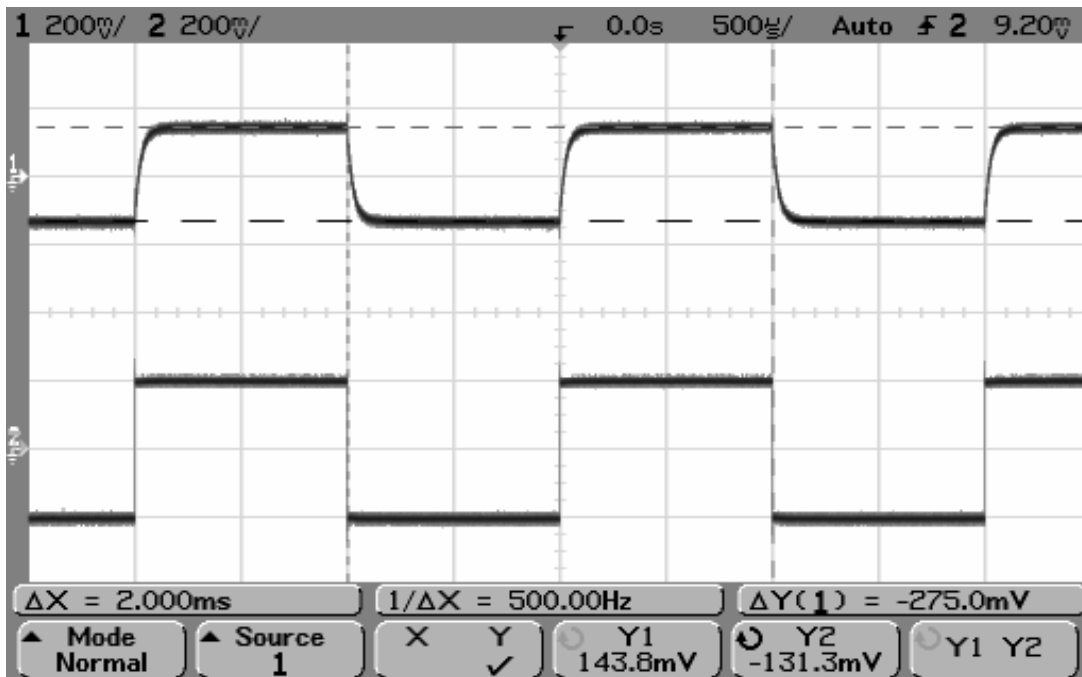Figure 69. ROIC voltage response to 300 Hz input bias signal.

Figure 70. ROIC voltage response to 500 Hz input bias signal.

At 800 Hz, the 90% rise time of the voltage response begins to approach 10% of the pulse duration. Figure 71 shows the voltage response to an input frequency of 800 Hz. At 1 kHz, the rise time to 90% is 54 μs, or 10.8% of the pulse duration, as indicated by Figure 72. At 1350 Hz, the rise time to 90% is 59 μs, or 15.95% of the pulse duration, as indicated by Figure 73. By using 10% of the pulse duration as the cutoff limit for the signal bandwidth, 1 kHz is approximately the signal bandwidth. Above 1 kHz, the ROIC causes signal distortion and should be filtered to exclude signals above 1 kHz to accomplish a noise bandwidth of 1 kHz.
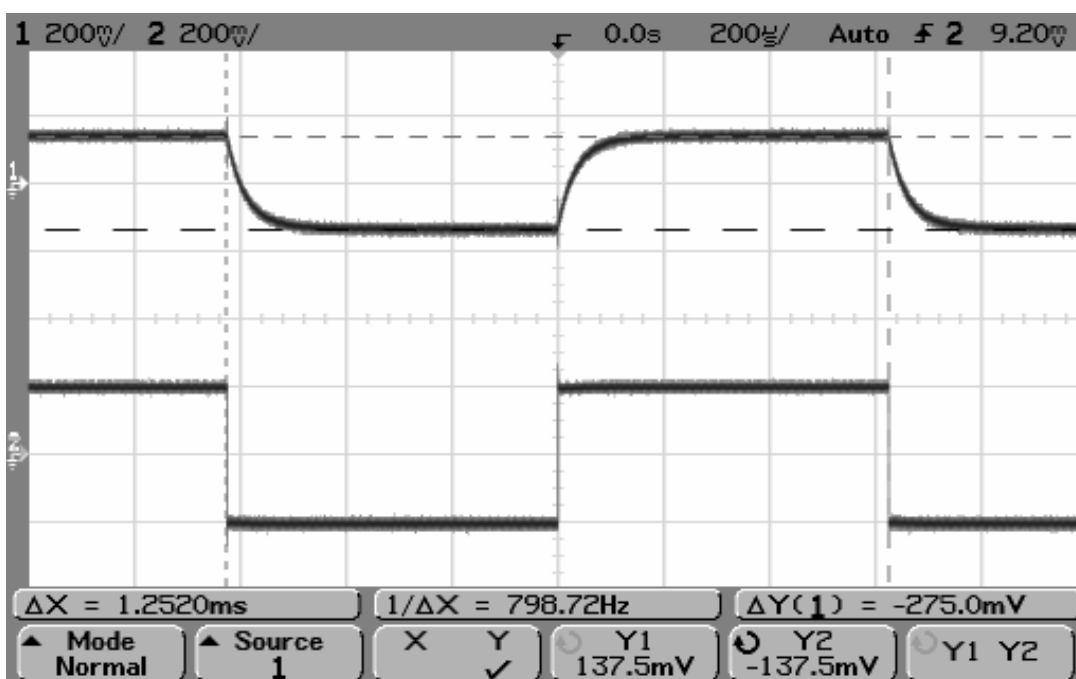
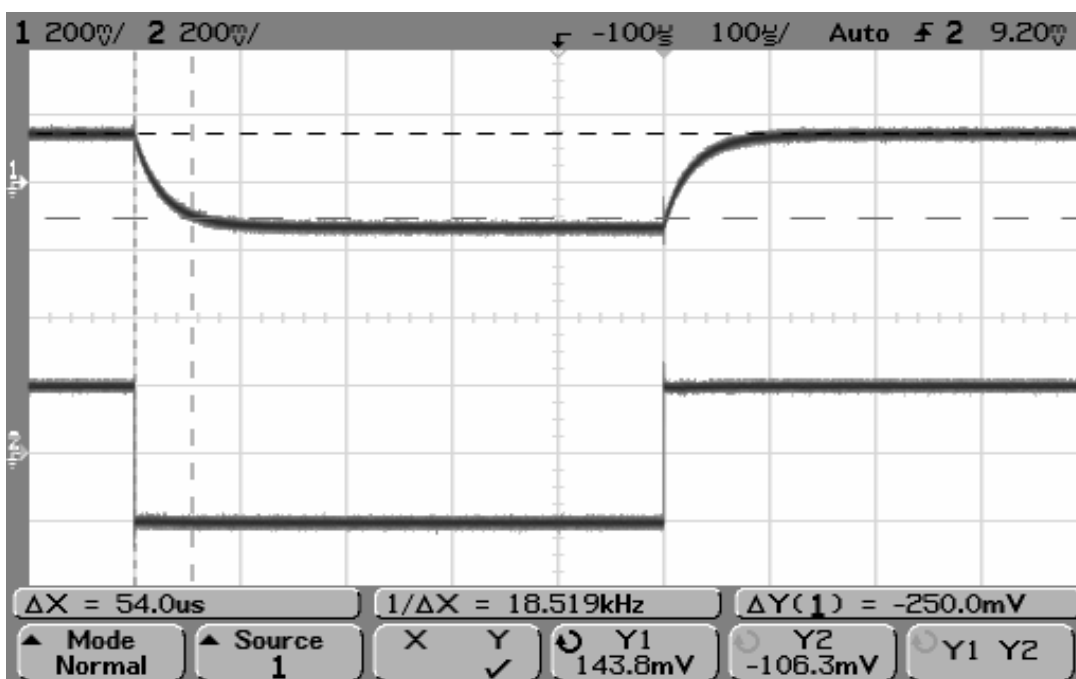Figure 71. ROIC voltage response to 800 Hz input bias signal.

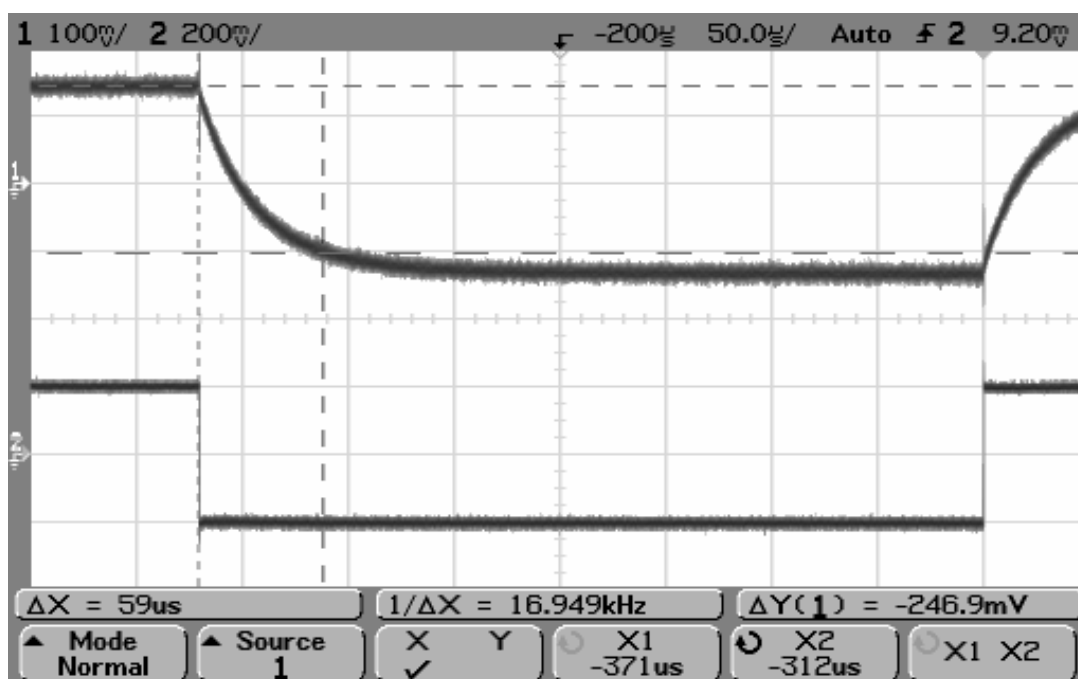Figure 72. ROIC voltage response to 1 kHz input bias signal.

Figure 73. ROIC voltage response to 1350 Hz input bias signal.

Bibliography

[1]   Buser, R. G. and M. F. Tompsett, "Uncooled infrared imaging arrays and systems: Historical overview" in *Uncooled Infrared Imaging Arrays and Systems, Semiconductors and Semimetals*, P.W. Kruse and D.D. Skatrud, Eds. New York: Academic, vol. 47, pp. 1-14, 1997.

[2]   Sierra Pacific Innovations, http://www.ir55.com/infrared_IR_camera.html, dated 11 August 2005.

[3]   Naik, R. R., S. M. Kirkpatrick, and M. O. Stone, "The thermostability of an α-helical coiled-coil protein and its potential use in sensor applications," *Biosensors and Bioelectronics*, vol. 16, pp. 1051-1057, 2001.

[4]   Mottin, E., A. Bain, P. Castelein, J. L. Ouvrier-Buffet, J. L. Tissot, J. J. Yon, and J. P. Chatard, "Amorphous silicon technology improvement at CEA/LETI," *Proc SPIE*, vol. 4650, pp. 138-149, 2002.

[5]   Wood, R. A. "Monolithic silicon microbolometer arrays" in *Uncooled Infrared Imaging Arrays and Systems, Semiconductors and Semimetals*, P.W. Kruse and D.D. Skatrud, Eds. New York: Academic, vol. 47, pp. 45-119, 1997.

[6]   Koester, D., A. Cowen, R. Mahadevan, M. Stonefield, and B. Hardy, "PolyMUMPs Design Handbook," MEMSCAP Inc., Revision 10.0, 2003.

[7]   Baltes, H. and O. Brand, "CMOS-based microsensors and packaging" *Sensors and Actuators A*, vol. 92, pp1-9, 2001.

[8]   Dereniak, E. L. and G. D. Boreman, *Infrared Detectors and Systems*. J. W. Goodman, Ed. New York: John Wiley & Sons, Inc., pp. 38-79, 1996.

[9]   Kimata, M., H. Yagi, M. Ueno, J. Nakanishi, T. Ishikawa, Y. Nakaki, M. Kawai, K. Endo, Y. Kosasayama, Y. Ohota, T. Sugino, and T. Sone, "Silicon infrared focal plane arrays," *Proc SPIE*, vol. 4288, pp 286-297, 2001.

[10]   Tissot, J. L. "Advanced IR detector technology development at CEA/LETI," *Infrared Physics & Technology*, vol. 43, pp. 223–228, 2002.

[11]   Sarusi, G. "QWIP or other alternative for third generation infrared systems," *Infrared Physics & Technology*, vol. 44, pp. 439–444, 2003.

[12]   Almasri, M., Z. Çelik-Butler, D. P. Butler, A. Yaradanakul, and A. Yildiz, "Uncooled multimirror broad-band infrared microbolometers," *J. Micro. Elec. Mech. Sys.*, vol. 11, no. 5, pp. 528-535, October 2002.

[13]   Pope, T. D., H. Jerominek, C. Alain, F. Picard, R. W. Fuchs, M. Lehoux, R. Zhang, C. Grenier, Y. Rouleau, F. Cayer, S. Savard, G. Bilodeau, J. F. Couillard, and C. Larouche, "256x1 and 256x40 pixel bolometer arrays for space and industrial applications," *Proc SPIE*, vol. 3436, pp. 325-331, 1998.

[14]   Breen, T., N. Butler, M. Kohin, C. A. Marshall, R. Murphy, T. Parker, and R. Silva, "More applications of uncooled microbolometer sensors," *Proc SPIE*, vol. 3436, pp. 530-540, 1998.

[15]   Miller, J. L., H. Duvoisin III, and G. Wiltsey, "Applications and performance of an uncooled infrared helmetcam," *Proc SPIE*, vol. 3436, pp. 566-571, 1998.

[16]   Jerominek, H., T. D. Pope, C. Alain, R. Zhang, M. Lehoux, F. Picard, R. W. Fuchs, C. Grenier, Y. Rouleau, F. Cayer, S. Savard, G. Bilodeau, J. F. Couillard, and C. Larouche, "128x128 pixel uncooled bolometric FPA for IR detection and imaging," *Proc SPIE*, vol. 3436, pp. 585-592, 1998.

[17]   Radford, W., R. Wyles, J. Wyles, J. Varesi, M. Ray, D. Murphy, A. Kennedy, A. Finch, E. Moody, F. Cheung, R. Coda, and S. Baur, "Microbolometer uncooled infrared camera with 20-mK NETD," *Proc SPIE*, vol. 3436, pp. 636-646, 1998.

[18]   Majumdar, A., M. Mao, T. Perazzo, Y. Zhao, O. Kwon, J. Varesi, and P. Norton, "Infrared vision using uncooled optomechanical camera," *Proc SPIE*, vol. 3948, pp. 74-79, 2000.

[19]   Daly, J. T., A. Bodkin, W. Schneller, R. Kerr, J. Noto, R. Haren, M. Eismann, and B. Karch, "Tunable narrow-band filter for LWIR hyperspectral imaging," *Proc SPIE*, vol. 3948, pp. 104-115, 2000.

[20]   Horn, S., D. Lohrmann, J. E. Miller, K. McCormack, G. Newsome, J. Brown, J. Campbell, Jr., P. Perconti, and G. Klager, "Small infrared sensors," *Proc SPIE*, vol. 4364, pp. 281-289, 2001.

[21]   Cochrane, D. M. T., P. A. Manning, and T. A. Wyllie, "Uncooled thermal imaging sensor for UAV applications," *Proc SPIE*, vol. 4369, pp. 168-177, 2001.

[22]   Horn, S., D. Lohrmann, J. Campbell, and P. Perconti, "Uncooled IR technology and applications," *Proc SPIE*, vol. 4369, pp. 210-221, 2001.

[23]   Gurnee, M. N., M. Kohin, R. Blackwell, N. Butler, J. Whitwam, B. Backer, A. Leary, and T. Nielson, "Developments in uncooled IR technology at BAE SYSTEMS," *Proc SPIE*, vol. 4369, pp. 287-296, 2001.

[24]   Yingwen, L., Y. Xinjian, H. Zhaoxiang, and L. Yan, "Infrared camera based on 320 x 240 uncooled focal plane array," *Proc SPIE*, vol. 4548, pp. 297-301, 2001.

[25]   Milton, Jr., O. J., R. M. Walker, and R. W. McMillan, "A compact, uncooled, long-wave infrared bolometer camera," *Proc SPIE*, vol. 4719, pp. 167-171, 2002.

[26]   George, T., "MEMS/NEMS development for space applications at NASA/JPL," *Proc SPIE*, vol. 4755, pp. 556-567, 2002.

[27]   Rogalski, A., "Infrared detectors - status and trends," *Progress in Quantum Electronics*, vol. 27, pp. 59-210, 2003.

[28]   Senesac, L. R., J. L. Corbeil, S. Rajic, N. V. Lavrik, and P. G. Datskos, "IR imaging using uncooled microcantilever detectors," *Ultramicroscopy*, vol. 97, pp. 451-458, 2003.

[29]   Kruse, P. W., *Uncooled Thermal Imaging: Arrays, Systems, and Applications*. Bellingham: SPIE, vol. TT51 pp. 1-88, 2001.

[30]   FLIR Systems Inc., http://www.flir.com/imaging/nmc/media/original/e6d4d356-5d40-4e23-87fa-c08d7bc00fa0.pdf, dated 11 August 2005.

[31]   Dereniak, E. L. and G. D. Boreman, *Infrared Detectors and Systems*. J. W. Goodman, Ed. New York: John Wiley & Sons, Inc., pp. 86-121, 1996.

[32]   Herwaarden, S. V. and G. C. M. Meijer, "Thermal Sensors" in *Semiconductor Sensors*, S.M. Sze, Ed. New York: Wiley, pp. 331-382, 1994.

[33]   Kovacs, G. T. A., *Micromachined Transducers Sourcebook*. New York: McGraw Hill, pp. 357-434, 1998.

[34]   Zhao, Y., M. Mao, R. Horowitz, A. Majumdar, J. Varesi, P. Norton, and J. Kitching, "Optomechanical uncooled infrared imaging system: Design, microfabrication, and performance," *J. Micro. Elec. Mech. Sys.*, vol. 11, pp. 136-146, April 2002.

[35]   Vig, J. R., R. L. Filler, and Y. Kim, "Uncooled IR imaging array based on quartz microresonators," *J. Micro. Elec. Mech. Sys.*, vol. 5, pp. 131-137, June 1996.

[36]   Hanson, C. M., H. R. Beratan, and J. F. Belcher, "Uncooled infrared imaging using thin-film ferroelectrics," *Proc SPIE*, vol. 4288, pp 298-303, 2001.

[37]   Wood, R. A., "High-performance infrared thermal imaging with monolithic silicon focal planes operating at room temperature," *IEEE Int. Electron Devices Meeting*, pp 175-177, 1993.

[38]   Tezcan, D. S., S. Eminoglu, and T. Akin, "A low-cost uncooled infrared microbolometer detector in standard CMOS technology," *IEEE Trans. on Electron Devices*, vol. 50, No. 2, pp 494-502, February 2003.

[39]   Dayeh, S. A., D. P. Butler, and Z. C. Butler, "Micromachined infrared bolometers on flexible polyimide substrates," *Sensors and Actuators A*, vol. 118, pp. 49-56, 2005.

[40]   Liger, M., S. Konishi, and Y. C. Tai, "Uncooled all-parylene bolometer," *Proc. IEEE MEMS Conf.*, pp. 593-596, Jan. 25-29, 2004.

[41]   Schaufelbuhl, A., N. Schneeberger, U. Munch, M. Waelti, O. Paul, O. Brand, H. Baltes, C. Menolfi, Q. Huang, E. Doering, and M. Loepfe, "Uncooled low-cost thermal imager based on micromachined CMOS integrated sensor array," *J. Micro. Elec. Mech. Sys.*, vol. 10, pp. 503-510, Dec 2001.

[42]   Iborra, E., M. Clement, L. V. Herrero, and J. Sangrador, "IR uncooled bolometers based on amorphous $Ge_xSi_{1-x}O_y$ on silicon micromachined structures" *J. Micro. Elec. Mech. Sys.*, vol. 11, pp 322-329, August 2002.

[43]   Brott, L. L., S. M. Rozenzhak, R. R. Naik, S. R. Davidson, R. E. Perrin, and M. O. Stone, "A poly(vinyl alcohol)/carbon-black composite film: A platform for biological macromolecule incorporation," *Adv. Mater.*, vol. 16, No. 7, pp. 592-596, April 5, 2004.

[44]   Hardy, B., "PolyMUMPs FAQ," MEMSCAP Inc., Revision 2.0, 2004.

[45]   Kovacs, G. T. A., *Micromachined Transducers Sourcebook*. New York: McGraw Hill, pp. 36-40, 1998.

[46]   E-mail correspondence with Busbee Hardy (buzz.hardy@memscapinc.com), MEMSCAP Inc., dated 15 December 2004.

[47]   Meeks, D., "Fundamentals of heat transfer in a multilayer system," *Microwave Journal*, vol. 35, No. 1, pp. 165-172, January 1992.

[48]   Dally, J. W., *Packaging of Electronic Systems: A Mechanical Engineering Approach.* New York: McGraw-Hill, pp. 305-308, 1990.

[49]   Bejan, A., *Heat Transfer.* New York: Wiley, pp. 335-378, 1993.

[50]   Kruse, P. W., "Principles of uncooled infrared focal plane arrays" in *Uncooled Infrared Imaging Arrays and Systems, Semiconductors and Semimetals*, P. W. Kruse and D. D. Skatrud, Eds. New York: Academic, vol. 47, pp. 17-42, 1997.

[51]   Dereniak, E. L. and G. D. Boreman, *Infrared Detectors and Systems.* J.W. Goodman, Ed. New York: John Wiley & Sons, Inc., pp. 182-183, 1996.

[52]   Class notes from EENG 777, taught by Capt. Paul Kladitis at the Air Force Institute of Technology, Summer Quarter 2004.

[53]   MEMSCAP, Inc., http://www.memscap.com/memsrus/svcsdata.php?RunID=62&CurrentPage=6&PHPSESSID=0d1c8cf7926d0189e3eccbb686e78554, dated 14 August 2005.

[54]   Pamula, V. K., A. Jog, and R. B. Fair, "Mechanical property measurement of thin-film gold using thermally actuated bimetallic cantilever beams," *Tech. Proc. of the 2001 Int. Conf. on Modeling and Simulation of Microsystems*, vol. 1, pp 410-413, 2001.

[55]   MEMS and Nanotechnology Clearinghouse, http://www.memsnet.org/material/, dated 14 August 2005.

[56]   Erkol, S. A., http://www.erkol.com/eng/Characteristics.htm#pvaerkol, dated 17 February 2005.

[57]   Dereniak, E. L. and G. D. Boreman, *Infrared Detectors and Systems*. J. W. Goodman, Ed. New York: John Wiley & Sons, Inc., p. 403, 1996.

[58]   Catamount Corp., http://www.catamountcorp.com/sale_items.html, dated 3 October 2001.

[59]   Amer, M. S., M. A. El-Ashry, L. R. Dosser, K. E. Hix, J. F. Maguire, and B. Irwin, "Femtosecond versus nanosecond laser machining: comparison of induced stresses and structural changes in silicon wafers," *Applied Surface Science*, vol. 242, pp. 162-167, 2005.

Vita

Captain Tetsuo Kaieda graduated from Sequim High School in Sequim, Washington. He entered undergraduate studies at Gonzaga University in Spokane, Washington where he graduated with a Bachelor of Sciences in Electrical Engineering in May 1999. He was commissioned through the United States Air Force Officer Training School, Maxwell AFB, Montgomery, Alabama in April 2000.

His first assignment was at Eglin AFB as a ALQ-155/SI Systems Engineer at the 36th Electronic Warfare Squadron in May 2000. While stationed at Eglin, he became a flight test engineer for the B-52 Branch of the 36 EWS. In August 2003, he entered the Graduate School of Engineering and Management, Air Force Institute of Technology. Upon graduation, he will be assigned to the National Air and Space Intelligence Center.

REPORT DOCUMENTATION PAGE

Form Approved
OMB No. 074-0188

1. REPORT DATE *(DD-MM-YYYY)* 13-09-2005	2. REPORT TYPE Master's Thesis	3. DATES COVERED *(From – To)* Mar 2004 – Sep 2005

4. TITLE AND SUBTITLE

Protein Impregnated Polymer (PIP) Film Infrared Sensor Using Suspended Microelectromechanical Systems (MEMS) Pixels

5a. CONTRACT NUMBER

5b. GRANT NUMBER

5c. PROGRAM ELEMENT NUMBER

6. AUTHOR(S)

Kaieda, Tetsuo, Captain, USAF

5d. PROJECT NUMBER

5e. TASK NUMBER

5f. WORK UNIT NUMBER

7. PERFORMING ORGANIZATION NAMES(S) AND ADDRESS(S)

Air Force Institute of Technology
Graduate School of Engineering and Management (AFIT/EN)
2950 Hobson Way
WPAFB OH 45433-7765

8. PERFORMING ORGANIZATION REPORT NUMBER

AFIT/GE/ENG/05-10

9. SPONSORING/MONITORING AGENCY NAME(S) AND ADDRESS(ES)

Air Force Research Laboratory (AFRL/MLPJE)
3005 P Street, Bldg 651
Wright-Patterson AFB, OH 45433-7702
(937) 255-3808, ext 3174
(Lawrence.Brott@wpafb.af.mil)

10. SPONSOR/MONITOR'S ACRONYM(S)

11. SPONSOR/MONITOR'S REPORT NUMBER(S)

12. DISTRIBUTION/AVAILABILITY STATEMENT

APPROVED FOR PUBLIC RELEASE; DISTRIBUTION UNLIMITED.

13. SUPPLEMENTARY NOTES

14. ABSTRACT

The Air Force Research Laboratory Materials and Manufacturing Directorate have developed a novel protein impregnated polymer (PIP) suspension that changes resistivity as a function of absorbed infrared radiation. Due to this property, the PIP is a potential material for use as an uncooled bolometer, or thermal sensor. In this research, a thermally-isolated pixel design, sensor characterization methods, and sensor fabrication and processing steps were developed. To create a microbolometer, the PIP was applied to two prototype micro-electro-mechanical systems (MEMS) surface micro-machined structures. The first is a raised cantilever pixel array that uses residual stress polysilicon and metal film arms to bend the pixels away from their substrate. The second is a suspended membrane pixel array in which the backside silicon wafer substrate is removed. The thermal sensor's figures of merit responsivity, detectivity, noise equivalent power, noise equivalent temperature difference, and thermal time constant, were modeled. An attempt was made to evaluate the performance of the fabricated microbolometer pixels by comparing measured data to model predictions. This research shows the PIP material can be used to make a practical thermal sensor.

15. SUBJECT TERMS

biomimetics, biological sensor, infrared (IR) detection, uncooled, thermal sensor, microelectromechanical systems (MEMS)

16. SECURITY CLASSIFICATION OF:			17. LIMITATION OF ABSTRACT	18. NUMBER OF PAGES	19a. NAME OF RESPONSIBLE PERSON Fellows, James A., Lt Col, USAF
a. REPORT U	b. ABSTRACT U	c. THIS PAGE U	UU	146	19b. TELEPHONE NUMBER *(Include area code)* (937) 255-3636, ext 4927 (James.Fellows@afit.edu)